

# The role of defects on electron behavior in graphene materials

**Citation for published version (APA):**

Cervenka, J. (2009). *The role of defects on electron behavior in graphene materials*. [Phd Thesis 1 (Research TU/e / Graduation TU/e), Applied Physics and Science Education]. Technische Universiteit Eindhoven.  
<https://doi.org/10.6100/IR642203>

**DOI:**

[10.6100/IR642203](https://doi.org/10.6100/IR642203)

**Document status and date:**

Published: 01/01/2009

**Document Version:**

Publisher's PDF, also known as Version of Record (includes final page, issue and volume numbers)

**Please check the document version of this publication:**

- A submitted manuscript is the version of the article upon submission and before peer-review. There can be important differences between the submitted version and the official published version of record. People interested in the research are advised to contact the author for the final version of the publication, or visit the DOI to the publisher's website.
- The final author version and the galley proof are versions of the publication after peer review.
- The final published version features the final layout of the paper including the volume, issue and page numbers.

[Link to publication](#)

**General rights**

Copyright and moral rights for the publications made accessible in the public portal are retained by the authors and/or other copyright owners and it is a condition of accessing publications that users recognise and abide by the legal requirements associated with these rights.

- Users may download and print one copy of any publication from the public portal for the purpose of private study or research.
- You may not further distribute the material or use it for any profit-making activity or commercial gain
- You may freely distribute the URL identifying the publication in the public portal.

If the publication is distributed under the terms of Article 25fa of the Dutch Copyright Act, indicated by the "Taverne" license above, please follow below link for the End User Agreement:

[www.tue.nl/taverne](http://www.tue.nl/taverne)

**Take down policy**

If you believe that this document breaches copyright please contact us at:

[openaccess@tue.nl](mailto:openaccess@tue.nl)

providing details and we will investigate your claim.

# The role of defects on electron behavior in graphene materials

PROEFSCHRIFT

ter verkrijging van de graad van doctor  
aan de Technische Universiteit Eindhoven,  
op gezag van de Rector Magnificus,  
prof.dr.ir. C.J. van Duijn,  
voor een commissie aangewezen  
door het College voor Promoties  
in het openbaar te verdedigen  
op dinsdag 28 april 2009 om 16.00 uur

door

**Jiří Červenka**

geboren te Nové Město na Moravě, Tsjechië

Dit proefschrift is goedgekeurd door de promotor:

prof.dr.ir. R.A.J. Janssen

Copromotor:

dr.ir. C.F.J. Flipse

CIP-DATA LIBRARY TECHNISCHE UNIVERSITEIT EINDHOVEN

Červenka, Jiří

The role of defects on electron behavior in graphene materials / by Jiří Červenka. -  
Eindhoven : Technische Universiteit Eindhoven, 2009.

Proefschrift.

ISBN 978-90-386-1722-0

NUR 924

Trefwoorden: grafeen / grafiet / rastertunnelmicroscopie / vibratiespectroscopie /  
elektronische structuur / ferromagnetisme / supergeleiding

Subject headings: graphene / graphite / scanning tunneling microscopy / inelastic  
electron tunneling spectroscopy / electronic structure / ferromagnetism / supercon-  
ductivity

Printed by *Omikron*, Prague

This research was financially supported by NanoNed, the Nanotechnology network in  
the Netherlands.

# Contents

<b>1</b>	<b>Introduction</b>	<b>1</b>
1.1	Carbon materials . . . . .	1
1.1.1	Graphene . . . . .	3
1.1.2	Graphite . . . . .	5
1.1.3	Fullerenes . . . . .	6
1.2	Scanning probe microscopies . . . . .	7
1.2.1	Scanning tunneling microscopy and spectroscopy . . . . .	8
1.2.2	Atomic, magnetic and electric force microscopies . . . . .	11
	Bibliography . . . . .	12
<b>2</b>	<b>Grain boundaries in graphite</b>	<b>15</b>
2.1	Introduction . . . . .	15
2.2	Experimental . . . . .	16
2.3	Results and discussions . . . . .	17
2.3.1	Structural properties of grain boundaries . . . . .	17
2.3.2	Electronic structure of grain boundaries . . . . .	22
2.3.3	Defects as a template for preferential absorption . . . . .	28
2.3.4	Characterization of STM tips with the aid of grain boundaries . . . . .	29
2.4	Conclusions . . . . .	31
	Bibliography . . . . .	32
<b>3</b>	<b>Ferromagnetism in graphite</b>	<b>35</b>
3.1	Introduction . . . . .	35
3.2	Experimental . . . . .	36
3.3	Results and discussion . . . . .	37
3.3.1	Magnetic force microscopy . . . . .	37
3.3.2	Superconductive quantum interference device magnetometer . . . . .	40
3.3.3	Magnetic impurity characterization . . . . .	43
3.3.4	Interpretations of the measured magnetic signal . . . . .	46

## CONTENTS

---

3.4	Conclusions . . . . .	57
	Bibliography . . . . .	58
<b>4</b>	<b>Graphene on silicon carbide</b>	<b>63</b>
4.1	Introduction . . . . .	63
4.2	Experimental . . . . .	65
4.3	Results and discussions . . . . .	66
4.3.1	Structural properties of few-layer graphene on SiC(0001) . . . . .	66
4.3.2	Electronic structure of epitaxial graphene . . . . .	73
4.3.3	Electronic structure of the interface layer . . . . .	77
4.3.4	Inelastic tunneling spectroscopy . . . . .	83
4.3.5	Electron scattering in graphene monolayer . . . . .	95
4.3.6	Is graphene on SiC a 2D superconductor? . . . . .	99
4.4	Conclusions . . . . .	103
	Bibliography . . . . .	104
<b>5</b>	<b>Wet deposition of fullerenes</b>	<b>109</b>
5.1	Introduction . . . . .	109
5.2	Experimental . . . . .	110
5.3	Results and discussions . . . . .	111
5.3.1	Spray coating of C <sub>60</sub> in solution . . . . .	111
5.3.2	C <sub>60</sub> on Au(111) . . . . .	114
5.4	Conclusions . . . . .	121
	Bibliography . . . . .	121
<b>A</b>	<b>Nonequilibrium Green's function theory</b>	<b>125</b>
	Bibliography . . . . .	132
	<b>Summary</b>	<b>133</b>
	<b>Samenvatting</b>	<b>137</b>
	<b>Acknowledgements</b>	<b>141</b>
	<b>Curriculum Vitae</b>	<b>143</b>

# Chapter 1

## Introduction

Carbon is a life sustaining element that, due to the versatility of its bonding, is present in nature in a variety of allotropic forms. Besides being an element that is fundamental for life on the planet, it is widely used in many technological fields and applications. For this reason, carbon-based materials can be encountered in common life on a daily basis. Although carbon has been studied widely in science for many centuries, there are still appearing new exciting discoveries and phenomena attracting many scientists. The aim of this thesis is to obtain a more detailed insight into a few interesting topics of physics in this prodigious material.

The thesis is formally divided into five chapters. In the first chapter, an introduction and a brief overview of the basic knowledge needed in following chapters are presented. The second chapter deals with structural defects in graphite, where electronic and structural properties of grain boundaries in graphite are studied on the nanometer scale. The third chapter touches an unexpected phenomenon in carbon materials, ferromagnetism, and it discusses conditions under which arises. The fourth chapter studies single atomic layer of graphite (graphene) grown on the SiC(0001) surface. An influence of the substrate on the structural, electronic, and vibrational properties of graphene is analyzed with local probe techniques. The last, fifth chapter deals with zero dimensional carbon, fullerenes, for which a new wet preparation method is developed for the formation of ultra thin fullerene layers on sample surfaces at ambient conditions.

### 1.1 Carbon materials

Carbon-based materials belong among the most versatile and widely studied solids. The reason lies in the chemical bonding of carbon. Carbon has four valence electrons in the  $2s^2p^2$ -configuration and two core electrons in the  $1s$ -orbital. In order to form

## 1. Introduction

---

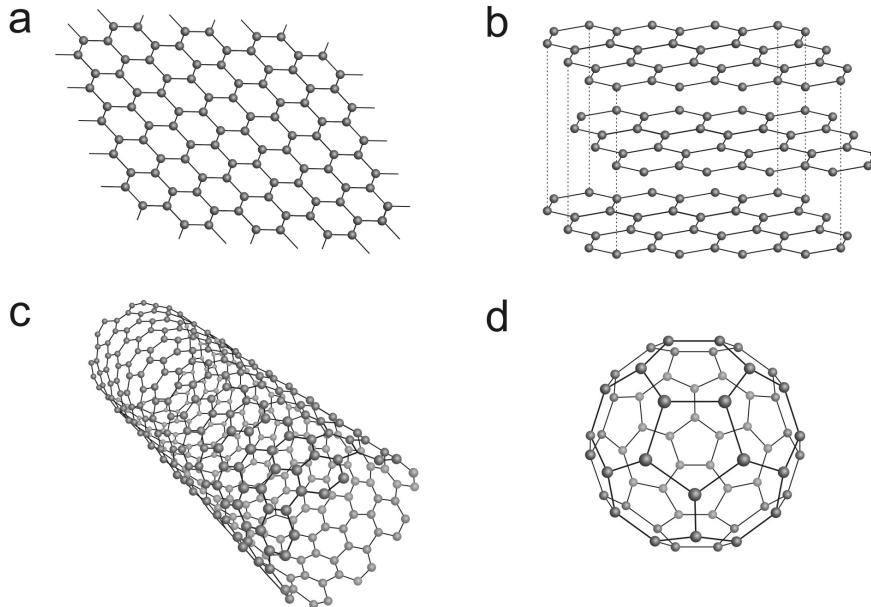


**Figure 1.1:** Atomic structures of graphene (a), graphite (b), carbon nanotube (c) and fullerene (d).

bonds, the atoms orbitals have to undergo a hybridization process. Three types of possible hybridizations can occur in carbon:  $sp$ - (acetylene),  $sp^2$ - (graphite), and  $sp^3$ -hybridizations (diamond). The other group IV elements (Si, Ge, etc.) appear primarily in the  $sp^3$ -hybridization. This in turn gives carbon the ability to adapt into various molecular and crystalline structures. Therefore, carbon exists in many allotropes covering up all dimensionalities: three-dimensional graphite, diamond and amorphous carbon, two dimensional graphene, one-dimensional nanotubes, and zero-dimensional fullerenes.

The physical properties of different carbon allotropes span over an astounding range of extremes. While diamond is the hardest material known, graphite is known for its softness and is used as a lubricant. Diamond is an excellent insulator with the largest known band gap 5.5 eV, fullerenes have semiconducting properties, and graphite, graphene and nanotubes are very good electrical conductors. In addition, when carbon is doped it can result in superconductivity, as it has been shown in intercalated graphite and alkali doped fullerenes [1–3].

The most stable crystalline form of carbon is graphite, which consists of planar honeycomb lattices of  $sp^2$ -bonded atoms called graphene, loosely piled up at regular distances  $c = 0.335$  nm. Graphene can be considered as the building block of many forms of carbon allotropes (see figure 1.1) and it has been used as the model system to

explain different properties of other  $sp^2$  bonded carbon forms. Graphite is obtained from graphene by stacking graphene layers on top of each other. Carbon nanotubes are synthesized by graphene wrapping into a cylinder. Depending on the direction in which graphene is rolled up, one can obtain either metallic or semiconducting electrical properties. Fullerenes can also be obtained from graphene by modifying the hexagons into pentagons and heptagons in a systematic way to obtain a ball. Even diamond can be obtained from graphene (graphite) under extreme pressure and temperatures by transforming the two dimensional  $sp^2$  bonds into three-dimensional  $sp^3$  bonds.

### 1.1.1 Graphene

Graphene is a single atomic layer of graphite with  $sp^2$  bonded carbon atoms in a honeycomb structure (figure 1.2a). The unit cell of graphene contains two equivalent A and B sublattices that lie at the origin of the special electronic properties of graphene. The electronic structure of graphene has been studied for more than half a century since the early work of Wallace [4]. As was mentioned before, the atomic electronic configuration of an isolated carbon atom is  $1s^2 2s^2 2p^2$ . In graphene, the three valence electrons in  $2s$ ,  $2p_x$  and  $2p_y$  orbitals are mixed with each other, which is well known as  $sp^2$  hybridization. These  $sp^2$  orbitals overlap and form strong  $\sigma$  bonds between carbon atoms in a graphene plane. On the other hand, the  $2p_z$  electrons form delocalized orbitals of  $\pi$  symmetry. The loosely bound  $\pi$ -electrons have much higher mobilities, so that the  $\pi$ -electrons play a dominant role in the electronic properties of graphene. In the low energies, the quasiparticles of graphene can be formally described by the Dirac-like Hamiltonian [5, 6]

$$\hat{H} = \hbar v_F \begin{pmatrix} 0 & k_x - ik_y \\ k_x + ik_y & 0 \end{pmatrix} = \hbar v_F \sigma \cdot \mathbf{k}, \quad (1.1.1)$$

where  $\mathbf{k}$  is the quasiparticle momentum,  $\sigma$  is the 2D Pauli matrix and  $v_F \approx 10^6 \text{ ms}^{-1}$  is the Fermi velocity. The resulting linear energy bands intersect at zero  $E$  near the edges of the Brillouin zone, giving rise to a conical spectrum for  $|E| < 1 \text{ eV}$  (figure 1.2b). Thus graphene is a two-dimensional zero-gap semiconductor, where its low-energy charge carriers are not described by the usual Schrödinger equation but are mimicking relativistic particles described by Dirac equation 1.1.1. By this way, graphene provides a new way to probe quantum electrodynamics (QED) phenomena in solid state physics [6]. The two-component description for graphene is very similar to the one by spinor wavefunctions in QED, where the "spin" index for graphene indicates sublattices rather than the real spin of electrons and is usually referred to as pseudospin  $\sigma$ . By analogy with QED, one can also introduce a quantity called chirality [6] that is formally a projection of  $\sigma$  on the direction of motion  $k$  and is positive (negative) for electrons (holes). In essence, chirality in graphene indicates



## 1. Introduction

---

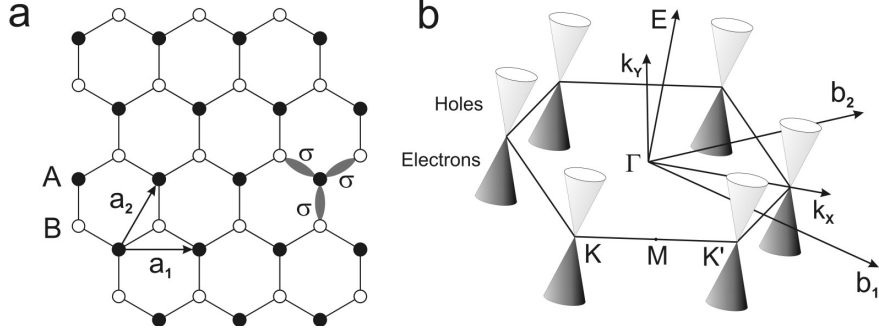


**Figure 1.2:** The 2D crystal structure of graphene and its first Brillouin zone. (a) The unit cell containing two atoms  $A$  and  $B$  defined by primitive vectors  $\mathbf{a}_1$  and  $\mathbf{a}_2$  with the lattice parameter  $a = 2.46 \text{ \AA}$ . (b) The first Brillouin zone of graphene with the points of high symmetry  $\Gamma$ ,  $M$  and two inequivalent  $K$  and  $K'$ .

the fact that electron and hole states are interconnected because they originate from the same carbon sublattices. As a result of these properties, graphene has led to the emergence of a number of new physical phenomena such as the anomalous half-integer quantum Hall effect [8], the minimal conductivity at the neutrality point [8], Klein tunneling [6], where relativistic particles can penetrate through a very high and wide potential barriers.

Although graphene has been known theoretically for many years, it has been presumed not to exist in the free state, being thermodynamically unstable and consequently fold into curved structures such as soot. The Manchester's group of Andre Geim has, however, shown that free standing graphene can exist and is stable, chemically inert and crystalline under ambient conditions. This opened a conceptually new class of materials that are only one atom thick and offer new inroads into low-dimensional physics that provide a fertile ground for applications [5]. In particular, graphene is a very promising candidate for electronic applications because it offers 2D electron gas system with extremely high mobility of electrons  $200,000 \text{ cm}^2/(\text{Vs})$  [9]. Unlike carbon nanotubes, conventional nanolithography can be applied to control geometry, which makes graphene more promising for future large-scale-integrated electronic devices. From a technological point of view, the graphite/silicon carbide system provides the most promising platform for ballistic-carrier devices based on nano-patterned epitaxial graphene [10]. This system of graphene grown on SiC(0001) is studied in chapter 4.

### 1.1.2 Graphite

Graphite has a three-dimensional (3D) layered crystal structure consisting of stacks of graphene planes. Among several possible layer stacking sequences, the ABAB sequence (Bernal crystal structure) is the most common and stable stacking sequence of graphite [11]. The layer separation in the Bernal structure is 3.35 Å. The unit cell of graphite consists of 4 atoms, as labeled by A, A', B and B' in figure 1.3a. The lattice parameters of the unit cell are  $c = 6.71$  Å and  $a = 2.46$  Å. The A and A' atoms have neighbors directly above and below in adjacent layer planes, whereas the B and B' atoms do not have such neighbors. The direct neighboring of A results in a bonding disturbance of electron density states, therefore only B atoms are resolved in scanning tunneling microscopy images on graphite [12].

The 3D first Brillouin zone of the Bernal graphite, as shown in figure 1.3b, is formed by the planes  $k_z = \pm\pi/c$  and the six planes going through the 2D Brillouin zone hexagon edges of length  $4\pi/3a$ . The band structure of graphite consists of 16 energy bands, where 12 of them are  $\sigma$ -bands and the other 4 are  $\pi$ -bands. Six  $\sigma$ -bands are bonding and the other six  $\sigma$  bands at higher energies are anti-bonding. These 2 groups of six  $\sigma$ -bands are separated by  $\approx 5$  eV [11]. The  $\pi$ -bands lie between these two groups of  $\sigma$ -bands. Similarly, two  $\pi$ -bands are bonding and the other two are anti-bonding. However, all 16 bands are coupled, from which the four  $\pi$ -bands are coupled the most strongly. Only half of the 16 energy bands in one unit cell are filled, thus the Fermi level lies in the middle of the four  $\pi$ -bands. The upper  $\pi$ -bands, which form the highest valence bands, overlap along the edges of Brillouin zone, making

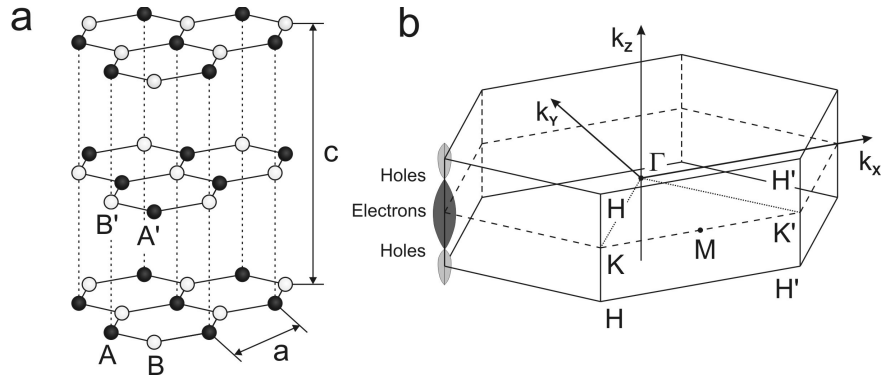


**Figure 1.3:** The crystal structure of graphite with Bernal stacking order ABAB and its Brillouin zone. (a) The primitive unit cell with dimensions  $a = 2.46$  Å and  $c = 6.71$  Å containing four atoms labeled as A, A', B and B'. (b) The Brillouin zone of graphite. The electron and hole Fermi surfaces are located in the vicinity of the edges HKH and H'K'H'.

## 1. Introduction

---

graphite a semi-metal, where the Fermi level is located near a sharp minimum in the density of states. The  $\pi$ -band overlap energy is about 0.03 eV, forming small electron pockets at the K (K') points and hole pockets at the H (H') points [11].

Graphite is a unique material that shows highly anisotropic properties. The anisotropic behavior of graphite is for example illustrated in the ability of graphite to act as a solid film lubricant. Graphene layers, stacked perpendicular to the  $c$  crystallographic axis, have a high inter-layer strength as a result of strong, covalent, carbon-carbon  $\sigma$  bonds. However, the weak  $\pi$  bonding, which holds adjacent graphene layers in alignment, yield with minimal energy, allowing graphene layers to peel away from each other. Graphite has a very high electrical conductivity in the direction parallel to the graphene planes, whereas conductivity perpendicular to graphene planes is several orders of magnitude smaller. Similarly, thermal conductivity of graphite is high along planes and small perpendicular to them, since phonons propagate very quickly along the tightly-bound planes, but are slower to travel from one plane to another. Magnetic properties of graphite are also highly anisotropic. Graphite is diamagnet, which shows one of the largest diamagnetic susceptibility next to superconductors, however, only in the direction perpendicular to graphene planes [13]. The diamagnetic susceptibility in the direction parallel to graphene planes is two orders of magnitude smaller in highly oriented pyrolytic graphite samples. This is because the magnetic properties of graphite are mainly governed by currents that circulate above and beneath the planar graphite layers [13]. In the real graphite samples containing structural defects, however, the electronic and therefore magnetic structure is completely governed by the presence of defects, as will be shown in chapters 2 and 3. In chapter 3, it will be shown that highly oriented pyrolytic graphite can become even ferromagnetic.

### 1.1.3 Fullerenes

Fullerenes are a unique class of molecules that represent the third form of pure carbon crystal structure, in addition to the familiar crystal structures of diamond and graphite [14]. They are all-carbon molecules with a closed cage, where the carbon atoms forming the cage are bonded in such a way that they form pentagonal rings and hexagonal rings. Fullerenes were discovered by Kroto *et al.* in 1985 [14] but have spread over the scientific community mainly after the development of a mass production method by Kratschmer *et al.* in 1990 [15]. Due to fullerene's unique structure and the potential importance of carbon in various aspects of science and technology, great efforts have been devoted to the understanding of their properties. Consequently, fullerenes are used in many areas of sciences, including physics, chemistry, biology, material science, and astronomy.

The most abundant member in the fullerene family is  $C_{60}$ . The molecular structure of  $C_{60}$  was shown in figure 1.1d. It consists of twelve pentagonal rings and twenty hexagonal rings, where none of the pentagonal rings make direct contact to each other. Each carbon atom is identical in the  $C_{60}$  cage, and the shape and structure resemble closely a soccer ball, for which it has been nicknamed as "buckyball". Each bond on the pentagonal rings is a single C-C bond, while those shared by two neighboring hexagonal rings are double C=C bonds. The diameter of the  $C_{60}$  molecule is 7 Å measured between carbon nuclei and 10 Å including the electron cloud [16,17].

$C_{60}$  is produced usually by the carbon arc method or by its variations [16]. It is stable in air and at higher temperatures.  $C_{60}$  has rich vibrational and electronic structure. The carbon atoms in fullerenes are predominantly in  $sp^2$  hybridization. The molecular structure results in a closed-shell electronic structure with highly degenerated  $\pi$ - and  $\sigma$ -derived molecular electronic states including the  $\pi$ -derived five-fold degenerate highest occupied molecular orbital (HOMO) and a triply degenerate lowest unoccupied molecular orbital (LUMO) [16]. The HOMO-LUMO gap of free  $C_{60}$  is 1.7 eV as found in the gas phase [18].  $C_{60}$  forms in a solid a close-packed structure with face-centered cubic (fcc) symmetry and lattice constant under ambient conditions 14.198 Å [16]. The  $C_{60}$  molecules are bonded by a weak intermolecular interaction of the van der Waals type.

Physical properties of fullerenes can be modified by attaching another elements or molecules to their cage. The chemical modification of fullerenes can be done by external or internal doping. The latter endohedral doping is possible due to the approximately spherical shape of the molecule, which leaves plenty of empty space for other inorganic and organic constituents. The doping of fullerenes can lead to different properties such as superconductivity in alkali-doped fullerenes [2,3] or magnetism in endohedral fullerene  $N@C_{60}$  [19]. The electronic properties of the fullerenes can also be modified upon the adsorption on different substrates. Since fullerenes are molecules consisting of large number of carbon atoms with various bonding nature, their bonding with the substrate can be quite complicated. Interesting phenomena may be expected, such as charge transfer, surface stress, chemical reactions, orientational ordering, and reconstruction on both adsorbates and substrates. In chapter 5, adsorption of fullerenes is studied on graphite and gold surfaces. The monolayer thick  $C_{60}$  layers are formed on sample surfaces by spray coating at ambient conditions.

## 1.2 Scanning probe microscopies

Scanning probe microscopy (SPM) is a branch of microscopy that forms images of surfaces by using a physical probe that scans over a surface of a specimen (figure 1.4).

## 1. Introduction

---

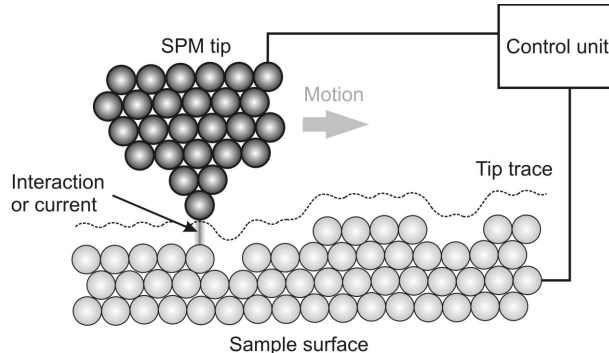


**Figure 1.4:** Schematic picture of a scanning probe microscope.

The development of the various scanning probe microscopy techniques has revolutionized the study of surface structure, by providing atomic resolution images in various environments such as ultra high vacuum (UHV), atmospheric pressure and even under solution [20, 21]. The number of SPM techniques is constantly growing, as the tip can be modified in many ways to investigate surface properties (for review see [20, 21]). Among the best known SPM techniques belong scanning tunneling microscopy, atomic force microscopy, magnetic force microscopy, and electric force microscopy, which are used in this thesis.

### 1.2.1 Scanning tunneling microscopy and spectroscopy

Scanning tunneling microscopy (STM) is one of the most used methods to determine structural and electric properties of a sample surface on the atomic scale. STM was the first technique able to observe atoms in the real space, for which the inventors of STM, Gerd Binnig and Heinrich Rohrer [22], have received the Nobel prize in physics in 1986. The microscope consists of a surface (metallic or semiconducting material) and a metallic tip with an atomically sharp apex. The STM uses the tunneling effect to obtain a current between a sharp tip and the sample by applying a voltage between them. When a conducting tip is brought very close to a metallic or semiconducting surface, an applied bias between them can allow electrons to tunnel through the vacuum barrier between them. For a small bias voltage compared to the work function  $\Phi$ , the tunneling barrier is roughly rectangular with a width given by the tip-sample distance  $z$  and a height  $\Phi$ . Then according to elementary quantum mechanics, the tunneling current is given by [21]

$$I_t(z) = I_0 e^{-2z\sqrt{2m\Phi/\hbar}}, \quad (1.2.1)$$

where  $I_0$  is a function of the applied voltage and the density of states in both tip and sample,  $m$  is the mass of the electron, and  $\hbar$  is reduced Planck's constant. The exponential  $I(z)$  dependence makes STM an extremely height sensitive technique, since a very small change of the tip-sample distance causes a huge change in the tunneling current. In order to obtain a real space map of the surface, the STM tip is scanned over the surface. This is done in the most used STM mode, the constant-current mode, by maintaining the tunneling current constant by an electrical feedback loop that keeps it to a preset current by varying the distance between tip and sample. The topography of the sample is then deduced from the movements of the piezoelements that are very precise manipulators used for the  $xyz$ -movements of the tip (sample). The atomic resolution capability of the STM is based on the ability to move STM tip with a pm precision and on the fact that most of the tunneling current is carried by the last atom at the apex of the STM tip, which is the closest to the sample.

### Scanning tunneling spectroscopy

One of the most fascinating potentials of the STM is its capability to obtain spectroscopic data with an atomic resolution. STM in a spectroscopic mode can probe the local density of states (LDOS) of a material. This is because the tunneling current at low bias voltages is a function of the LDOS [23]. Following the Bardeen's theory [24], the tunneling current between the two electrodes separated by an insulating barrier can be expressed on the basis of the Fermi's golden rule as

$$I \propto \int_{-\infty}^{\infty} |M(E)|^2 \rho_T(E - eV) \rho_S(E) [f(E - eV) - f(E)] dE, \quad (1.2.2)$$

where  $f$  is the Fermi-Dirac distribution function for electrons,  $V$  is the bias voltage applied between the electrodes,  $\rho_{T,S}$  are densities of states of the tip and sample, and  $M$  denotes the tunneling matrix element, which is giving information about the orbital character of the tip and sample wave functions and about their overlap (for more information see [23, 25]). In the STM topography mode, however, the tunneling current is maintained constant by the feedback system and is a function of a tip-sample distance. Therefore, an STS spectrum is obtained by positioning the tip at the place of interest at a fixed distance from a sample (opened feedback loop) and the bias voltage is swept over the energy range of interest and the current is recorded, resulting in a  $I(V)$  curve. The first derivative of the  $I(V)$  curve gives information about the LDOS of the sample surface and tip [20]. According to Baarden's theory using the Fermi's golden rule and at the limit of low temperatures and low bias voltage

$$\frac{dI}{dV} \propto |M|^2 \rho_T(E_F) \rho_S(E_F), \quad (1.2.3)$$

## 1. Introduction

---

meaning that the tunneling conductivity at low bias voltages is given by the convolution of the densities of states of the tip and sample. The DOS of the metallic tip is usually assumed to be flat. Unfortunately, the tunneling current is often too noisy to obtain reasonable data by calculating  $dI/dV$  numerically. Therefore, in most tunneling spectroscopy experiments  $dI/dV$  spectra are obtained by using a lock-in amplifier in order to increase the signal to noise ratio [26].

### Inelastic electron tunneling spectroscopy

Apart to the electronic structure, an  $I(V)$  curve can contain information about the vibration properties of the surface atoms or molecules. This method is called inelastic electron tunneling spectroscopy (IETS). While electrons are tunneling between tip and sample, they can undergo inelastic proces, at which they lose their energy by exciting a vibration or a phonon. This opens a new inelastic tunneling path next to the classical elastic tunneling path, which results in an increase of the tunneling current above voltage associated with the energy of the vibration (phonon). This is seen as a step in the  $dI/dV$ . However, because the inelastic contributions are usually very small, in the order of 1% of the total current [26–28], IETS measures the second derivative of the current voltage relationship. In the  $d^2I/dV^2$  spectra, the inelastic loss features of electrons are observed as peaks at the onset of the loss vibrational modes for positive sample bias and as minima for negative sample bias, respectively. The  $d^2I/dV^2$  spectra in IETS is usually obtained by a lock-in amplifier technique, where two lock-in amplifiers are connected to the electronic loop measuring the tunneling current. For this purpose, a sinusoidal reference signal with amplitude  $A$  is superimposed to the applied sample bias. The second harmonic component of the modulated signal is proportional to  $d^2I/dV^2$  [26].

The local capability of STM-IETS has been proven to be a valuable tool to access the vibrational properties of adsorbates at surfaces. IETS was successfully applied in detecting local inelastic electron energy-loss spectra of individual molecules adsorbed on metallic substrates [27, 28]. Vibrations of single molecules as large as  $C_{60}$  have been detected [29]. IETS has an advantage in comparison to the traditional techniques studying vibrations that it can give information about the local vibrational properties, while the traditional techniques such as Raman, infrared and high resolution energy electron loss spectroscopies (HREELS) measure averaged signals over a larger ensemble of molecules. However, not all the vibronic modes are observed in STM-IETS. This shows that the detected vibrations in the inelastic tunneling might be dependent on the electron pathway and symmetry arguments as has been recently shown by theoretical modeling [30]. Moreover, the signals measured in IETS are extremely small reaching the intensity of the inelastic signals in the order of few percent

of the total current. This can be changed, as will be shown in chapter 4.3.4, if IETS experiments are properly designed.

### 1.2.2 Atomic, magnetic and electric force microscopies

The development of the atomic force microscope (AFM) [31] has represented a new milestone in the field of surface science techniques, because it allowed to study a whole new class of insulating surfaces and soft biological samples, which could not be studied by STM. STM can be applied only to samples with a good conductivity such as metals or semiconductors. On the other hand in AFM, instead of current, the force between a small sharp tip and a particular surface is used to obtain images with even atomic resolution at special cases. The principle of AFM relies on measuring atomic interactions between very sharp tip and atoms of a sample surface, which are brought in the vicinity. For this purpose, the AFM tip is attached to a flexible cantilever. The force applied on the tips is measured from the deflection of the cantilever by optical (interferometer, beam-deflection) or electrical methods (piezoelectric, piezoresistive). Two operating modes can be used to obtain AFM images. In the contact AFM mode, the topography of a sample surface is obtained by maintaining a constant repulsive force between the sample and tip while scanning. The other dynamic AFM mode uses a deliberately vibrating cantilever, where the interaction between tip and sample changes vibrational amplitude, frequency and phase. In this mode, one of these parameters is used by the feedback system to obtain topography images.

AFM is a very versatile tool, which can be operated in ambient conditions, vacuum, controlled atmosphere, and liquids. By modifying an AFM tip, other forces such as electrostatic or magnetic can be measured. These methods are called electrostatic (EFM) and magnetic force microscopies (MFM). For this reason, very soft (i.e. force sensitive) Si AFM probes are coated by metallic or magnetic coating materials. The operation of MFM and EFM consists of two steps. In the first run, a topography is obtained in the normal dynamic AFM mode in a line scan. Then the tip is lifted to a height, where the long range magnetic (electrostatic) forces prevail, and the same trace as in topography is followed and the change of the amplitude and the phase is recorded. By repeating this sequence, MFM (EFM) images are constructed. The resolution of MFM and EFM is not as good as the resolution of AFM, because of the large tip-sample separation and a larger radius of MFM and EFM tips due to magnetic coating layer.



## Bibliography

- [1] T. E. Weller, M. Ellerby, S. S. Saxena, R. P. Smith, and N. T. Skipper, *Nature Physics* **1**, 39 - 41 (2005).
- [2] A. F. Hebard, M. J. Rosseinsky, R. C. Haddon, D. W. Murphy, S. H. Glarum, T. T. M. Palstra, A. P. Ramirez and A. R. Kortan, *Nature* **350**, 600 (1991).
- [3] R. C. Haddon, A. F. Hebard, M. J. Rosseinsky, D. W. Murphy, S. J. Duclos, K. B. Lyons, B. Miller, J. M. Rosamilia, R. M. Fleming, A. R. Kortan, S. H. Glarum, A. V. Makhija, A. J. Muller, R. H. Eick, S. M. Zahurak, R. Tycko, G. Dabbagh and F. A. Thiel, *Nature* **350**, 320 (1991).
- [4] P. K. Wallace, *Phys. Rev.* **71**, 622 (1947).
- [5] A. K. Geim and K. S. Novoselov, *Nature Materials* **6**, 183 (2007).
- [6] M. I. Katsnelson, K. S. Novoselov, and A. K. Geim, *Nature Physics* **2**, 620 (2006).
- [7] K. S. Novoselov, A. K. Geim, S. V. Morozov, D. Jiang, Y. Zhang, S. V. Dubonos, I. V. Grigorieva, and A. A. Firsov, *Science* **306**, 666 (2004).
- [8] K. S. Novoselov, A. K. Geim, S. V. Morozov, D. Jiang, M. I. Katsnelson, I. V. Grigorieva S. V. Dubonos, and A. A. Firsov, *Nature* **438**, 197 (2005).
- [9] S. V. Morozov, K. S. Novoselov, M. I. Katsnelson, F. Schedin, D. C. Elias, J. A. Jaszczak, and A. K. Geim, *Phys. Rev. Lett.* **100**, 016602 (2008).
- [10] C. Berger, Z. Song, T. Li, X. Li, X. Wu, N. Brown, C. Naud, D. Mayou, A. N. Marchenkov, E. H. Conrad, P. N. First, and W. A. de Heer, *Science* **312**, 1191 (2006).
- [11] J.-C. Charlier, J.-P. Michenaud, X. Gonze, and J.-P. Vigneron, *Phys. Rev. B* **44**, 13237 (1991).
- [12] D. Tománek and S. G. Louie, *Phys. Rev. B* **37**, 8327 (1998).
- [13] T. L. Makarova, Magnetic properties of carbon structures, *Semiconductors* **38**, 615 (2004).
- [14] H. W. Kroto, J. R. Heath, S. C. O'Brien, R. F. Curl and R. E. Smalley, *Nature* **318**, 162 (1985).
- [15] W. Krätschmer, L. D. Lamb, K. Fostiropoulos and D. R. Huffman, *Nature* **347**, 354 (1990).

## 1.2 Bibliography

---

- [16] M. S. Dresselhaus, G. Dresselhaus, P. C. Eklund, *Science of Fullerenes and Carbon Nanotubes*, Academic Press, San Diego, 1996.
- [17] L. Forró and L. Mihály, *Rep. Prog. Phys.* **64**, 649 (2001).
- [18] S. H. Yang, C. L. Pettiette, J. Conceicao, O. Cheshnovsky, and R. E. Smalley, *Chem. Phys. Lett.* **139**, 233 (1987).
- [19] T. Almeida Murphy, T. Pawlik, A. Weidinger, M. Hhne, R. Alcalá, and J. M. Spaeth, *Phys. Rev. Lett.* **77**, 1075 (1996).
- [20] R. Wiesendanger, *Scanning Probe Microscopy: Analytical Methods*, Springer, Berlin, 1998.
- [21] F. J. Giessibl, *Rev. Mod. Phys.* **75**, 949 (2003).
- [22] G. Binnig, H. Röhrer, Ch. Gerber, E. Weibel, *Phys. Rev. Lett.* **49**, 57 (1982).
- [23] J. Tersoff and D. R. Hamann, *Phys. Rev. B* **31**, 805 (1985).
- [24] J. Bardeen, *Phys. Rev. Lett.* **6**, 57 (1961).
- [25] C. J. Chen, *Phys. Rev. B* **42**, 8841 (1990).
- [26] J. H. A. Hagelaar, The role of the electron trajectory in scanning tunneling microscopy: elastic and inelastic tunneling through NO on Rh(111), Ph.D. thesis, Eindhoven University of Technology (2008).
- [27] B. C. Stipe, M. A. Rezaei, and W. Ho, *Science* **280**, 1732 (1998).
- [28] H. J. Lee and W. Ho, *Science* **286**, 1719 (1999).
- [29] J. I. Pascual, J. Gomez-Herrero, D. Sanchez-Portal, and H. P. Rust, *J. Chem. Phys.* **117**, 9531 (2002).
- [30] A. Troisi and M. A. Ratner, *J. Chem. Phys.* **125**, 214709 (2006).
- [31] G. Binnig, C. F. Quate, and Ch. Gerber, *Phys. Rev. Lett.* **56**, 930 (1986).



## Chapter 2

# Grain boundaries in graphite

### 2.1 Introduction

Understanding the defect structures and their role on the electronic structure of graphite is a keystone for carbon nanostructures and carbon materials in general. Defects are inevitable constituents of graphite which have profound influence on its electrical, chemical and other physical properties. Recently, graphene (single layer of graphite) and few-layer graphene showed a number of unconventional properties [1–3] and it seems to be of great importance to understand the influence of defects in this material for possible future applications.

Although graphite is one of the most extensively studied materials there are still new phenomena observed on graphite surfaces with scanning tunneling microscope (STM), which are not well understood [4,5]. In particular, defect structures in the  $sp^2$  bonded carbon lattice have many representations and have not been well characterized experimentally yet [6,7].

Grain boundaries are one of the most commonly occurring extended defects in highly oriented pyrolytic graphite (HOPG) because of its polycrystalline character. Observations of grain boundaries have been reported on the graphite surface with STM before [8–11] and recently also on few graphene layers grown on C-face of SiC [12]. Periodic structures [9–12] and disordered regions [8] have been observed along grain boundaries. For a large angle tilt grain boundary evidence of possible presence of pentagon-heptagon pairs was shown [10]. Although the structure of various grain boundaries in graphite has been examined with STM, there is no proper model that can explain all observations. Moreover, the electronic structure of grain boundaries has not been investigated so far.

Point defects and extended defects in graphene and graphite have been widely studied theoretically in the last decade [13–28]. In general, defects in the carbon hon-

## 2. Grain boundaries in graphite

---

eycomb lattice give rise to quasilocalized electron states at the Fermi energy [19, 22]. These states extend over several nanometers around the defects forming characteristic  $(\sqrt{3} \times \sqrt{3})R30^\circ$  superstructures as has been observed with STM on graphite [29–32] and graphene [33]. In the absence of electron-hole symmetry, these states induce transfer of charge between the defects and the bulk leading to phenomenon called self-doping [22]. Moreover, it has been shown that point defects such as vacancies and hydrogen-terminated vacancies could be magnetic [18–27] showing that electron-electron interactions play an important role in graphene systems because of low electron densities at the Fermi energy. These defects could be the origin of observed ferromagnetism in different graphite samples [34–37].

In this chapter, an experimental study of structural and electronic properties of grain boundaries in HOPG is presented. Various grain boundaries have been systematically studied by AFM and STM. Their structural properties are characterized in section 2.3.1. A crystallographic model producing periodically distributed point defects is proposed to reproduce all STM experimental observations of grain boundaries on graphite surfaces. Scanning tunneling spectroscopy (STS) characterization of a local electronic structure of grain boundaries is discussed in section 2.3.2. STS on grain boundaries shows localized states and enhanced charge density in comparison to a bare graphite surface. In the last two sections, grain boundaries are utilized as template for adsorbing external clusters of magnetic atoms (section 2.3.3) and as a tool for characterization of STM tips on the graphite surface (section 2.3.4).

## 2.2 Experimental

Samples of HOPG of ZYH quality were purchased from NT-MDT. The ZYH quality of HOPG with the mosaic spread  $3.5^\circ - 5^\circ$  has been chosen because it provides a high population of grain boundaries on the graphite surface. HOPG samples were cleaved by an adhesive tape in air and transferred into a scanning tunneling microscope (Omicron RT and LT STM) working under ultra high vacuum (UHV) condition. The HOPG samples have been heated to  $500^\circ\text{C}$  in UHV before the STM experiments. STM measurements were performed in the constant current mode with either mechanically formed Pt/Ir tips or electrochemically etched W tips at three different temperatures 5 K, 78 K and 300 K. STS spectra have been obtained by using a lock-in amplifier technique with frequency 990 Hz and amplitude 25 mV at 300 K or 10 mV at 78 K. The same samples have been subsequently studied by atomic force microscopy (AFM) using Multimode scanning probe microscope with Nanoscope IV controller from Veeco Instruments in air. Ni clusters have been obtained by thermal evaporation of the 99.99% pure nickel onto the graphite surface at the pressure

$10^{-8}$  mbar.

## 2.3 Results and discussions

### 2.3.1 Structural properties of grain boundaries

Figure 2.1 shows typical examples of grain boundaries observed on the HOPG surface with AFM and STM. In AFM, grain boundaries appear as lines protruding above a graphite surface by a small height up to 0.3 nm. On the other hand in STM, grain boundaries show a periodic one-dimensional superlattice with height corrugations ranging from 0.4 nm to 1.5 nm, which are almost independent on the applied bias voltage. Since grain boundaries have much smaller height in AFM and the corrugation of STM is given by convolution of the topography and the local density of states (DOS) of the substrate, grain boundaries possess enhanced charge density of states compared to the bare graphite surface. Similar effects have been observed on defects artificially created by low-energy ions on the graphite surface [6]. STM images of ion bombarded surfaces showed defects as hillock, which did not originate from a geometric protrusion of a surface but from an increase in DOS near the Fermi energy level [6].

Grain boundaries form an continuous network over graphite surface. They interconnect each other as can be seen in figures 2.1(a) and 2.1(d). Grain boundaries are the surface signature of bulk defects of HOPG, so they overrun step edges of an arbitrary height without altering their direction, periodicity and corrugation, which is depicted in figures 2.1(a) and 2.1(c). During the cleavage of the HOPG substrate, grain boundaries pose as weak points, therefore step edges are created out of them on the graphite surface. Figure 2.1(b) displays a grain boundary at the bottom left part of the image, which transforms itself into a step edge in the right part of the image. Region I is separated by a monoatomic step (0.35 nm height) from region II and by a double step (0.7 nm height) from region III.

Grain boundaries set bounds to so called 2D superlattices, which are frequently observed on graphite surfaces in STM [4]. Two examples are shown in figures 2.1(c) and 2.1(d). The most accepted origin of 2D superlattices discussed in the literature is a rotation of the topmost graphite layer with respect to the other layers, which produces Moiré pattern [4]. Although Moiré pattern can not explain all the superlattices reported in literature [4], it has been in good agreement with all observed 2D superlattices in our STM measurements.

One of the most intriguing properties of grain boundaries is their well defined 1D superlattice periodicity. We have analyzed various grain boundaries on HOPG surfaces. Their superlattice periodicities have been found in the range from 0.5 nm

## 2. Grain boundaries in graphite

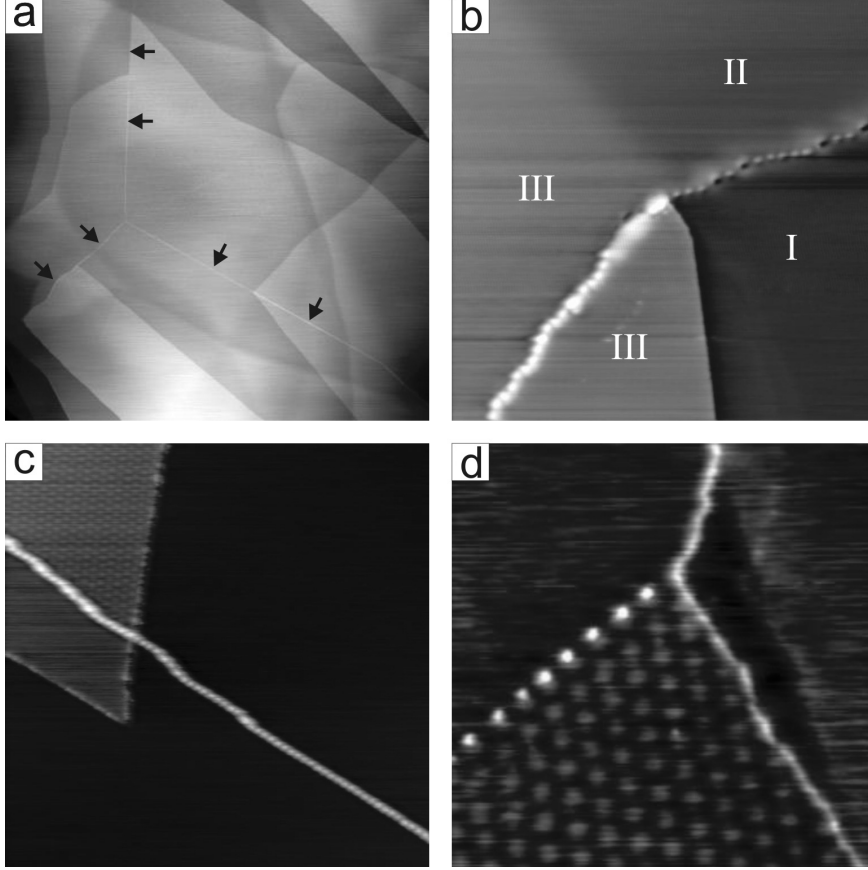


**Figure 2.1:** (a) AFM image of the HOPG surface with a grain boundary indicated by arrows ( $3.5 \times 3.5 \mu\text{m}^2$ ). (b) STM image of a grain boundary continuing as a step edge ( $105 \times 105 \text{ nm}^2$ ,  $U = -0.5 \text{ V}$ ,  $I = 0.5 \text{ nA}$ ). (c) STM image of a grain boundary extending over a step edge ( $186 \times 186 \text{ nm}^2$ ,  $U = -0.3 \text{ V}$ ,  $I = 0.3 \text{ nA}$ ) (d) STM on grain boundaries bordering a 2D superlattice  $D_1 = 4.6 \text{ nm}$   $D_2 = 0.9 \text{ nm}$  ( $60 \times 60 \text{ nm}^2$ ,  $U = -0.4 \text{ V}$ ,  $I = 0.4 \text{ nA}$ ).

to 10 nm. Two periodicities within one superlattice have been observed as shown in figure 2.2(a). The second periodicity occurs as the direction of a grain boundary changes by  $30^\circ$  or  $90^\circ$ . Figure 2.2(b) represents a cross section over the top of the grain boundary from figure 2.2(a) going over a polyline ABC with a  $30^\circ$  bend in the point B. The periodicity along the line AB is  $D_1 = 2.18 \text{ nm}$  with a height corrugation 0.6 nm and the periodicity along the line BC is  $D_2 = 3.83 \text{ nm}$  with a height corrugation of 0.9 nm. The periodicity  $D_2$  is approximately  $\sqrt{3}D_1$ , which will be used as a notation for the second superlattice periodicity later in the text.

In figure 2.3, atomically resolved current STM images of three different grain

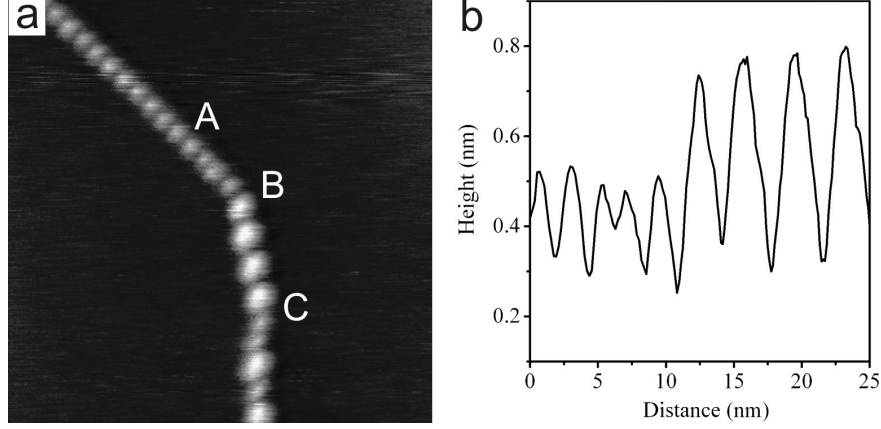


**Figure 2.2:** (a) STM image of a grain boundaries with two periodicities  $D_1 = 2.18$  nm and  $D_2 = 3.83$  nm. (b) Cross section over the grain boundary in figure (a) along the polyline ABC. Scanning parameters:  $50 \times 50$  nm<sup>2</sup>,  $U = 1$  V,  $I = 0.1$  nA.

boundaries and their fast fourier transformation (FFT) images are shown. The grain boundaries exhibit 1D superlattices with periodicities  $D = 1.25$  nm in figure 2.3(a),  $\sqrt{3}D = 1.4$  nm in figure 2.3(c) and  $\sqrt{3}D = 0.83$  nm in figure 2.3(e). It is apparent from these images that grain boundaries in graphite are tilt grain boundaries, which are produced between two rotated graphite grains. No preferential orientation of grains has been found. Angles between grains have been found in the interval from  $1^\circ$  to  $29.5^\circ$ . Graphite grains are rotated by angles  $12^\circ$ ,  $18^\circ$  and  $29.5^\circ$  in figures 2.3(a), 2.3(c) and 2.3(e), respectively. The rotation of the graphite grains can be seen as well in the FFT images in figures 2.3(b), 2.3(d) and 2.3(f), where points labeled as A and A' are forming apexes of two rotated hexagons representing the graphite lattices in the reciprocal space. Six points marked as B demonstrate  $\sqrt{3} \times \sqrt{3}R30^\circ$  superstructure, which has been observed around point defects and step edges of graphite previously [29, 30]. The  $\sqrt{3} \times \sqrt{3}R30^\circ$  superstructure is produced by scattering of the free electrons off defects, which generates standing wave patterns in the electron density [29]. Figure 2.3(b) shows clearly two rotated  $\sqrt{3} \times \sqrt{3}R30^\circ$  superstructures B and B' corresponding to scattering patterns in two different grains. The center part of the FFT image marked as C represents the large periodicities in the real space of the 1D superlattice.

The structure of all grain boundaries observed on HOPG surfaces can be explained by a simple model, where the superlattice periodicity is determined only by two parameters:  $\alpha$  the angle between the grains and  $\beta$  the orientation of a grain boundary in respect to the graphite lattice. The orientation towards the graphite lattice can be either  $\beta_D = 30^\circ \pm \alpha/2$  or  $\beta_{\sqrt{3}D} = \pm\alpha/2$ . The sign turns on which direction



## 2. Grain boundaries in graphite

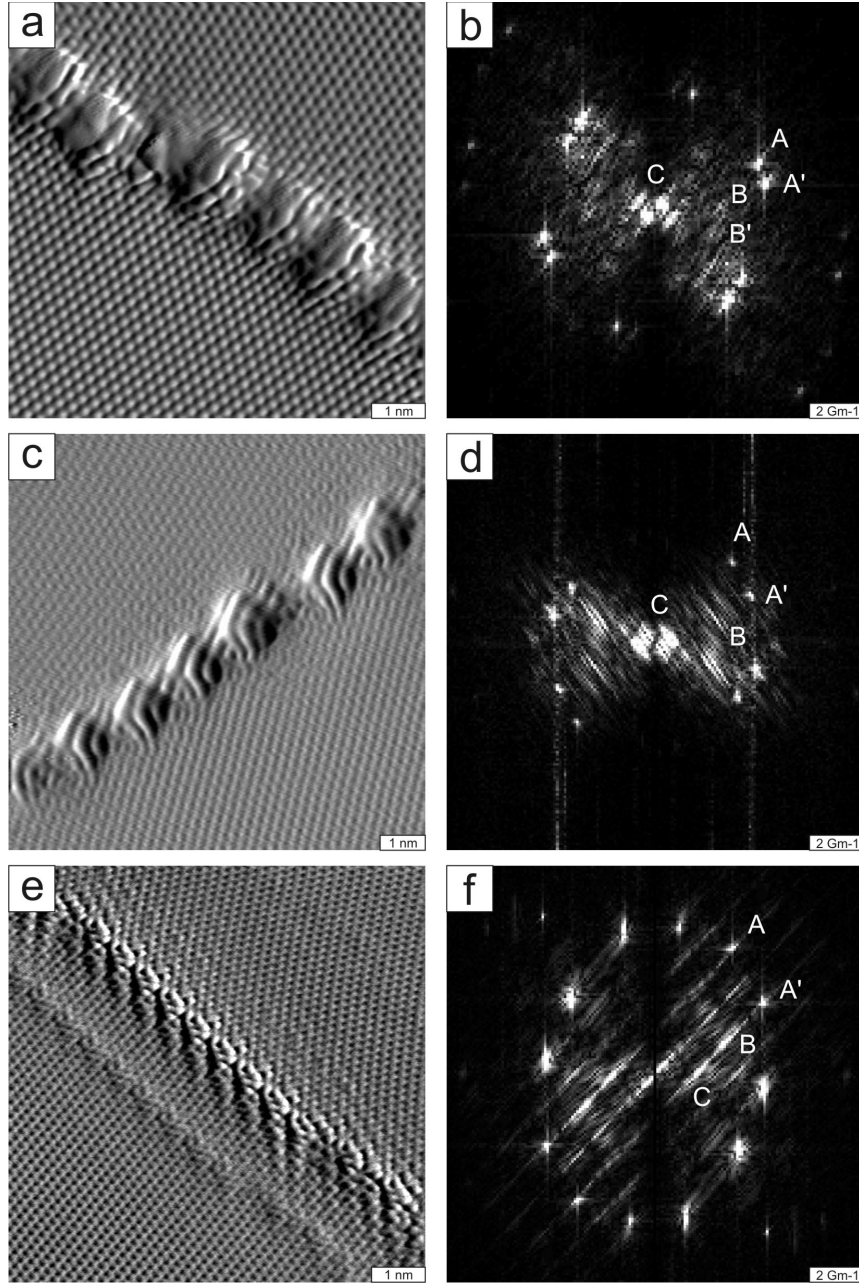


**Figure 2.3:** Current STM images of three different grain boundaries on HOPG (a), (c) and (e), and their FFT images (b), (d) and (f), respectively. Grain boundaries show 1D superlattices with periodicities  $D = 1.25$  nm (a),  $\sqrt{3}D = 1.4$  nm (c) and  $\sqrt{3}D = 0.83$  nm (e). The angle between two graphite grains is  $\alpha = 12^\circ$  (a),  $\alpha = 18^\circ$  (c) and  $\alpha = 29.5^\circ$  (e) and the angle between the grain boundary and the graphite lattice is  $\beta = 25^\circ$  (a),  $\beta_{\sqrt{3}D} = 9^\circ$  (c) and  $\beta_{\sqrt{3}D} = 13.5^\circ$  (e). Scanning parameters:  $10 \times 10$  nm<sup>2</sup>,  $U = 0.5$  V,  $I_t = 0.3$  nA.

of the graphite lattice is taken as a reference. Two superlattice periodicities could be constructed  $D_1 = D$  for  $\beta_D$  orientation and  $D_2 = \sqrt{3}D$  for  $\beta_{\sqrt{3}D}$  orientation. The superlattice periodicity  $D$  is given by a simple formula for a Moiré pattern  $D = d/2\sin(\alpha/2)$ , where  $d = 0.246$  nm is the graphite lattice parameter.

In figure 2.4 a schematic illustration of the crystallographical structure of two possible orientations of grain boundaries is shown. Periodically distributed point defects are created in this way having the superlattice periodicity  $D$  or  $\sqrt{3}D$  separation between them. The periodicities of the grain boundaries and angles between the graphite grains have been chosen according to STM observations  $\alpha = 12^\circ$ ,  $D = 1.18$  nm in figure 2.4(a) and  $\alpha = 18^\circ$ ,  $\sqrt{3}D = 1.36$  nm in figure 2.4(b). A large angle tilt grain boundary shown in figure 2.3(e) is very similar to a grain boundary on graphite reported by Simonis *et al.* [10], where possible presence of the pentagon-heptagon pairs has been predicted on the base of comparison between experimental STM images and theoretically calculated STM images.

Similarly, like for graphite edges, grain boundaries have two basic shapes, which are rotated by  $30^\circ$  towards each other. The orientation  $\beta_D$  in figure 2.3(a) has an armchair character at the axis of the grain boundary, while the  $\beta_{\sqrt{3}D}$  orientation in figure 2.3(b) has a zigzag character. As it was mentioned before grain boundaries are weak spots of graphite lattice therefore edges are produced out of them in the

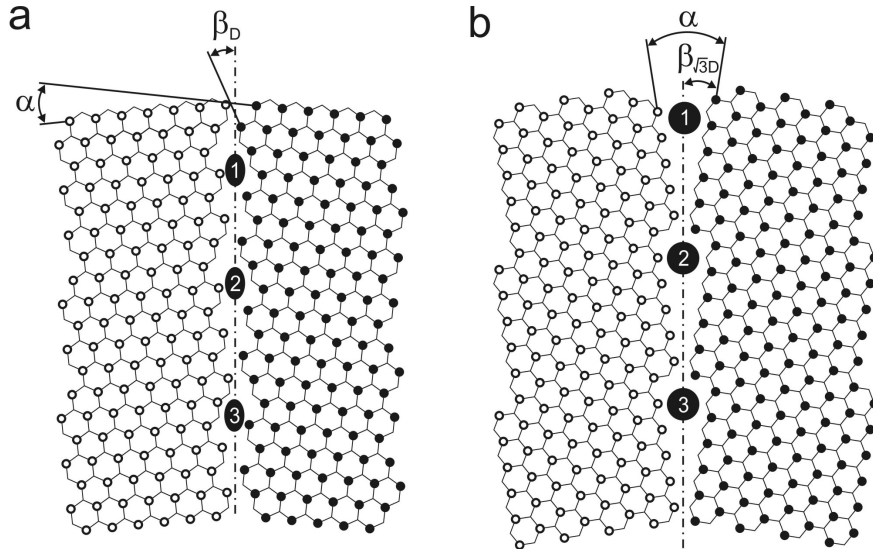


**Figure 2.4:** Schematic pictures of grain boundaries in graphite showing two possible superlattice periodicities  $D$  (a) and  $\sqrt{3}D$  (b). Periodicities within the grain boundaries and angles between the graphite grains have been chosen according to STM observations  $\alpha = 12^\circ$ ,  $D = 1.18$  nm (a) and  $\alpha = 18^\circ$ ,  $\sqrt{3}D = 1.36$  nm (b).

## 2. Grain boundaries in graphite

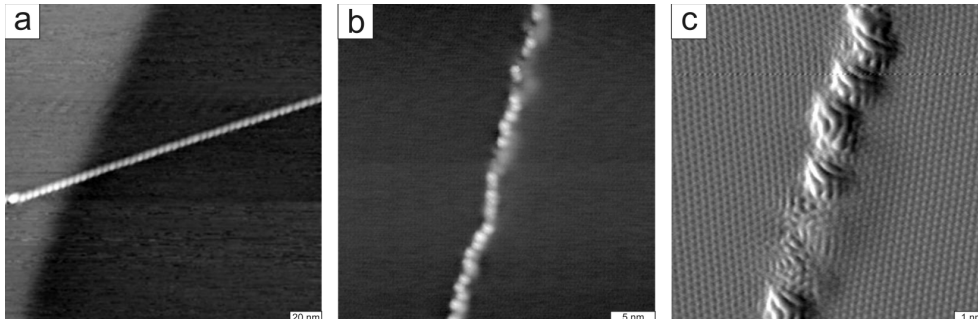


**Figure 2.5:** STM images of straight (a) and undulating (b) grain boundaries on HOPG. Scanning parameters: (a)  $200 \times 200 \text{ nm}^2$ , (b)  $37 \times 37 \text{ nm}^2$ ,  $U = 1 \text{ V}$ ,  $I = 0.3 \text{ nA}$ . (c) Current STM image of a grain boundaries with a defects in the periodic structure, zoomed in the center part of figure (a). Scanning parameters:  $10 \times 10 \text{ nm}^2$ ,  $U = 1 \text{ V}$ ,  $I = 0.3 \text{ nA}$ .

cleaving process. If an edge would be created from the grain boundary by cutting it into half, the edges would have segments of zigzag or armchair edge of the maximum length as the superlattice periodicity  $D$  or  $\sqrt{3}D$ . Previous STM studies of step edges on graphite has found a short length of zigzag edges (up to 2 nm) alternated by armchair segments, while the energetically more stable armchair edges had lengths up to hundred nanometers [38]. We have observed periodicities of the grain boundaries between 0.5 to 10 nm, which are in accordance with the observation of the short length of alternating zigzag and armchair edges, which could have been created out of grain boundaries.

Although most of the grain boundaries show a periodic structure over large nanometer distances, see figure 2.5(a), some of them exhibit undulating structure as shown in figure 2.5(b). This irregular structure is caused mostly by alternation of  $\beta_D$  and  $\beta_{\sqrt{3}D}$  direction, by which a change in periodicities  $D$  and  $\sqrt{3}D$  is induced. Nevertheless, there are also imperfections within grain boundaries. An example of a defect in the periodic structure of a grain boundary is shown in figure 2.5(c). This observation eliminates the possibility that a periodic structure of grain boundaries is produced by electron interference between free electrons waves from two different grains. It would be also difficult to construct such a high corrugation at the grain boundary, which is 15 times larger than the graphite lattice corrugation, taking into account only interference effects.

### 2.3.2 Electronic structure of grain boundaries

Scanning tunneling spectroscopy has been measured on grain boundaries and on a clean graphite surface for comparison. Two fundamentally different STS curves have

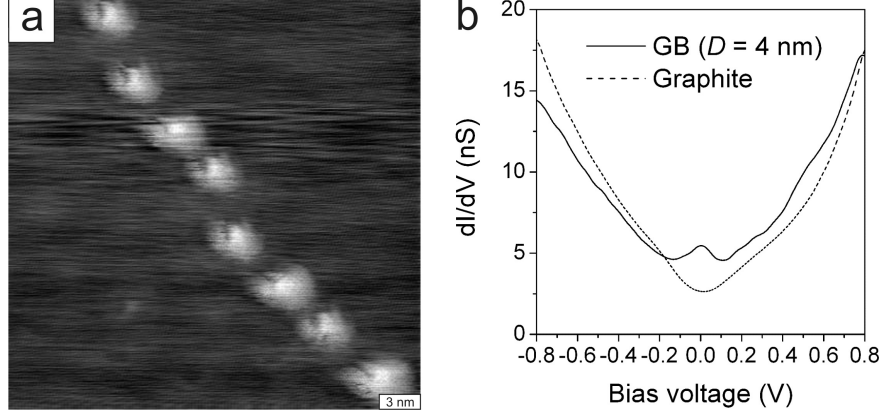


**Figure 2.6:** (a) STM of a grain boundary  $D = 4$  nm and (b) STS measured on top of the grain boundary and on the clean graphite surface. The grain boundary displays one localized states at the Fermi energy. Scanning parameters: (a)  $30 \times 30$  nm<sup>2</sup>,  $U = 1$  V,  $I = 0.06$  nA; (b)  $U = 0.26$  V,  $I = 0.5$  nA.

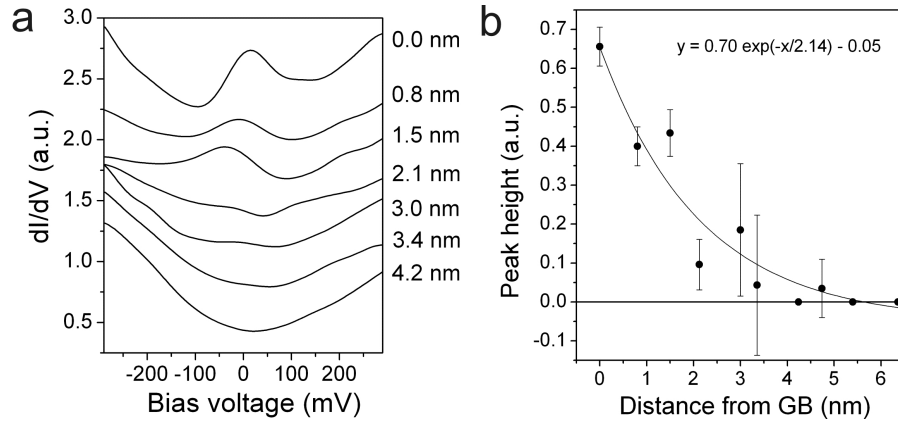


**Figure 2.7:** (a) Decay of the localized peak at the Fermi energy as the function of the distance from the grain boundary (figure 2.6). The  $dI/dV$  curves were vertically shifted for clarity. (b) Height of the localized state versus distance from the grain boundary (GB) after subtraction of the background graphite signal. The error bar denotes the width of the Gaussian peak.

been observed for grain boundaries with small and large superlattice periodicities.

An example of grain boundaries with a large periodicity  $D = 4$  nm is shown in figure 2.6(a). The grain boundary is composed of separated hillocks, which are 0.5 nm in height and around 4 nm in diameter. In figure 2.6(b), two  $dI/dV$  spectra measured on the top of a grain boundary and on the clean graphite surface are shown. STS spectra on grain boundaries exhibit an additional localized state at the Fermi energy,

## 2. Grain boundaries in graphite

which is not seen on the clean graphite surface. Decay of the localized peak at the Fermi energy as the function of the distance from the grain boundary is shown in figure 2.7. The  $dI/dV$  curves were vertically shifted for clarity in the figure 2.7(a). STS curves on the grain boundary exhibit a clear peak formation, which flattens out farther from the grain boundary and transfers into a depression far away ( $\approx 4$  nm), where a typical STS curve of graphite is observed. The position of the peak is not positioned always directly at the Fermi energy but is fluctuating around ( $\pm 25$  mV). This can be caused by an experimental error mainly due to room temperature and a drift. The peak height of the localized state have been determined by subtraction of the background graphite  $dI/dV$  spectrum measured at the large distance from the grain boundary. The result is demonstrated in figure 2.7(b). The peaks have been fitted by a Gaussian curve and its width  $\sigma$  is plotted as the error bar. An exponential curve has been fitted through the points ( $R^2 = 0.92$ ).

In figure 2.8, STM of a grain boundary with a "small" periodicity  $D = 2.6$  nm and its corresponding STS are shown.  $dI/dV$  spectra measured on the top of a grain boundary exhibit two localized states at  $-0.27$  V and  $0.4$  V. These states are not observed on the clean graphite surface. The extensions of the localized states measured along points in figure 2.8(a) are illustrated in figure 2.9. The peak height has been determined by fitting a Gaussian curve after subtraction of a background signal by an exponential function. The error bar represents  $\sigma$ , the width of the Gaussian peak. Both localized states at  $-0.27$  V and  $0.4$  V extend up to a large distance  $4$  nm, where no clear localized peaks are observed. The measured points have been fitted by expo-

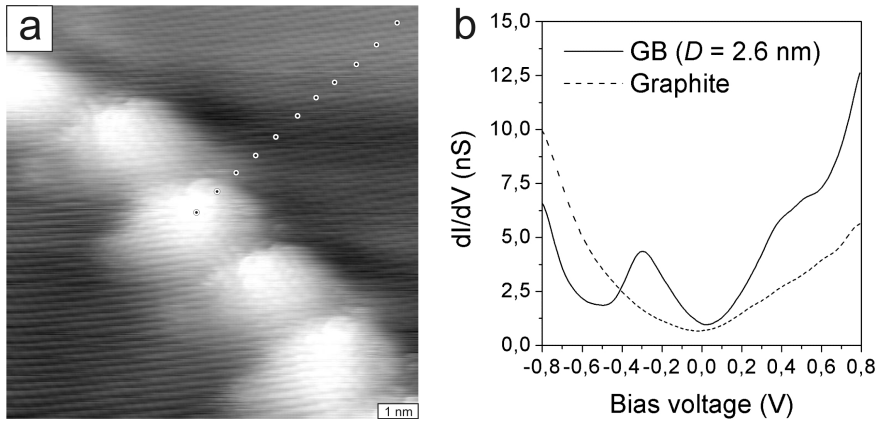


**Figure 2.8:** a) STM of a grain boundary  $D = 2.6$  nm and (b) STS measured on top of the grain boundary and on the clean graphite surface. The grain boundary displays two localized states at  $-0.27$  V and  $0.4$  V. Scanning parameters:  $13 \times 13$  nm<sup>2</sup>,  $U = -0.53$  V,  $I = 0.5$  nA.

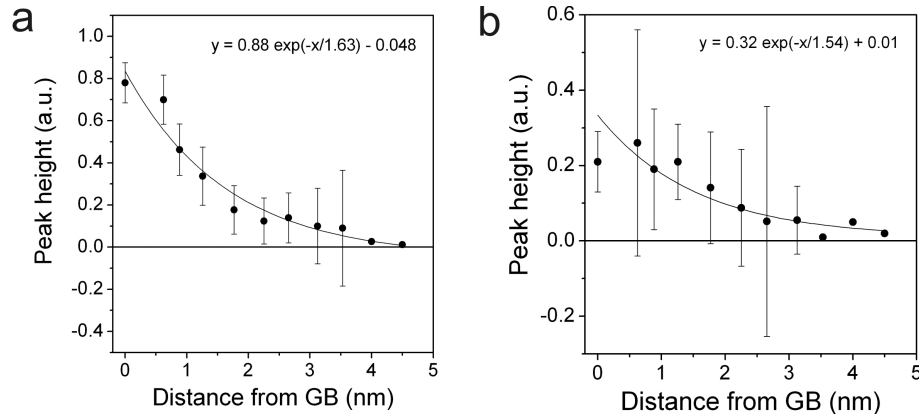


**Figure 2.9:** Height of the localized states at  $-0.27$  V (a) and  $0.4$  V (b) from STS curves (figure 2.6) versus distance from the grain boundary (GB). STS spectra were measured along points in figure 2.6(a). The error bar determines  $\sigma$ , the width of the Gaussian peak.

ponential curves with  $R^2 = 0.95$  (a) and  $R^2 = 0.87$  (b) in figure 2.9. Both fits resulted in comparable fitting parameters. Especially, the factors in the exponential functions give very similar values 1.63 and 1.54 for the states at  $-0.27$  V and  $0.4$  V, and 2.14 for the exponential decay function of the peak observed at the Fermi energy in figure 2.7.

Positions of localized states measured on 15 different grain boundaries have been analyzed and plotted against their superlattice periodicity as shown in figure 2.10. Two localized peaks around the Fermi energy are observed on grain boundaries with small superlattice periodicities ( $< 4$  nm). The localized peaks are predominantly distributed around  $-0.2$  eV in the filled states and around  $0.4$  eV in the empty states. However, grain boundaries with larger periodicities ( $> 4$  nm) display only one localized state at the Fermi energy. Similarly, one peak at the Fermi energy has been observed with STS on a point defect naturally occurring in graphite [5] and on a short zigzag edge on graphite [38]. So, the tops of grain boundaries with large periodicities demonstrate electronic properties like solitary defects in graphite.

Various point defects in graphene and graphite have been studied theoretically before [13–26, 28]. As a consequence of the presence of topological defects, the electronic structure of graphene is significantly modified. Generally, defects in the carbon honeycomb lattice give rise to formation of quasilocalized electron states around the Fermi energy [19, 22]. These states extend over several nanometers around the defects forming characteristic  $(\sqrt{3} \times \sqrt{3})R30^\circ$  superstructures as has been observed with STM around grain boundaries (see figure 2.3) and other defects [29–33].

Single-atom vacancies are one of the simplest possible defects in graphene lattice

## 2. Grain boundaries in graphite

---

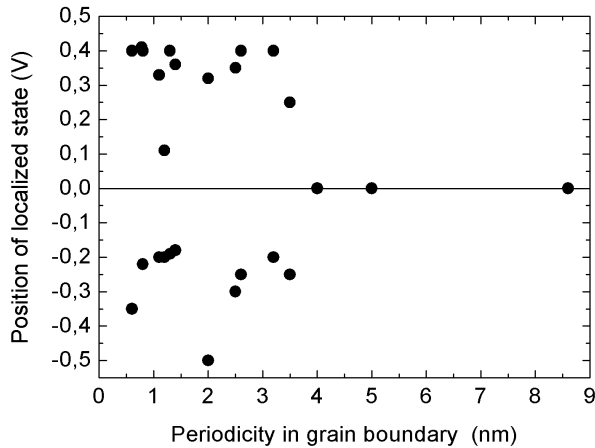


**Figure 2.10:** Positions of localized states measured on 15 different grain boundaries plotted against their superlattice periodicity.

and therefore have been the most studied in literature [13–20]. A single-atom vacancy is a defect in which one carbon atom is removed from the  $\pi$  conjugation network of the graphene sheet. This leads to two possibilities: either the disrupted bonds remain as dangling bonds or the structure undergoes a bond reconstruction in the vicinity of the vacancy, with several possible outcomes [14]. In either case, a slight local distortion of the lattice is expected. It was shown that single-atom vacancies lead to creation of quasilocalized electron states at the Fermi energy [18]. Since graphene is a zero band gap semiconductor with a DOS vanishing at the Fermi energy, these states are created exactly at the Fermi level. A similar situation was observed in extended defects consisting of a chain of boundary defects in graphene [19], which also formed localized states at the Fermi energy. In the absence of electron-hole symmetry, these states induce transfer of charge between the defects and the bulk leading to phenomenon called self-doping [22]. The self-doping of defects is in accordance with an increased charge DOS at the grain boundaries observed by STM. In the study of periodically closely spaced vacancies lines on graphite sheet it was found that they behave as metallic waveguide with a high density of states near the Fermi level [28] showing similarities to grain boundaries in graphite, which are consisting of planes of periodically repeating defects.

Since graphene systems have low electron densities at the Fermi energy, electron-electron interactions play an important role as recent experiments showed [39]. In the presence of a local repulsive electron-electron interaction the localized states will become polarized, leading to the formation of local moments [19]. This has

been illustrated in DFT studies of point defects in graphite such as vacancies and hydrogen-terminated vacancies [18]. These defects revealed to be magnetic having a local magnetic moment  $1.12\text{-}1.5\mu_B$  [20]. Spin polarized DOS of these systems showed two strongly spin polarized impurity states in the empty and filled states [20]. Saturation of a vacancy by hydrogen caused small suppression of magnetic moment to  $1\mu_B$  [20]. In another theoretical work, the influence of adsorption of H, O and N atoms on vacancies have been studied [24]. Only the adsorption of oxygen fully quenched the magnetic moment on the vacancy, while both H and N atoms supported the magnetism of vacancies [24]. The fact that magnetism does not vanish upon adsorption of other species has important consequence that magnetism in graphene materials does not require presence of highly reactive unsaturated dangling bonds.

The role of different distances between single vacancies has been studied in the DFT study of an 3D array of single vacancies in graphite [25]. Different sizes of supercells containing single vacancies have been constructed [25]. Two spin polarized states have been formed for small supercells, supporting ferrimagnetic order up to the distance 1 nm among the vacancies. The  $5 \times 5 \times 1$  supercell (1.23 nm separated vacancies) did not show a net magnetic moment in graphite and a single localized peak around Fermi energy has been observed in spin polarized LDOS. In graphene, the  $5 \times 5$  supercell exhibited still a net magnetic moment of  $1.72 \mu_B$  [25]. In another study of periodically distributed vacancies in graphene [27], a ferromagnetic ground state has been found for unexpectedly large defect separations  $25 \text{ \AA}$ . However, the system showed semiconducting properties in contrast to metallic behavior in the calculation of Faccio *et al.* [25].

Our experimental results on grain boundaries show very similar results to the theoretical predictions of Faccio *et al.* [25]. Periodically repeating defects in grain boundaries exhibit metallic properties. Moreover, one single localized peak is observed for distances larger than 4 nm between the defects, while two peaks are visible for smaller distances. In order to maintain magnetic interaction over such a large distance, an indirect exchange interaction between defects has to be involved. More detailed study of magnetic properties of graphite and grain boundaries in particular will be discussed in chapter 3, where magnetic force microscopy and bulk magnetization measurements are presented.

Another origin of the two principally different DOS for grain boundaries could be the different structure of point defects in grain boundaries having smaller and larger superlattice periodicities. Point defects in graphite can exist in several forms, such as single and multiple vacancies, interstitials, Stone Wales defects and other more complicated point defects. All of them can essentially occur in grain boundaries. Moreover, they can be saturated by different atoms like hydrogen, oxygen or nitrogen.



## 2. Grain boundaries in graphite

---

Using only STM measurement, it is impossible to extract the exact atomic structure of the defect. Nevertheless, the shape and the symmetry of the charge modulation around the defects reflects its structure like it has been shown in the theoretical study of a single atomic and double atomic defects in graphene [21]. The single atomic defect resulted in a simple trigonal symmetry in the charge modulation around the defect, while double atomic defect demonstrated two fold symmetry. From this point of view, grain boundaries contain more complicated point defects as seen in figure 2.3. In order to discern between the two proposed possibilities for diverse DOS of grain boundaries an appropriate calculation has to be done, which is going to be difficult especially for grain boundaries with large periodicities. Another option is a direct experimental proof of magnetic properties of grain boundaries with spin-polarized STM or an indirect evidence, which will be presented in following chapter 3.

### 2.3.3 Defects as a template for preferential absorption

It was shown in the previous section 2.3.2 that grain boundaries on the graphite surface possess localized states. These states can for example be utilized as a bonding state for adsorbing other molecules or clusters. Self-assembly and selective deposition through templates appears to be one of the promising ways forward the fabrication of low-dimensional nanostructures [40,42]. An alternative way is using atomic or molecular manipulation with STM [41]. However, this process is usually restricted to low temperatures and has very limited fabrication speed. While atomic steps and defects on surfaces of a solid substrate serve as a class of natural templates for generating supported one-dimensional nanostructures [42]. Grain boundaries exhibiting 1D superlattices have additional advantages of almost no apparent height and possibility of choosing the 1D periodicity from range of 0.5 nm to 10 nm. Atomic chains with different separations between atoms could be created in this way at low temperatures.

In order to check the principle of preferential absorption on grain boundaries of HOPG, a small amount of Ni has been thermally evaporated onto the HOPG sample at room temperature. Ni has been chosen because the interaction between Ni nanoparticles and various carbon materials has both fundamental and commercial importance [43]. Ni nanoparticles are one of the most important catalysts for the formation of carbon nanotubes, as well as for the high-pressure synthesis of commercial diamonds [43].

In figure 2.11, STM images of 10% coverage of Ni on graphite surface are manifested. Ni clusters have diameters around 4 nm and height of 2 nm. They are preferentially adsorbed around step edges creating a wire like structure as it was reported in previous studies [42–44]. However, not all the wires of Ni clusters are arranged along the step edges. Step edges cannot cross each other because graphite

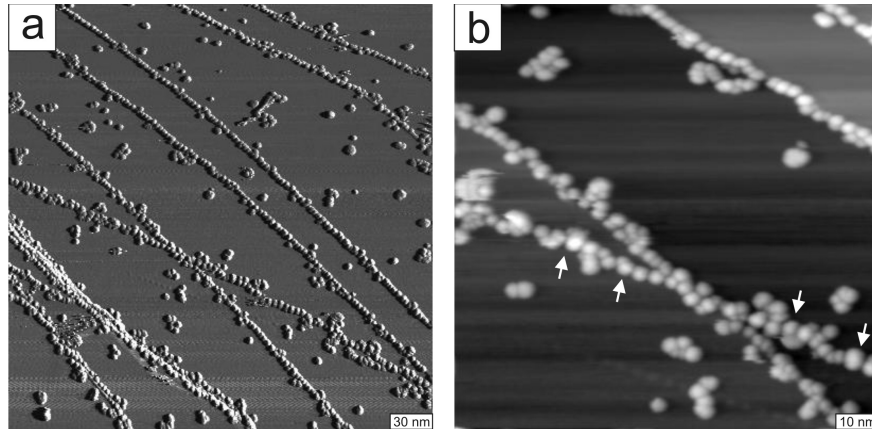


**Figure 2.11:** STM images of Ni clusters on HOPG. (a) A current STM image of a  $300 \times 300 \text{ nm}^2$  region on the HOPG surface, where step edges and grain boundaries are decorated with Ni clusters. (b) A STM topography image depicting a grain boundary, which is marked by arrows. The image is a zoom from figure (a). Scanning parameters:  $107 \times 107 \text{ nm}^2$ ,  $U = 0.5 \text{ V}$ ,  $I_t = 0.2 \text{ nA}$ .

is layered material. Therefore, a wire marked by arrow in figure 2.11(b) is a grain boundary decorated by Ni clusters. This shows that grain boundaries successfully act as 1D templates for preferential adsorption of clusters. At low temperatures, when the diffusion of the atoms is hindered, smaller clusters or atoms can be deposited on the surface. In such a way a 1D chain of magnetic atoms can be created with any predefined distances in range of 0.5 nm to 10 nm.

#### 2.3.4 Characterization of STM tips with the aid of grain boundaries

Grain boundaries exhibit a distinct sign in STM not only as one-dimensional superlattices with a nanometer separation but also as defects with a large extension of their electron states in the  $z$  direction perpendicular to the graphite surface. This extension of electron states has been shown by the difference in the apparent height of grain boundaries in STM and AFM (see figure 2.1). The height of grain boundaries was found  $< 0.3 \text{ nm}$  in AFM, whereas it reached much higher values in STM up to 1.5 nm. The difference between these two heights can be contributed to electron states of grain boundaries, which are protruding up to 1.2 nm distance above the graphite surface. Due to this large extension of electronic states, grain boundaries can be employed in characterization of STM tips while scanning HOPG surfaces.

In figure 2.12, two subsequent STM images of a grain boundary are shown. The first image (a) represents a grain boundary, which does not demonstrate its usual

## 2. Grain boundaries in graphite

---

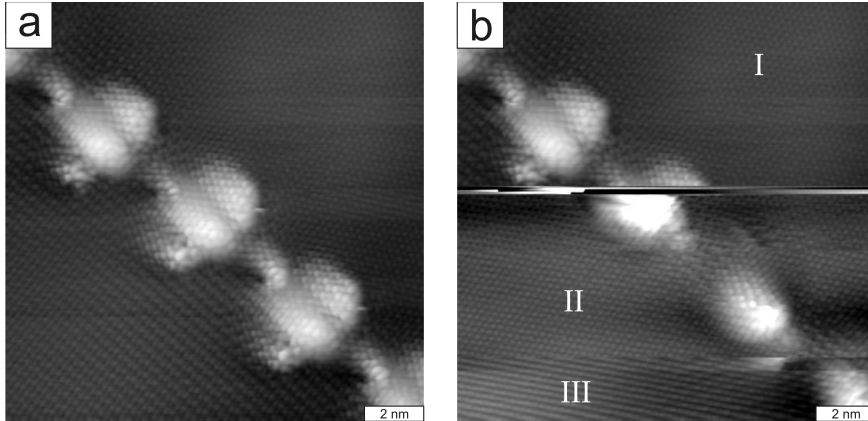


**Figure 2.12:** STM images of a grain boundary on HOPG (a) before tip change and (b) after tip change in between regions I and II. Scanning parameters:  $10 \times 10 \text{ nm}^2$ ,  $U = 0.5 \text{ V}$ ,  $I = 0.3 \text{ nA}$ .

simple "chain of beads" like structure as it was shown in previous STM images in figure 2.3. Instead, beads are composed of four smaller hillocks that repeat along the grain boundary. In the second figure 2.12(b), the STM tip has been deliberately changed by a voltage pulse at a location in between regions I and II. Another unprompted change of the tip has happened in between regions II and III. Interestingly, atomic resolution of the graphite surface has been obtained in all three regions, giving a clear signature of sharp STM tips in all three regions. However, the multiple internal structure of the grain boundary in region I indicates scanning with a multiple STM tip. From many measurements on grain boundaries, it can be concluded that the region II shows properly internal structure of grain boundary consisting only of one hillock without additional internal features. Therefore, the STM tip in region II has a symmetric conic shape at the apex and the grain boundary in figure 2.12(a) has been scanned with a multiple tip consisting of four sharp protrusions. Such a multiple tip would not be recognized on the flat graphite surface but it could contribute to tunneling if for instance molecules are deposited on the surface. Thus, grain boundaries on HOPG serve as a very fine tool to characterize the shape of very end of the STM tips.

Statistically, Pt/Ir tips exhibit more often multiple tips in comparison with W tips as was deduced from many performed STM measurements on HOPG. The reason lies most probably in the preparation method of the STM tips, which assures better defined tip geometries for W tips than Pt/Ir tips. W tips have been prepared by electrochemical etching, where the the material of a W wire is etched away homogeneously from the wire perimeter creating thus conical shaped tips. On the other hand

Pt/Ir tips have been produced by mechanical cutting, where a tip is produced by a combination of a pulling and cutting process which results in undefined tip geometries consisting of many micro tips.

Since graphite is commonly used for deposition of various molecules and biological species, it is substantial to understand the origin of different features such as superlattices on graphite surfaces in order to properly distinguish between deposited material and the structures of a clean graphite surface. HOPG has been the subject of numerous studies by STM. It has been shown that different structures can be observed by STM on freshly cleaved HOPG surfaces upon no deposition has occurred [45–47]. Next to the most common features such as large terraces separated by atomic steps, one can observe features like graphite strands, fiber clusters, ridges formed from steps, folded flakes, broken pieces and another periodic features such as 2D Moiré patterns or 1D superlattices of grain boundaries that meander across the graphite surface. These features can cause ambiguities when this surface is used as a substrate for study of molecular or biological materials. Especially, superlattices showing large-periodicity in the form of large hexagonal arrays or 1D chains could mimic the appearance of 2D arrays of protein molecules or 1D strands of DNA or molecules that have been deposited onto HOPG [45]. Multiple STM tips make the situation even more complicated, therefore one has to be very careful in analyzing data on graphite surfaces upon adsorption other molecules especially at low concentrations.

## 2.4 Conclusions

In conclusion, a systematic scanning tunneling microscopy and spectroscopy study of grain boundaries in highly oriented pyrolytic graphite have been performed. Different grain boundary geometries have been characterized with a focus on their structural and electronic properties. Grain boundaries showed a periodic structure and an enhanced charge density compared to the bare graphite surface. Two possible periodic structures have been observed along grain boundaries. A geometrical model producing periodically distributed point defects on the basal plane of graphite has been proposed to explain all observed structures of grain boundaries. Scanning tunneling spectroscopy revealed two localized states for the grain boundaries having small periodicities ( $< 4$  nm), while a single localized state at the Fermi energy has been observed for larger periodicities, indicating a long-range interaction among point defects within a grain boundary. Moreover, grain boundaries have been used as binding sites for selective deposition by thermal evaporation creating an 1D template and as a useful tool to characterize STM tips on the graphite surface.

### Bibliography

- [1] K. S. Novoselov, A. K. Geim, S. V. Morozov, D. Jiang, Y. Zhang, S. V. Dubonos, I. V. Grigorieva, and A.A. Firsov, *Science* **306**, 666 (2004).
- [2] K. S. Novoselov, A. K. Geim, S. V. Morozov, D. Jiang, M. I. Katsnelson, I. V. Grigorieva, S. V. Dubonos, and A. A. Firsov, *Nature* **438**, 197 (2005).
- [3] C. Berger, Z. Song, T. Li, X. Li, X. Wu, N. Brown, C. Naud, D. Mayou, A.N. Marchenkov, E.H. Conrad, P.N. First, and W.A. de Heer, *Science* **312**, 1191 (2006).
- [4] W. T. Pong and C. Durkan, *J. Phys. D* **38**, R329 (2005).
- [5] Y. Niimi, H. Kambara, T. Matsui, D. Yoshioka, and H. Fukuyama, *Phys. Rev. Lett.* **97**, 236804 (2006).
- [6] J. R. Hahn and H. Kang, *Phys. Rev. B* **60**, 6007 (1999).
- [7] A. Hashimoto, K. Suenaga, A. Gloter, K. Urita, and S. Iijima, *Nature* **430**, 870 (2004).
- [8] T. R. Albrecht, H. A. Mizes, J. Nogami, Sang-il Park, and C. F. Quate, *Appl. Phys. Lett.* **52**, 362, (1988).
- [9] C. Daulan, A. Derré, S. Flandrois, J. C. Roux, and H. Saadaoui, *J. Phys. I France* **5**, 1111 (1995).
- [10] P. Simonis, C. Goffaux, P. A. Thiry, L. P. Biro, Ph. Lambin, and V. Meunier, *Surf. Sci.* **511**, 319 (2002).
- [11] W. T. Pong, J. Bendall, and C. Durkan, *Surf. Sci.* **601**, 498 (2007).
- [12] F. Varchon, P. Mallet, L. Magaud, and J. Y. Veillen, *Phys. Rev. B* **77**, 165415 (2008).
- [13] V. M. Pereira, F. Guinea, J. M. B. Lopes dos Santos, N. M. R. Peres, and A. H. Castro Neto, *Phys. Rev. Lett.* **96**, 036801 (2006).
- [14] V. M. Pereira, F. Guinea, J. M. B. Lopes dos Santos, N. M. R. Peres, and A. H. Castro Neto, *Phys. Rev. B* **77**, 115109 (2008).
- [15] H. Amara, S. Latil, V. Meunier, Ph. Lambin, and J.-C. Charlier, *Phys. Rev. B* **76**, 115423 (2007).

## 2.4 Bibliography

---

- [16] A. A. El-Barbary, R. H. Telling, C. P. Ewels, M. I. Heggie, and P. R. Briddon, *Phys. Rev. B* **68**, 144107 (2003).
- [17] Y. Ferro and A. Allouche, *Phys. Rev. B* **75**, 155438 (2007).
- [18] P. O. Lehtinen, A. S. Foster, Y. Ma, A. V. Krasheninnikov, and R. M. Nieminen, *Phys. Rev. Lett.* **93**, 187202 (2004).
- [19] M. A. H. Vozmediano, M. P. Lopez-Sancho, T. Stauber, and F. Guinea, *Phys. Rev. B* **72**, 155121 (2005).
- [20] O. V. Yazyev and L. Helm, *Phys. Rev. B* **75**, 125408 (2007).
- [21] T. O. Wehling, A. V. Balatsky, M. I. Katsnelson, A. I. Lichtenstein, K. Scharnberg, and R. Wiesendanger, *Phys. Rev. B* **75**, 125425 (2007).
- [22] N. M. R. Peres, F. Guinea, and A. H. C. Neto, *Phys. Rev. B* **73**, 125411 (2006).
- [23] N. M. R. Peres, F. Guinea, and A. H. C. Neto, *Phys. Rev. B* **72**, 174406 (2005).
- [24] R. Y. Oeiras, F. M. Araújo-Moreira, N. Veríssimo-Alves, R. Faccio, H. Pardo, and A. W. Mombrú, (unpublished) arXiv:0606533 (2006).
- [25] R. Faccio, H. Pardo, P. A. Denis, R. Yoshikawa Oeiras, F. M. Araújo-Moreira, M. Veríssimo-Alves, and A. W. Mombrú, *Phys. Rev. B* **77**, 035416 (2008).
- [26] J. J. Palacios, J. Fernández-Rossier, and L. Brey, *Phys. Rev. B* **77**, 195428 (2008).
- [27] L. Pisani, B. Montanari, and N. M. Harrison, *New J. Phys.* **10**, 033002 (2008).
- [28] L. A. Chernozatonskii, P. B. Sorokin, E. É. Belova, J. Brüning, and A. S. Fedorov, *JETP Letters* **84**, 115 (2006).
- [29] H. A. Mizes and J. S. Foster, *Science* **244**, 559 (1989).
- [30] K. F. Kelly, D. Sarkar, G. D. Hale, S. J. Oldenburg, and N. J. Halas, *Science* **273**, 1371 (1996).
- [31] J. G. Kushmerick, K. F. Kelly, H.-P. Rust, N. J. Halas, and P. S. Weiss, *Phys. Chem. B* **103**, 1619 (1999).
- [32] P. Ruffieux, O. Gröning, P. Schwaller, L. Schlapbach, and P. Gröning, *Phys. Rev. Lett.* **84**, 4910 (2000).
- [33] G. M. Rutter, J. N. Crain, N. P. Guisinger, T. Li, P. N. First, and J. A. Stroscio, *Science* **317**, 219 (2007).

## 2. Grain boundaries in graphite

---

- [34] P. Esquinazi, A. Setzer, R. Höhne, C. Semmelhack, Y. Kopelevich, D. Spemann, T. Butz, B. Kohlstrunk, and M. Lösche, *Phys. Rev. B* **66**, 024429 (2002).
- [35] P. Esquinazi, D. Spemann, R. Höhne, A. Setzer, K.-H. Han, and T. Butz, *Phys. Rev. Lett.* **91**, 227201 (2003).
- [36] P. Esquinazi and R. Höhne, *J. Magn. Magn. Mater.* **290-291**, 20 (2005).
- [37] A. V. Rode, E. G. Gamaly, A. G. Christy, J. G. Fitz Gerald, S. T. Hyde, R. G. Elliman, B. Luther-Davies, A. I. Veinger, J. Androulakis, and J. Giapintzakis, *Phys. Rev. B* **70**, 054407 (2004).
- [38] Y. Kobayashi, K. Fukui, T. Enoki, and K. Kusakabe, *Phys. Rev. B* **73**, 125415 (2006).
- [39] A. Grüneis, C. Attaccalite, T. Pichler, V. Zabolotnyy, H. Shiozawa, S. L. Molodtsov, D. Inosov, A. Koitzsch, M. Knupfer, J. Schiessling, R. Follath, R. Weber, P. Rudolf, L. Wirtz, and A. Rubio, *Phys. Rev. Lett.* **100**, 037601 (2008).
- [40] P. Gambardella, A. Dallmeyer, K. Maiti, M. C. Malagoli, W. Eberhardt, K. Kern, and C. Carbone, *Nature* **416**, 301 (2002).
- [41] M. F. Crommie, C. P. Lutz, and D. M. Eigler, *Science* **262**, 218 (1993).
- [42] M. P. Zach, K. H. Ng, and T. M. Penner, *Science* **290**, 2120 (2000).
- [43] D.-Q. Yang and E. Sacher, *J. Phys. Chem. B* **109**, 19329 (2005).
- [44] N. P. Young, J. Palfreyman, and Z. Li, *Small* **2**, 71 (2006).
- [45] C. R. Clemmer and T. P. Beebe, *Science* **251**, 640 (1991).
- [46] H. Chang and A. J. Bard, *Langmuir* **7**, 1143 (1991).
- [47] W. T. Pong, J. Bendall, and C. Durkan *Jpn. J. Appl. Phys.* **44**, 5443 (2005).

## Chapter 3

# Ferromagnetism in graphite

### 3.1 Introduction

Graphite has been considered solely as a diamagnetic material for a long time, showing the second largest diamagnetic susceptibility after superconductors. However, recent experiments have shown that ferromagnetic order is possible in different carbon-based materials, including graphite. Ferromagnetism with high Curie temperatures, well above room temperature, and very small saturation magnetization has been reported in various graphitic systems [1–7]. The role of different magnetic impurities on the measured ferromagnetism has been studied in diverse samples of highly oriented graphite (HOPG), Kish graphite, and nature graphite [3]. The magnetization results, however, showed no correlation with the magnetic impurity concentration [3]. Ferro- or ferrimagnetic ordering was demonstrated in proton-irradiated spots in highly oriented graphite [4, 5]. Magnetic force microscope study showed a magnetic signal specifically in an proton-irradiated region [5]. The intensity of this signal, measured by MFM at the surface, could be modified by application of an external magnetic field. Bulk ferromagnetic graphite with a high defect concentration has been prepared via chemical route reaching the saturation magnetization 0.58 emu/g [6]. Apart from that, ferromagnetism has been observed in other carbon-based materials such as polymerized fullerenes [8, 9], carbon nanofoam [10], proton irradiated thin carbon films [11], and nitrogen and carbon ion implanted nanodiamond [12]. All these observations suggest an inherent ferromagnetic behavior of carbon-based materials.

Several theoretical investigations have been carried out to explain magnetism observed in these systems. The origin of ferromagnetism was suggested to be attributed to the mixture of carbon atoms with  $sp^2$  and  $sp^3$  bonds resulting in ferromagnetic interaction of spins separated by  $sp^3$  centers [13]. Another theoretical calculation suggested magnetism in  $sp^2$  bonded carbon nanostructures that contain a negatively



### 3. Ferromagnetism in graphite

---

curved graphitic surface, introduced via the presence of seven- or eight-membered rings [14]. In nanometer scale graphite, the electronic structure is strongly affected by the structure of the edges. Fujita and coworkers proposed that the  $\pi$  electrons on a monohydrogenated zigzag edge might create a ferrimagnetic spin structure on the edge [15]. Recently, it has been shown in spin-polarized density functional theory calculations that point defects in graphite, such as vacancies and hydrogen-terminated vacancies, are magnetic [16–18]. Randomly distributed single-atom defects have demonstrated ferromagnetism in disordered graphite with preserved stacking order of graphene layers [19]. In a three-dimensional network of single vacancies in graphite, ferrimagnetic order has been developed up to 1 nm separation among the vacancies [20]. In graphene, the magnetic order remained even at larger distances between vacancies, which were arranged in a two-dimensional periodic array [18, 20, 21].

In this chapter, an experimental study of ferromagnetic order in highly oriented pyrolytic graphite (HOPG) is presented. A ferromagnetic signal is probed locally with magnetic force microscopy (MFM) along line defects such as step edges and grain boundaries on HOPG surfaces in section 3.3.1. Bulk magnetization measurements of HOPG at 5 K and 300 K using a superconductive quantum interference device (SQUID) magnetometer are demonstrated in section 3.3.2. Ferromagnetic order is observed in HOPG samples even at room temperature showing one order larger saturation magnetization in the direction along  $c$  axis. Different origins of the observed ferromagnetism are discussed in section 3.3.4, giving rise to a new model based on ferromagnetism of itinerant  $sp$ -electrons occupying narrow defect states.

## 3.2 Experimental

Samples of HOPG of ZYH quality were purchased from NT-MDT. The ZYH quality of HOPG with the mosaic spread  $3.5^\circ - 5^\circ$  has been chosen because it provides a high population of step edges and grain boundaries on the graphite surface. HOPG samples were cleaved by an adhesive tape in air and transferred into a scanning tunneling microscope (Omicron LT STM) working under ultra high vacuum (UHV) condition. The HOPG samples have been heated to  $500^\circ\text{C}$  in UHV before the STM experiments. STM measurements were performed at 300, 78 and 4 K in the constant current mode with mechanically formed Pt/Ir tips or W tips as was presented in previous chapter 2. The same samples have been subsequently studied by atomic force microscopy (AFM), magnetic force microscopy (MFM) and electrostatic force microscopy (EFM) in air using a Dimension 3100 scanning probe microscope (SPM) from Veeco Instruments. PPP-MFMR cantilevers made by NanoSensors and MESP cantilevers from Veeco Instruments with a hard magnetic material CoCr-coating film have been used

in the MFM tapping/lift mode. Magnetization of the magnetic coating films were  $M_t = 720 \text{ emu/cm}^3$  for MESP cantilevers and  $M_t = 300 \text{ emu/cm}^3$  for PPP-MFMR cantilevers with coercivity 300 Oe for both MFM tip coatings. Magnetic moment of the MFM tip is estimated to be  $10^{-13} - 10^{-14} \text{ emu}$  [22]. Magnetization measurements have been performed with a superconductive quantum interference device (SQUID) magnetometer at 5 K and 300 K. Surfaces of HOPG samples have been analyzed for impurities by low energy ion scattering (LEIS) by Calipso [23]. Particle induced x-ray emission (PIXE) have been used to detect impurities spatially in ppm range in the bulk HOPG material at the Cyclotron Laboratory of the Eindhoven University of Technology.

## 3.3 Results and discussion

### 3.3.1 Magnetic force microscopy

In figure 3.1, AFM, MFM and EFM images of the same area on the HOPG surface are shown. The AFM topography in figure 3.1a displays a surface with a high population of step edges, surface distortions, and defects. The MFM images in figure 3.1b and figure 3.1c were taken on the same place as the AFM image with a lift scan height of 50 nm, where long-range van der Waals forces are negligible and magnetic forces prevail. A magnetic signal is measured on most of the line defects, however, a step edge marked as A in figure 3.1a does not show a magnetic signal in the MFM image. On the other hand, two lines in the MFM image in figure 3.1b that are indicated as B and C do not show a noticeable height difference in the topography. The lines B and C are grain boundaries of HOPG. Their detailed AFM and STM study has been discussed in chapter 2.

In order to determine the character of the detected magnetic signal, the MFM tip has been magnetized in two opposite directions: pointing into (figure 3.1b) and out of the graphite surface plane (figure 3.1c). Since the MFM signal represents the phase shift between the probe oscillation and the driving signal due to a magnetic force acting on the tip, the dependence of the phase shift on the force gradient can be expressed by a simple form [22]

$$\Delta\Phi \approx -\frac{Q}{k} \frac{\partial F}{\partial z}, \quad (3.3.1)$$

where  $Q$  is quality factor and  $k$  is spring constant of the cantilever. Typical values of our MFM system give a minimal detectable force gradient in the order of  $100 \mu\text{N/m}$ ,  $Q = 200$  and  $k = 2.8 \text{ N/m}$ . For a true quantitative interpretation of MFM images it is necessary to have an exact knowledge of the geometry and magnetic properties of the tip and the substrate in order to express the force acting on the tip, which

### 3. Ferromagnetism in graphite

---

is difficult and has been achieved only in special cases [22]. Nevertheless, a qualitative analysis can be done according to expression 3.3.1, where a positive phase shift (bright contrast) represents a repulsive force between the tip and the sample, and a negative phase shift (dark contrast) manifests an attractive interaction relative to the background signal. Since the tip magnetized into the graphite surface plane has shown a bright contrast in figure 3.1b and the out of plane magnetized tip produced a dark phase contrast on the line defects in figure 3.1b, the orientation of the net magnetic moment in the defects stayed in the same direction, pointing out of the graphite surface plane. This shows a clear indication of ferromagnetic order at the defect sites at room temperature. In the case of paramagnetic order, a bright contrast would be detected in both directions of the magnetization of the tip because the local magnetic moments would align with the magnetic field of the tip, leading to attractive interaction. The same result would be valid if electric force gradients were detected due to charge accumulation at the step edges. Hence, the ferromagnetic order in the defects of the HOPG sample is the only plausible explanation for the detected MFM signal.

However, not all signals measured in the MFM showed to be sensitive to the reversal of the tip magnetization, in particular, areas with a different phase contrast. This is due to the metallic character of the magnetic coating film of the MFM tip, which probes electrostatic forces as well. EFM has therefore been measured on the same place with a Pt coated Si tip with a lift scan height of 20 nm (see figure 3.1d). A bright contrast is observed on the same places as in the MFM images, showing a bright contrast on the line defects and some of the areas of the graphite surface. Bright places represent regions of a higher electrostatic surface potential difference than dark regions in respect to the grounded EFM tip. Similar regions with a different surface potential have been measured in EFM and kelvin probe microscopy (KPM) on HOPG before [24,25]. This non-uniform potential distribution has been found to be caused by the mechanical stress induced during sample cleaving [25]. The highest inhomogeneity in the potential distribution has been found directly after cleavage of a HOPG sample that had been transferred to vacuum. This distribution changed slowly in time till it saturated to a stable potential distribution after few hours. Nevertheless, the inhomogeneities remained even after the surface relaxation, in particular on the defect structures [25]. Our experiments have been done on relaxed graphite surfaces, which have been heat-treated before in UHV. Thereby the MFM measurements represent a superposition of magnetic and electrostatic signals, where the magnetic signal is sensitive to the reversal of magnetization of the MFM tip, while the electrostatic signal is not, and forms only background signal in MFM measurements. By that the observed MFM line shapes in figure 3.1c, demonstrating dark depressions in the middle of the

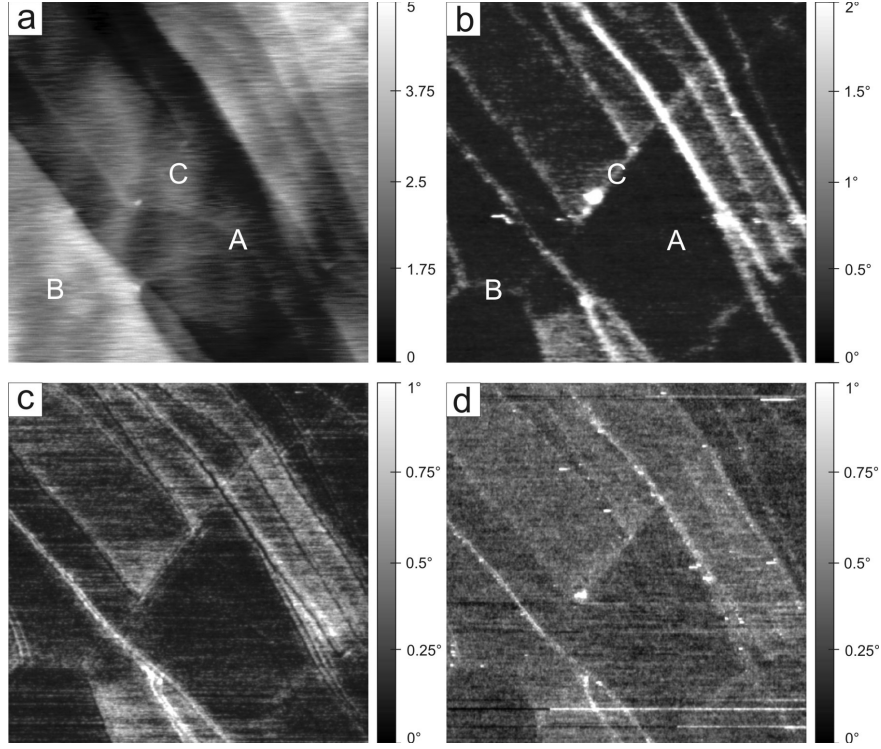


**Figure 3.1:** AFM (a), MFM (b) and (c), and EFM (d) images of the same area on a HOPG surface. MFM tip has been magnetized pointing into the graphite surface (b) and out of the graphite surface (c), respectively. Image parameters: scan area  $2 \times 2 \mu\text{m}^2$ , the MFM lift height  $h = 50 \text{ nm}$ , and the EFM lift height  $h = 20 \text{ nm}$ .

bright line profile, could be easily explained. In this image, the MFM tip has been magnetized out of the graphite surface, so the attractive magnetic forces have caused a dark contrast while repulsive electrostatic forces formed a bright contrast. After the reversal of the MFM tip magnetization in to the graphite sample (see figure 3.1b), only a bright phase contrast is observed demonstrating larger values of the phase shift than with opposite magnetization.

Similar observations of magnetism on defects in graphite have been reported recently using a different local probe technique [26]. In this study, magnetic field induced strains have been studied using a STM setup on HOPG samples in a magnetic field. It has been suggested that defects in graphite may be magnetic and magnetostrictive [26]. Magnetostriction occurs only in ferromagnetic materials and results in a change in the dimensions of the specimen due to strain when a magnetic field is applied. In this magnetostriction experiment [26], the magnetic field has been ap-

### 3. Ferromagnetism in graphite

---

plied parallel to the long axis of the sample that was held in a STM in air. Similar magnetoelastic displacements (3 nm) were observed on graphite step sites as for ferromagnetic wires, implying that the HOPG sample has nonzero magnetization [26]. The magnetostriction saturation has reached value around 100 Oe, which is comparable to saturation fields determined along graphene planes by SQUID magnetization measurements in reference [3] and by us as will be presented in following section.

#### 3.3.2 Superconductive quantum interference device magnetometer

The bulk magnetization of the HOPG samples has been measured with a SQUID magnetometer at 5 K and 300 K. A SQUID magnetometer is the most sensitive technique for measuring magnetic fields, capable of measuring flux changes that represents only a small fraction of a flux quantum ( $2.07 \times 10^{-15}$  Wb). Measurements in a DC SQUID magnetometer are done by moving a sample through the second-order gradiometer in the magnetic field produced by a superconducting magnet. The magnetic moment of the sample induces an electric current in the pick-up coil system. A change in the magnetic flux in these coils changes the persistent current in the detection circuit containing Josephson junctions. This signal is proportional to the magnetic moment of a sample in the magnetic field.

In figure 3.2, in-plane and out-of-plane ferromagnetic hysteresis loops of HOPG at 5 K are shown. The in-plane direction denotes a magnetic field applied along the graphene planes and in the out-of-plane direction the magnetic field was perpendicular to these planes. Linear diamagnetic background signals have been subtracted from the raw data, which are shown in the insets of figure 3.2. The magnetic susceptibility has been determined by a linear fit through the measured points at larger magnetic fields in the interval 1-3 T. The magnetic susceptibilities are  $\chi_{\parallel} = -5.4 \times 10^{-7}$  emu/g mT in the basal plane and  $\chi_{\perp} = -1.1 \times 10^{-5}$  emu/g mT along the  $c$  axis (perpendicular to graphene planes). The in-plane magnetization loops display a small saturation magnetization  $2.7 \times 10^{-3}$  emu/g, coercive field 7.7 mT, and remnant magnetization  $3.8 \times 10^{-4}$  emu/g. The out-of-plane magnetization measured along the  $c$ -axis manifests one order larger saturation magnetization 0.013 emu/g and similar coercive field 10 mT and remnant magnetization  $3.9 \times 10^{-4}$  emu/g as in the in-plane magnetization measurement. The result for the in-plane magnetization is comparable to SQUID measurements of HOPG reported by P. Esquinazi et al. [3], showing magnetic saturation in the order of  $10^{-3}$  emu/g. However, out-of-plane magnetization measurements have not been reported in this work and thus cannot be compared to our data.

SQUID magnetization measurements at 300 K are depicted in figure 3.3. The diamagnetic signal has been subtracted in the same way as for the measurements at

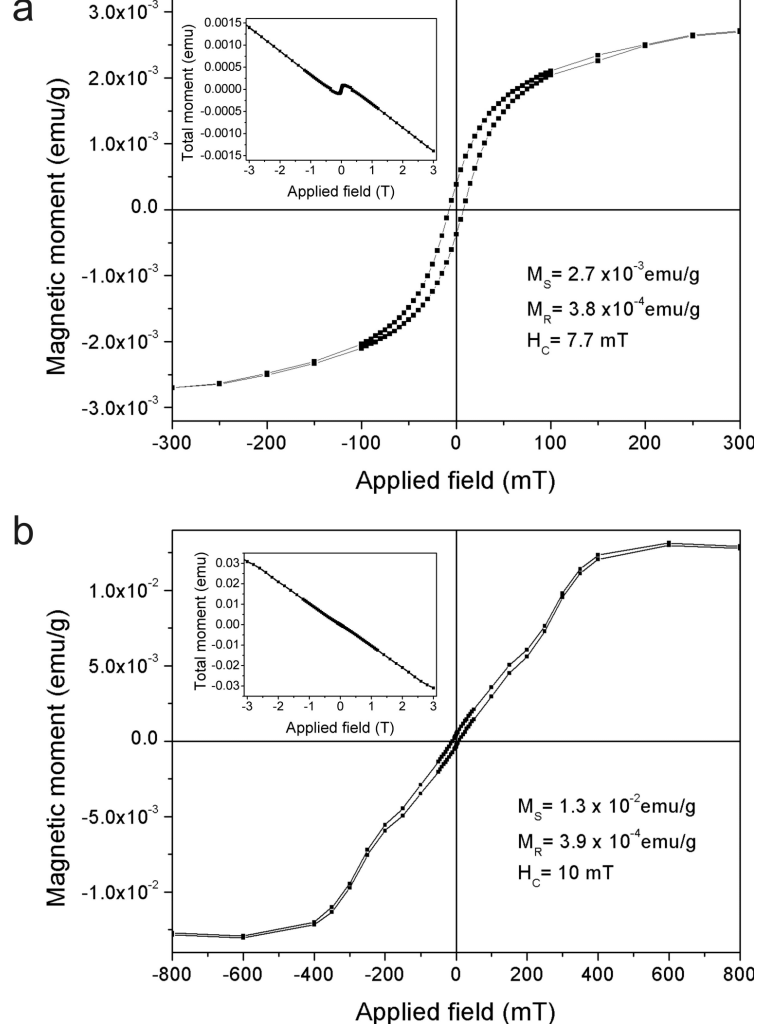


**Figure 3.2:** (a) In-plane SQUID magnetization and (b) out-of-plane magnetization measurements on HOPG at 5 K after subtraction of the diamagnetic signals. Insets show the data before subtraction of linear diamagnetic signals:  $\chi_{\parallel} = -5.4 \times 10^{-7}$  emu/g mT and  $\chi_{\perp} = -1.1 \times 10^{-5}$  emu/g mT.

5 K. The magnetic susceptibilities were found to be  $\chi_{\parallel} = -3.9 \times 10^{-7}$  emu/g mT and  $\chi_{\perp} = -6.8 \times 10^{-6}$  emu/g mT. The magnetization loops after the linear correction display ferromagnetic hysteresis as well as at 5 K. Magnetization in the in-plane alignment of the HOPG sample shows saturation magnetization  $2.5 \times 10^{-3}$  emu/g, coercive field 6.2 mT and remnant magnetization  $3.2 \times 10^{-4}$  emu/g. The magnetization loops measured along the  $c$ -axis display saturation magnetization  $2.2 \times 10^{-3}$  emu/g,

### 3. Ferromagnetism in graphite

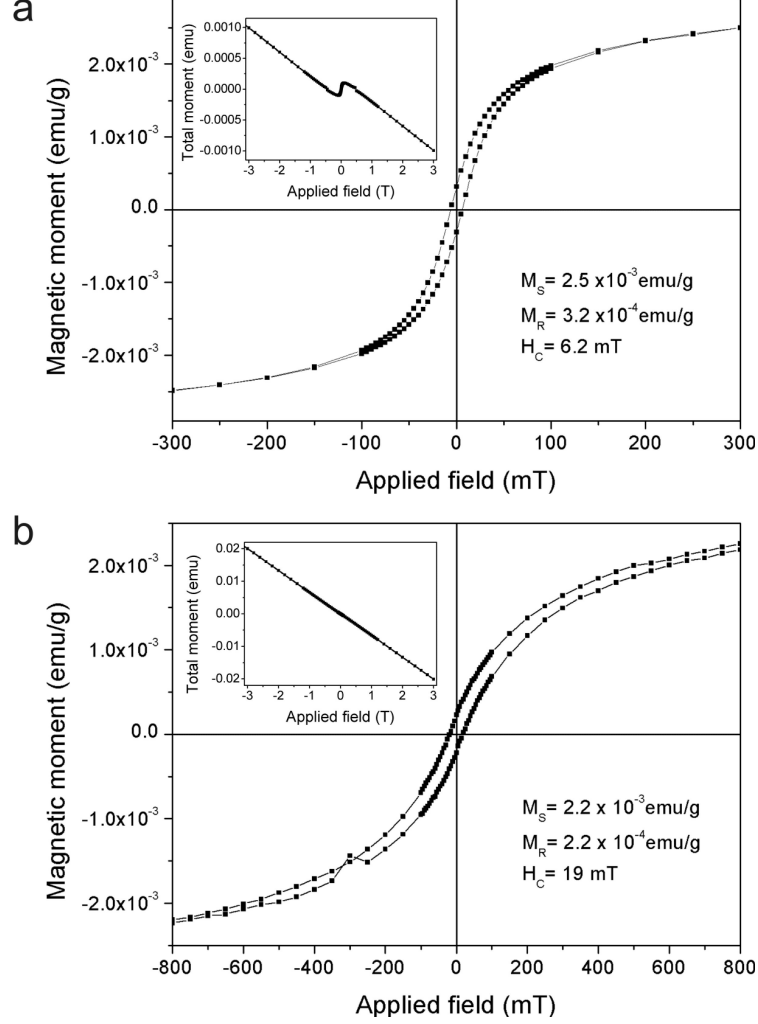


**Figure 3.3:** (a) In-plane SQUID magnetization and (b) out-of-plane magnetization measurements on HOPG at 300 K after subtraction of the diamagnetic signals. Insets show the data before subtraction of linear diamagnetic signals:  $\chi_{\parallel} = -3.9 \times 10^{-7}$  emu/g mT and  $\chi_{\perp} = -6.8 \times 10^{-6}$  emu/g mT.

coercive field 19 mT and remnant magnetization  $2.2 \times 10^{-4}$  emu/g.

Since the out-of-plane magnetization saturates at higher magnetic fields, it represents the hard axis and the in-plane direction represents the easy magnetic axis of the HOPG sample. The reason that the in-plane magnetization curves do not come to the same point at high fields is probably due to a misalignment of graphite planes with respect to the magnetic field, which could have resulted in small spikes at  $\pm 0.5$  T as can be seen in the inset of figure 3.3a. A proper alignment of a graphite sample plays

an important role mainly for the diamagnetic contribution, which possesses a two orders of magnitude smaller susceptibility in the in-plane than in the out-of-plane configuration. If a HOPG sample is not properly aligned an out-of-plane susceptibility contribution will be measured in the in-plane alignment. However, this can not be eliminated, even if the sample would be well aligned, because HOPG crystallites have an average misalignment from the  $c$ -axis. This misalignment is given by the mosaic spread  $3.5^\circ - 5^\circ$  of HOPG, which was determined by x-ray diffraction by the producer. An imperfect alignment can have also influence on the value of in-plane saturation magnetization, which demonstrates a slightly larger value at room temperature compared to 5 K. In the work of Esquinazi et al. [3], the value of saturation magnetization remained practically constant from 5 K to 500 K.

The magnetization curves of HOPG show a clear magnetic anisotropy. Anisotropy in a magnetic material is usually caused by a crystalline anisotropy through a spin-orbit coupling. However, this option can be excluded in our case because the spin-orbit coupling is small in graphite [27]. The second option is a shape anisotropy. For this reason, a twice longer HOPG sample has been analyzed by SQUID magnetometer. The magnetization curves on this sample gave rise to similar results as in figures 3.2 and 3.3. This means that the magnetic moments are localized because the demagnetizing field minimizing the energy by flux closure in the sample could not be changed by the sample geometry. In order to make any conclusions about source of the magnetic anisotropy, more studies are needed.

#### 3.3.3 Magnetic impurity characterization

The main question arising in studies of magnetism in carbon-based materials is related to the role of magnetic metallic impurities. HOPG samples, as they have been studied previously [3], contain a small fraction of magnetic elements. These elements can contribute to the measured magnetic signal and therefore it is very important to know their concentration in the HOPG samples in order to properly interpret the measured ferromagnetic signals in MFM and SQUID measurements. For this reason, the HOPG samples have been analyzed for impurity concentration by particle induced X-ray emission (PIXE) in the bulk material and by low energy ion scattering (LEIS) at the surface.

PIXE is a very sensitive technique used for determining the elemental composition of a material. In this method, a material is exposed to a proton beam with a high energy (a few MeV). The protons cause electrons within the atoms of the target to be excited from core shells producing X-rays which are specific to each element. Thus, analyzing the X-ray emission from the sample upon proton irradiation can be used to identify each element within the sample. By scanning the proton beam across the



### 3. Ferromagnetism in graphite

---

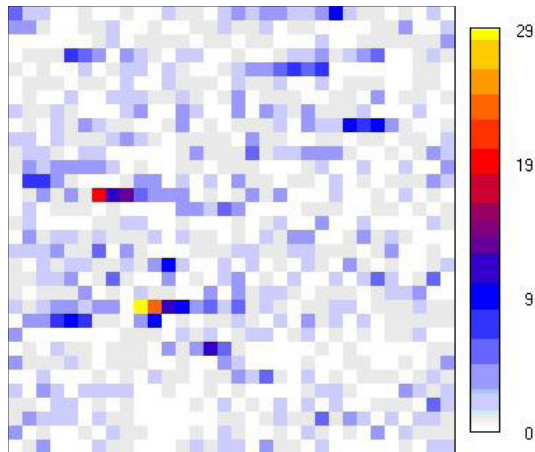


**Figure 3.4:** Fe-count distribution map on a  $0.3 \times 0.3 \text{ mm}^2$  area of HOPG with a beam current 200 pA. The vertical scale represents a number of detected photons having an energy specific to Fe. The averaged Fe signal over this area corresponds to concentration  $\approx 20 \mu\text{g/g}$ .

sample surface, concentration maps of each element can be acquired.

A concentration analysis by PIXE has been performed at the Cyclotron Laboratory of the Eindhoven University of Technology. The HOPG has been analyzed by 3 MeV protons that have a penetration depth of  $70 \mu\text{m}$  in carbon. The analysis was performed under the assumption that the concentrations of the elements in the sample do not change with a depth. Fe was found to be the main magnetic impurity in PIXE with average concentration  $\approx 20 \mu\text{g/g}$ . Other magnetic and metallic impurities were below the detection limit, which means  $< 1 \mu\text{g/g}$  for V, Cr, Mn, Ni, Co and Cu; and  $< 4 \mu\text{g/g}$  for Ti. In figure 3.4, a spatial distribution map of Fe in the HOPG sample is shown. The map reflects the Fe-count distribution on a  $0.3 \times 0.3 \text{ mm}^2$  area of a HOPG sample with a beam current 200 pA. From this image it can be seen that the Fe content in HOPG is not entirely uniformly distributed and it has a few hotspots. In these 10-20  $\mu\text{m}$  spots, the concentration is approximately 10 times higher than in the surrounding regions. However, only 3 hotspots can be seen on the  $0.3 \times 0.3 \text{ mm}^2$  area and the rest of the sample exhibits approximately uniform distribution of Fe.

In order to check the concentration of magnetic elements at the HOPG surface low energy ion scattering (LEIS) have been done. LEIS is a method highly sensitive to heavy elements at the sample surface. In this technique, a sample is bombarded with noble gas ions of a few keV. The energy of a noble gas ion that is backscattered by a surface atom is determined by the laws of conservation of energy and momentum, for a given primary energy and scattering angle. The energy spectrum of the scattered

ions is equivalent to a mass spectrum of the surface atoms. From the number of counts of specific mass, the concentration of elemental composition of the sample topmost surface layer can be determined. The LEIS experiments have been performed by Calipso [23]. However, no signal of Fe, Co, Ni elements was detected, which means that the concentration of all these elements is well below 100 ppm.

The concentration of 20  $\mu\text{g/g}$  Fe in our HOPG samples is comparable to found impurity concentration in HOPG samples by Esquinazi et al. [3]. In this study, several HOPG samples from different sources have been characterized for impurity concentration by PIXE. As a main magnetic impurity was found Fe with concentration ranging from 0.3 to 19  $\mu\text{g/g}$ . Other magnetic metallic impurities have been found similarly below 2  $\mu\text{g/g}$ . The magnetic signal has been compared with concentration of magnetic elements homogenously distributed in the samples. However, the measured magnetization of the HOPG samples did not show a correlation with the concentration of magnetic impurities [3]. We also believe that the measured content of Fe impurities in HOPG is not sufficient to produce the ferromagnetic signal shown by SQUID in figure 3.2. The amount of 20  $\mu\text{g/g}$  of Fe would contribute maximally  $4.4 \times 10^{-3}$  emu/g to the magnetization and for Fe or  $\text{Fe}_3\text{O}_4$  clusters, the magnetic signals would be even smaller [3]. Moreover, the assumption that all Fe is magnetically ordered is wrong as it has been shown experimentally in iron-rich graphite [2], where only about 38% of Fe has contributed to ferromagnetic signal.

MFM measurements showed the ferromagnetic signal specifically at step edges and grain boundaries on the HOPG surface. It can be expected that most of the impurities segregate just along grain boundaries or step edges at the surface. However, if the observed ferromagnetic signal had originated from magnetic impurities arranged along grain boundaries or step edges, all the magnetic impurities should have to be arranged along the line defects uniformly to produce homogenous signals in MFM, which is very unlikely. Nevertheless assuming so, one atom thick impurity line along all the defect lines in figure 3.1 would give rise to the concentration of approximately 500 ppm, which should be detectable with LEIS. Moreover, small clusters of magnetic impurities fitted within a monoatomic step height of 0.33 nm would not produce a ferromagnetic signal at room temperature but would be superparamagnetic. Mass selected iron clusters have shown the transition from the ferromagnetic to the superparamagnetic phase at a particle diameter of about 10 nm at room temperature [28]. In a recent experiment, a comparison between proton and iron irradiated graphite sample has been made to study the influence of Fe on magnetism observed in graphite [29]. A similar number of protons and iron-ions at similar energies have been used for comparison. The result showed that both could produce similar paramagnetic contributions depending on the implantation temperature, however only protons induced ferromagnetic effects [29],

### 3. Ferromagnetism in graphite

---

supporting that defects play a major role in ferromagnetism of irradiated graphite.

To conclude, concentration of 20  $\mu\text{g/g}$  of Fe has been found in HOPG samples by PIXE. This amount of iron can only partly contribute to the measured ferromagnetic signal in the bulk magnetization measurements in HOPG. Fe has been found to be homogeneously distributed in HOPG, wherefore it cannot account for the ferromagnetic signals observed in MFM at the line defects on HOPG surfaces. Hence magnetic impurities cannot explain fully the observed ferromagnetism in graphite, especially at room temperature.

#### 3.3.4 Interpretations of the measured magnetic signal

Several scenarios that predict the magnetism of carbon have been suggested in literature: (i) magnetism due to magnetic impurities in carbon materials or induced by a magnetic proximity effect at the impurities [2]; (ii) volume magnetism of an ideal structure that contains alternating  $sp^2$ - and  $sp^3$ -hybridized atoms [13]; and (iii) atomic-scale magnetism caused by structural imperfections and defects [14–20]. The first most obvious possibility of ferromagnetism in HOPG due to the magnetic impurities has been excluded after careful analysis of magnetic elements in HOPG by PIXE and LEIS in previous section. The second suggestion cannot be applied in graphite on large scale. Hence the defect-induced magnetism remains as the most plausible source of the shown-up ferromagnetic behavior in graphite. Since MFM has showed the ferromagnetic signal specifically along line defects on the HOPG surface, the main focus will be on these extended defects, but the role of point defects will be discussed as well.

Line defects occur naturally on graphite surfaces as edges and grain boundaries. Graphite edges have been extensively studied both theoretically [15, 30, 31] and experimentally [32–34]. There are two typical shapes for graphite edges: armchair and zigzag. Only zigzag edges are expected to give rise to the magnetic ordering due to the existence of the edge state at the Fermi energy [15]. Armchair edges do not possess such an edge state and are responsible for semiconducting properties in graphene nanoribbons [15]. STM experimental results on step edges of graphite, however, showed that zigzag edges are much smaller in length ( $\approx 2$  nm) than those of armchair edges and less frequently observed [34]. From this point of view, realistic edges on graphite are composed of an alternating sequence of longer armchair edges and shorter zigzag edges. This one-dimensional system could be paramagnetic or ferrimagnetic in the short-range due to local magnetic moments formed at zigzag edge fragments [15], but no long-range ferromagnetic order could be expected at room temperature. We rather believe that step edges are created on HOPG at places where bulk grain boundaries cross the surface. During the cleavage of the graphite crystal, grain boundaries are

the weakest points of the graphite crystal and step edges are created out of them on the newly formed HOPG surface. This has been confirmed by STM and AFM observations in figure 2.1, where grain boundaries continued as step edges. A step edge created in this way would have the same orientation and geometry as a grain boundary underneath.

Grain boundaries in HOPG have been studied in great detail in chapter 2. They are inevitable defects of graphite samples because of their polycrystalline character. They are formed between two rotated grains during the crystal growth. They extend over step edges and form a continuous network all over the graphite surface. Grain boundaries show a small or no apparent height in AFM (see figure 3.1). On the other hand, grain boundaries exhibit a very distinct sign in STM, where they appear as one dimensional superlattices with the height corrugation up to 1.5 nm (figure 2.2). The most prominent, however, are their electronic properties. Grain boundaries possess an enhanced charge density compared to the bare graphite surface as has been shown in section 2.3.1. Due to the charge accumulation they appear as bright lines in EFM (see figure 3.1). Grain boundaries possess localized states which are not observed on the clean graphite surface. STS of a grain boundary showed two strong localized states around the Fermi level for grain boundaries with periodicity  $< 4$  nm and one localized peak at the Fermi energy for periodicities  $> 4$  nm. Due to these localized states, grain boundaries could be of the origin of the observed ferromagnetism in graphite as will be explained in the following text.

Grain boundaries on graphite surfaces demonstrate themselves as periodically distributed point defects arranged in a one-dimension superlattice. In reality, they have a quasi two-dimensional character since they separate two or more three-dimensional graphite grains. Thus, grain boundaries are planes of periodically distributed point defects, where the distance between defects is determined by the angle between the graphene lattices in two neighboring graphite grains. The distance between defects in the direction perpendicular to the graphene planes is assumed to be identical to the distance between graphene planes 0.335 nm.

Point defects in graphene lattice have been studied extensively theoretically in recent years [16–21, 35–44]. The single-atom defects in the graphene lattice give rise to quasilocalized states at the Fermi level and to the formation of local magnetic moments [16–21, 35–39]. The common feature of these defects is that one or more carbon atoms are removed from the  $\pi$  conjugation network of the graphene sheet. The graphene lattice is a bipartite lattice, which is formed by two interpenetrating triangular sublattices of carbon atoms (labeled  $A$  and  $B$ ), such that the first neighbors of an atom  $A$  belong to the sublattice  $B$  and vice versa. The low-energy electronic structure of graphene is well described by a single-orbital ( $p_z$ ) nearest-neighbor hopping

### 3. Ferromagnetism in graphite

---

Hamiltonian [18,45]. When a defect is created in the  $A$  sublattice, only the  $p_z$  orbitals of the carbon atoms in  $B$  sublattice contribute to the quasilocalized state and vice versa. Inui *et al.* has proven that the existence of these zero energy (midgap) states has a sufficient condition in a finite sublattice imbalance  $N_A \neq N_B$  [46]. Because of the particle-hole symmetry, midgap states are half-filled for neutral graphene and the appearance of magnetic moments is expected (odd number of electrons) in analogy with Hund's rule in atomic magnetism [18]. The magnetic moments are not spread over the graphene sheet but are quasilocalized around the defect [17].

Since graphene systems have low electron densities at the Fermi energy, electron-electron interactions start to play an important role as recent experiments have shown [37,47]. These interactions cannot be described in the tight binding model. The Hubbard model extends the single-particle tight binding model by including the effect of Coulomb repulsion  $U > 0$  between two electrons on the same atomic site. Using the Hubbard model and the neutral bipartite lattice, Lieb has demonstrated that the total spin  $S$  of the ground state is given by  $2S = |N_A - N_B|$ , where  $N_A$  is a number of atoms in sublattice  $A$  and  $N_B$  in sublattice  $B$  [48]. Thus, Lieb's theorem states that a sublattice unbalance causes always a finite total magnetic moment in the graphene lattice. This imbalance can be induced for instance by single-atom vacancies, which remove only one atom of the sublattice, or by multiple vacancies where more  $A$  or  $B$  atoms are removed.

In single atom vacancies, the ground state has one unpaired electron and according to Lieb's theorem spin 1/2 for  $U = 0$  [18]. Although this picture looks too simplified to be valid for realistic single-atom vacancies in graphene, it yields very good agreement with both mean-field Hubbard and density functional theory (DFT) models [16–19]. In graphene, a single-atom vacancy is created by removing one atom from the graphene lattice, whereupon each of the three neighboring atoms is left with one dangling  $sp^2$  bond. It has been found in DFT calculations that this vacancy undergoes a Jahn-Teller distortion upon relaxation, where two of the nearest atoms to the vacancy site form a weak covalent bond, resulting in a pentagon-like structure [16,17]. Formation of the pentagon saturates two  $sp^2$  dangling bonds, but the third unsaturated bond is left and is responsible for the formation of the magnetic moment. The local magnetic moment of single vacancy in graphene was found to be  $1.12 - 1.53\mu_B$  depending on the defect concentration [17]. The local density of states on the vacancy demonstrated two strongly spin polarized impurity states in the empty and filled states [16,17].

An example of an extended vacancy with a sublattice unbalance  $N_A = 6$  and  $N_B = 3$  is demonstrated in figure 3.5a. This vacancy results in a total spin  $S = 1.5$  and formation of ferrimagnetic order around the void [49]. The spin density of

each sublattice is schematically shown by circles in figure 3.5, where the diameter of a circle represents the expected value of the spin density according to calculations in reference [49]. The second extended vacancy shown in figure 3.5b does not have a sublattice imbalance because the same number of  $A$  and  $B$  atoms have been removed ( $N_A = N_B = 3$ ), and therefore it does not induce a local magnetic moment.

Lieb's theorem, however, does not specify the actual magnetic order or spin texture. Therefore, even if  $S = 0$  local magnetic moments can be formed resulting in antiferromagnetic or ferrimagnetic coupling between them [18]. The well understood example of compensated ferrimagnetic structure is a zigzag ribbon, where each edge presents ferromagnetic order antiparallel to each other for a total vanishing magnetic moment [53]. Other examples can be found as hexagonal graphene islands [50, 51] or their mirror images extended vacancies [18, 49]. In figure 3.5c, an extended defect causing a local moment even though  $N_A = N_B$  is shown. In this slit-shaped defect, 6 pairs of carbon atoms on sublattice  $A$  and  $B$  were removed. Local magnetic moments have developed on both sides of the slit [49]. Moments on the one side of the edge couple ferromagnetically because they are on the same sublattice, and moments on the opposite sides couple antiferromagnetically because they belong to the different sublattices [49]. There is no direct exchange coupling between the moments on both sides of the slit since the coupling is only through edges of the slit [49]. The formation of the local moment at the slit, however, showed to be dependent on the strength of the interaction and the length of the slit, which determines the localization of electrons. Local moments have been found for slits with length  $> 3$  atomic pairs and  $U = 1.2t$ , where  $t \approx 2.7$  eV is the nearest hopping energy for graphene [49].

Point defects in grain boundaries are not single vacancies as has been shown by STM in the previous chapter but rather more complicated defects. Two characteristic structures of grain boundaries on the graphite surface have been found. They are shown in figure 3.6. These structures are only illustrative since it is not known whether they form stable configurations or if they would undergo reconstruction in order to minimize the energy of the systems. Nevertheless, these structures will be used to demonstrate a basic principle why point defects in grain boundaries can induce local magnetic moments in graphite.

The first structure of a grain boundary is characterized by periodicity  $D$  and orientation  $\beta_D$  as it has been shown in previous chapter 2 in figure 2.4. The same structure of a grain boundary with periodicity  $D$  is shown again in figure 3.6a. It has a characteristic orientation which is slightly off the armchair edge direction by angle  $\beta_D$ . This results in the atomic structure along the axis of a grain boundary that consists of long armchair edges alternated by short zigzag edges. This sequence is repeated in space with periodicity  $D$ . In this structure, a sublattice unbalance

### 3. Ferromagnetism in graphite

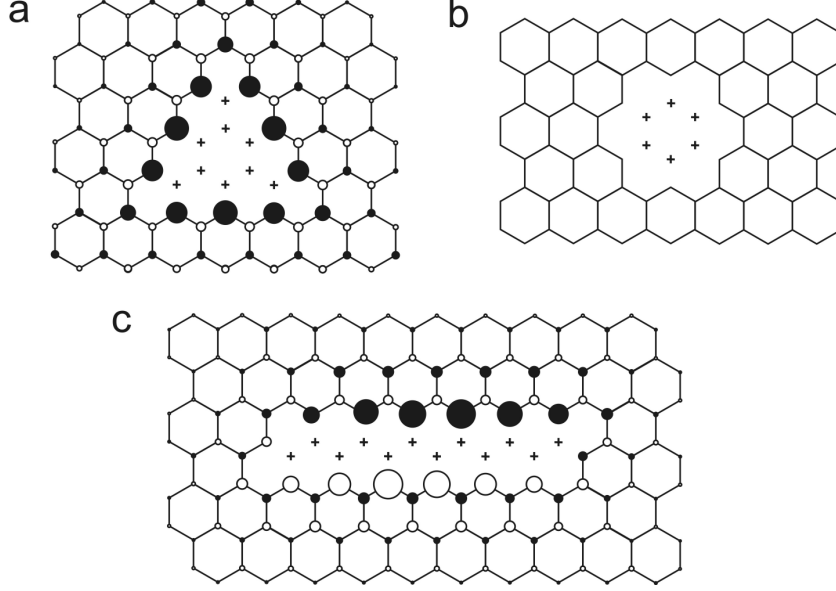


**Figure 3.5:** Examples of extended vacancies with a lattice imbalance (a)  $N_A = 6$ ,  $N_B = 3$ ; and with balanced lattices (b)  $N_A = N_B = 3$  and (c)  $N_A = N_B = 6$ . The extended vacancies (a) and (c) form local magnetic moments while the extended vacancy (b) does not induce a local magnetic moment. The closed dots represent schematically positive spin density and open dots negative density according to reference [49].

is created owing to existence of a zigzag segment within the armchair edge. The zigzag segment with the length of the graphite lattice parameter ( $2.46 \text{ \AA}$ ) produce a lattice unbalance  $|N_A - N_B| = 1$ , similarly like a single-atom vacancy. Therefore,  $N_A \neq N_B$  in the grain boundary structure in figure 3.6a and a local magnetic moment is created in accordance with Lieb's theorem. The assumed spin density of the grain boundary with periodicity  $D$  is shown in figure 3.6a. The second characteristic structure of a grain boundary has a  $\sqrt{3}D$  periodicity and is rotated by  $30^\circ$  with respect to the previous structure. Hence the internal structure of such a grain boundary is characterized by long zigzag edges and by short armchair edges as shown in figure 3.6b. The structure of such a grain boundary is symmetric, therefore  $N_A = N_B$ , even though long zigzag edges are present. However, a local magnetic moment can be formed in analogy to the extended vacancy shown in figure 3.5c.

If defects of the graphite lattice are exposed to atmospheric conditions most of the reactive vacancies will be saturated by other elements or molecules. The role of saturation of reactive carbon dangling bonds at vacancies has been considered in some of the DFT calculations of single-atom vacancies in graphene [16, 17, 52].

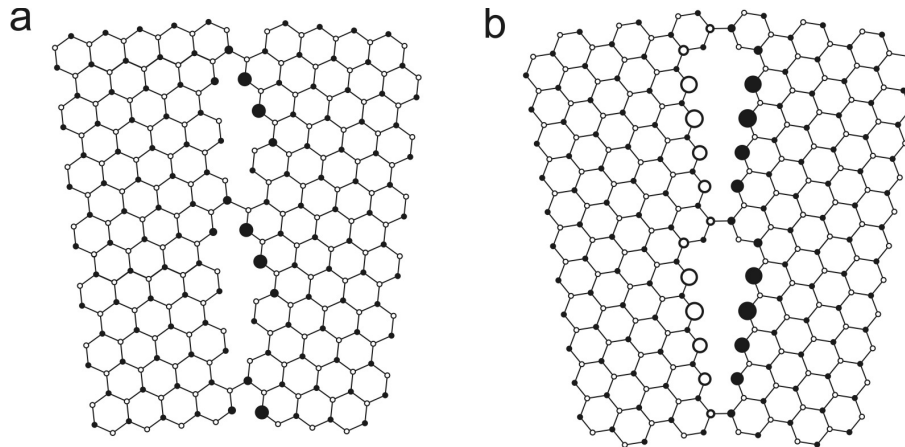


**Figure 3.6:** Schematic picture of magnetic defects in grain boundaries between two graphene flakes. (a)  $N_A \neq N_B$  and (b)  $N_A = N_B$ . The radius of each circle represents schematically the expected spin density.

Saturation of a vacancy by a hydrogen can lead to several scenarios as was found in DFT calculation of Lehtinen *et al.* [16]. In the first nonmagnetic situation, a hydrogen saturates the dangling bond at the distance  $1.25 \text{ \AA}$  above the graphene plane [16]. If a hydrogen is positioned directly in the vacancy, in the plane of graphene sheet, it give rise to the formation of a magnetic moment of  $2.3\mu_B$ . This configuration is, however, less stable than the previous one. The second magnetic situation is obtained upon chemisorption of two hydrogens in the vacancy, where a magnetic moment of  $1.2\mu_B$  is provided by the remaining dangling bond. Finally, three hydrogens bonded to the vacancy destroy the magnetic moment of the vacancy. A magnetic moment formation can also be achieved when a hydrogen is chemisorbed directly on a graphene sheet, which give rise to a magnetic moment  $1\mu_B$  [17]. Similarly, hydrogen pinned to a carbon interstitial in between two graphene planes showed to be magnetic [16, 17]. Saturation of vacancies by nitrogen has been studied by Zhang *et al.* [52]. While one nitrogen saturating a vacancy destroys the magnetic moment of the vacancy, similarly like one hydrogen, the presence of nitrogen nearby a vacancy has shown to produce larger macroscopic magnetic signals as compared to a standalone carbon vacancy [52]. In other calculations, vacancies remained magnetic upon adsorption of H and N atoms, whereas O quenched the magnetic moment on the vacancy [39]. Chemical functionalization and substitutional doping have also been investigated theoretically in graphene zigzag edges nanoribbons [15, 53–55]. Hydrogen saturation of zigzag edges is well known to preserve the spin polarization at the edge [15]. Similarly, oxidized zigzag graphene nanoribbons have been found to maintain a spin-polarized



### 3. Ferromagnetism in graphite

---

ground state with antiferromagnetic alignment at the ribbon edges [54]. Interestingly, edge-oxidized zigzag nanoribbons have been found to be more stable than hydrogen terminated nanoribbons [54]. There have also been studies of many other functional groups to be attached to the zigzag edges, leading to various results, for example see [55].

So far, it has been shown that local magnetic moments are likely to be formed at the point defects of grain boundaries even upon saturation by other atoms. The next question which arises is what the coupling between these moments will be? The types of magnetic couplings have been studied in single vacancies [19] and extended vacancies in graphene [18]. It has been found that coupling between vacancies on the same sublattice is always ferromagnetic while vacancies on opposite sublattices couple antiferromagnetically. From this point of view, the coupling between the neighboring defects in grain boundary is always ferromagnetic because the magnetic moments are formed on the same sublattice (see figure 3.6). This is valid for both structures of grain boundaries. The second structure in figure 3.6 will form a ferrimagnetic structure.

The role of different distances on the magnetic coupling between single-atom vacancies has been studied in the DFT study of an 3D array of single vacancies in graphite [20]. A ferrimagnetic coupling between vacancies has been found to be maintained up to the distance 1 nm [20]. Two spin-polarized localized states have been observed at the vacancy site. If the separation between vacancies was increased to 1.23 nm, ferrimagnetic order disappeared and only one localized peak at the Fermi energy was formed in the same way as for an isolated vacancy. In graphene, the same size of vacancy supercell exhibited still a net magnetic moment of  $1.72\mu_B$  [20]. In another theoretical study using a mean-field Hubbard model similar effects have been found [18]. Electronic structure and magnetic properties of vacancies and voids in graphene and graphene ribbons have been studied [18]. The magnetic properties of defective graphene showed to be related to the appearance of midgap states and how they were affected by electron-electron interactions. It has been found that if the defects were far away from each other, their electronic structure was the same as that of a single defect: midgap states localized in a single sublattice around the missing atom. Therefore, they behaved as independent objects with local spin given by Lieb's theorem  $2S = |N_A - N_B|$ . As the defects become closer, the midgap states hybridized, resulting in a bonding and antibonding pair away from zero energy. Defects in opposite sublattices coupled antiferromagnetically while defects on the same sublattice resulted in ferromagnetic coupling and the total magnetic moment was sum of individual local moments.

The electronic structure of grain boundaries shows strong similarities to these theoretical findings. Two split localized states around the Fermi energy have been

observed at different grain boundaries with periodicities  $< 4$  nm, while grain boundaries with periodicities  $> 4$  nm displayed only one peak at the Fermi energy. So grain boundaries with a large separation between defects behave as single isolated defects in graphite, while the electronic structure of closely spaced defects results in two split states. If they were spin polarized electron states the exchange splitting would be in order of 0.6 eV for most of the grain boundaries (see figure 2.10).

In figure 3.7, two grain boundaries with large 11 nm separation between their defects are shown. These models use the same slit-like models as were shown in figure 3.6. The slit defects are separated by regions where the unperturbed graphene lattice is present at the boundary. So, the effective distance between the defects is actually smaller than the superlattice periodicity. However, this is valid only for the  $\sqrt{3}D$  grain boundary structure (see figure 3.6b). The other structure of grain boundary with periodicity  $D$  have the separation between defects proportional to superlattice periodicity  $D$  because the local moments are expected to be formed at the zigzag edges fragments (see figure 3.6a). In order to maintain ferromagnetic coupling between defects even for 3.5 nm distance between defects in grain boundary indirect exchange interaction have to be involved. In graphene, the indirect Ruderman-Kittel-Kasuya-Yosida (RKKY) interaction [56] mediated via valence electrons between these local moments has been found to be always ferromagnetic due to the semimetallic properties of graphene [35]. The presence of ferromagnetism has been studied theoretically in the phase diagram of pure and doped graphene [38]. In graphite, however, because of finite density of states at the Fermi energy, competing ferro- and antiferromagnetic coupling is expected between the local moments. This gives an additional oscillating term with the oscillation period determined by the Fermi momentum of electrons (holes) [35,57].

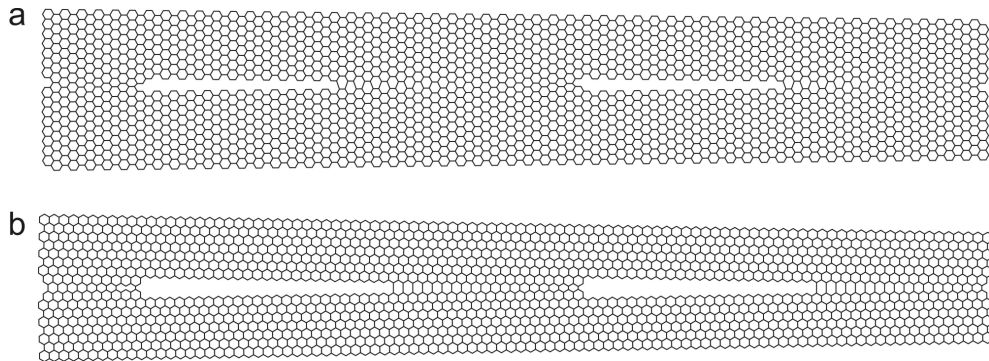


**Figure 3.7:** Examples of grain boundaries with 11 nm separation between their defects. (a)  $D = 11$  nm,  $\alpha = 1.28^\circ$  and (b)  $\sqrt{3}D = 11$  nm,  $\alpha = 2.2^\circ$ .

### 3. Ferromagnetism in graphite

---

Further supporting evidence that the ferromagnetism originates from grain boundaries is the fact that grain boundaries and step edges are the only defects, which are commonly observed in STM experiments on graphite surface. Naturally occurring point defects have been detected only seldom on the graphite surface with STM [58]. For this reason, point defects has been artificially produced by low-energy ions on the graphite surface for STM studies [59] and by high-energy protons in order to trigger ferro- or ferrimagnetic order in the irradiated spots on HOPG [4].

The very important aspect of grain boundaries is their two-dimensional character, which can explain most of the observed ferromagnetic signals in MFM and SQUID measurements. We assume that grain boundaries are propagating along the  $c$ -axis of the graphite crystal, creating 2D plane of defects as shown in figure 3.8. The distance between the defects in grain boundaries is determined by the superlattice periodicity in the graphene planes and by the graphite interlayer separation 0.335 nm along the  $c$ -axis of HOPG. As it was described before, step edges can be the manifestation of the grain boundaries buried underneath them as shown in figure 2.1. The ferromagnetic signal would then come from 2D grain boundary planes formed through the bulk crystal. MFM measurements showed defects to be magnetized along the  $c$ -axis of the graphite crystal meaning in-plane magnetized grain boundaries. An infinitely extended 2D magnetic plane with in-plane magnetization is stray-field-free and therefore it can exist in the single-domain state [60]. Accordingly, an in-plane magnetized grain boundary plane should show a single magnetic domain, which supports the observation of only one magnetization direction in MFM. Due to crossings among grain boundaries, minimum energy configuration would lead to magnetization pointing along the  $c$ -axis of HOPG. SQUID magnetization measurement showed one order higher saturation magnetization along the  $c$ -axis than along the in-plane direction, which is also in accordance with the 2D character of grain boundaries. It is expected that most of the grain boundaries do not lie exactly in the  $c$ -axis but have a small tilt. The angle of deviation of the grain's boundary from the perpendicular axis is given

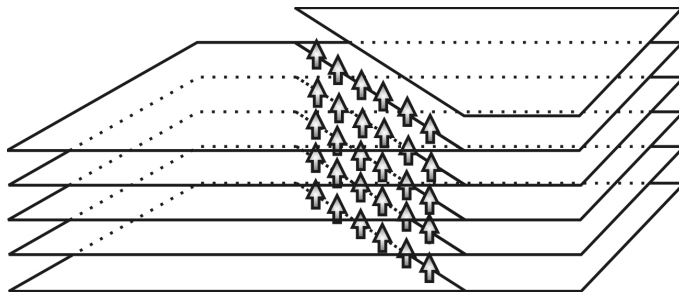


**Figure 3.8:** A schematic picture of a 2D magnetic grain boundary in bulk HOPG.

by the mosaic spread, which is  $3.5^\circ - 5^\circ$  for our HOPG samples. Therefore, a larger magnetic field is necessary to align the local magnetic moments of grain boundaries along the  $c$ -axis than along the graphene planes, where the magnetic axis stays in the 2D grain boundary plane. Hence magnetization in-plane shows easy magnetic axis and out-of-plane magnetization demonstrates a hard magnetic axis (figure 3.2).

In order to get an estimate of magnetic moment per one defect of a grain boundary, we can use concentration of magnetic defects on the graphite surface and assume that it is the same in the bulk graphite sample. The concentration of line defects observed by MFM (figure 3.1) was determined to be  $\approx 500$  ppm. The saturation magnetization along the  $c$  axis of the graphite reached value  $0.013 \text{ emu/g} \simeq 2.6 \times 10^{-5} \mu_B/\text{C}$ . By using distances between defects of grain boundaries  $0.5\text{-}4 \text{ nm}$ , we get magnetic moment  $0.2 - 1.5\mu_B$  per defect. This magnetic moment is close to the theoretically predicted value of magnetic moment  $1.12\text{-}1.53\mu_B$  of one vacancy site in graphene [17]. The magnetic moment in the model structure of a defect in a grain boundary with periodicity  $D$  should similarly result in a magnetic moment of one vacancy site (see figure 3.6). However, such an estimate cannot be done for the  $\sqrt{3}D$  grain boundary structure and a proper calculation has to be done for this purpose.

Ferromagnetic order in graphite demonstrates unexpectedly high Curie temperatures reaching values well above room temperature as reported in other studies [1, 3]. Kopelevich *et al.* [1] found ferromagnetic like hysteresis loops up to 800 K in magnetization measurements of HOPG. In the study of Esquinazi *et al.* [3], various graphite samples from different sources have produced ferromagnetic signals even at  $T_C = 500 \text{ K}$ . Higher temperatures could not be measured in their setup, which means that the transition temperature was above this temperature. Such a high  $T_C$  are observed only for ferromagnetic metals, for instance  $T_C(\text{Fe}) = 770^\circ\text{C}$ ,  $T_C(\text{Ni}) = 358^\circ\text{C}$ ,  $T_C(\text{Co}) = 1131^\circ\text{C}$ , magnetite  $T_C(\text{Fe}_3\text{O}_4) = 575 - 585^\circ\text{C}$  and hematite  $T_C(\text{Fe}_2\text{O}_3) = 675^\circ\text{C}$  [61]. Taking analogy to ferromagnetism in Fe allows us to get a rough estimate of Curie temperature of a magnetic grain boundary. Iron has  $T_C = 1043 \text{ K}$  and exchange splitting in order  $1.4 \text{ eV}$ . So, with the value of  $0.6 \text{ eV}$  the exchange splitting in a grain boundary, which has been determined from STS, we get  $T_C = 447 \text{ K}$ . However, the electrons involved in the ferromagnetic behavior in graphite are  $sp$  electrons and therefore the well known theory of magnetism based upon the unfilled character of  $3d$  or  $4f$  electrons energy levels cannot be directly applied [62]. This has been confirmed in the proton irradiated thin carbon films studied by x-ray magnetic circular dichroism, where the magnetic order was found to originate only from the carbon  $\pi$ -electron system [11]. Similarly, it has been found theoretically by Faccio *et al.* [20] that  $p_z$  orbitals contributed mainly to the ferrimagnetic spin arrangement for atoms far away from vacancies in the 3D array of single vacancies.

### 3. Ferromagnetism in graphite

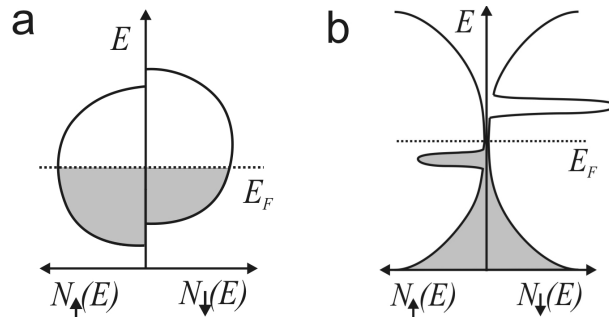


**Figure 3.9:** Spin polarized DOS showing weak itinerant ferromagnet (a) and ferromagnetic grain boundary with exchange split states (b).

Ferromagnetism with high Curie temperature  $T_C$  of  $sp$ -electrons in narrow impurity (defect) bands has been recently studied in theory [62]. This theory has been applied to  $\text{CaB}_6$  but it is well applicable to graphite with narrow defect states. Unfortunately, grain boundaries with two split states have a very small DOS at the Fermi level as shown in figure 3.9b, so the Stoner approach cannot be applied for them. The Stoner theory can be used only for isolated defects or zigzag edges which show a large DOS at the Fermi energy. The fact that localized states of grain boundaries with large separation between defects lie at the Fermi level and grain boundaries with smaller distances have finite DOS at the Fermi level suggests that itinerant (Stoner) magnetism can be induced by the electron exchange instability. It has been argued that Stoner ferromagnetism with high Curie temperatures  $T_C$  can be expected for  $sp$  electron systems with narrow impurity states [62]. Itinerant electron ferromagnetism in a narrow impurity band with  $sp$  electrons differs from the usual situation in the  $3d$  band of transition metals. In this theory, correlation effects do not reduce the effective interaction which enters the Stoner criterion in the same way as in bulk band ferromagnets. Moreover, the spin wave excitations may not be effective if full spin alignment is maintained in lowering  $T_C$ . The value of  $T_C$  can thus be close to the value given by Stoner theory, unlike for other bulk ferromagnetic metals.

The magnetic structure of grain boundaries can be viewed as 2D plane of local magnetic moments. The temperature behavior of this system can be described by the 2D anisotropic Heisenberg model [63]. Unlike 1D or 2D isotropic magnets which possess long-range order only in the ground state, real 1D and 2D magnets have shown finite values of the magnetic ordering temperature  $T_C$  due to weak interlayer coupling and/or magnetic anisotropy [63]. The 2D anisotropic Heisenberg model using self-consistent spin-wave theories (SSWT) with Dyson-Maleev, Schwinger and combined boson-pseudofermion representations has been recently developed for de-

scription of magnetism in layered magnetic materials [63]. This model due to correct fluctuation corrections to SSWT has successfully described behavior of several layered magnets such as  $\text{La}_2\text{CuO}_4$ ,  $\text{K}_2\text{NiF}_4$  and  $\text{CrBr}_3$  leading to an excellent agreement with experimental values of  $T_C$ . Accordingly, an adequate description of  $T_C$  is assumed by this model in the system of 2D planes consisting of local magnetic moments in graphite [64].

The anisotropic Heisenberg model is defined by [63]

$$H = -\frac{1}{2} \sum_{ij} J_{ij} \mathbf{S}_i \mathbf{S}_j - \frac{1}{2} \eta \sum_{ij} J_{ij} S_i^z S_j^z - D \sum_i (S_i^z)^2, \quad (3.3.2)$$

where  $J_{ij}$  are the exchange integrals,  $\eta > 0$  and  $D > 0$  are the two-site and single-site easy-axis anisotropy parameters. For our situation, the 2D magnet with the easy-axis anisotropy in the limit of small anisotropy  $D/|J| \ll 1$ ,  $\eta \ll 1$  will be assumed. The magnetic correlation parameters can be obtained within this model in the presence of spin wave fluctuations. The detailed description of the theoretical approach to SSWT of 2D anisotropic Heisenberg model has been done in reference [63]. For the ferromagnetic order, the analytical results for the Curie temperature was obtained

$$T_C = 4\pi JS^2 \left[ \ln \frac{T_C}{JS\Delta_0} + 4 \ln \frac{4\pi JS\Delta_0}{T_C} + C_F \right]^{-1}, \quad (3.3.3)$$

where constant  $C_F$  gives only small contribution and  $\Delta_0 = \Delta(T=0)$  is the dimensionless energy spin-wave gap. In the theoretical study of fluctuations of magnetic moments at the edge zigzag edge of graphene ribbons, a very high value for the spin wave stiffness  $D = 2100$  meV has been found [65]. If we use these results obtained for zigzag graphene edges in reference [65]:  $S = 1/2$ ,  $J = 4a = 4874$  K and  $\Delta_0 = 10^{-4}$ , the Curie temperature of 2D magnetic grain boundary would be  $T_C = 764$  K. This result is the low limit of  $T_C$ . The critical temperature would be only larger for larger values of  $\Delta_0$  or for the total spin of a defect within grain boundary. Hence grain boundaries in graphite are the most possible source of magnetism, feasible to reach Curie temperatures above room temperature.

### 3.4 Conclusions

In conclusion, ferromagnetic signals have been observed in HOPG locally by magnetic force microscopy and in the bulk magnetization measurements using a superconducting quantum interference device magnetometer at room temperature. Magnetic impurities have been excluded as the origin of the magnetic signal after careful analysis, supporting an intrinsic magnetic behavior of carbon-based materials. The observed ferromagnetism has been attributed to originate from unpaired *sp*-electron spins, localized at defects sites of grain boundaries. Scanning tunneling microscopy (STM)

### 3. Ferromagnetism in graphite

---

and spectroscopy (STS) have been performed on the same samples with a systematic study of different grain boundaries in the previous chapter 2. Grain boundaries have shown two intense localized states around the Fermi energy and enhanced charge density compared to bare graphite. The unique structure of defects within grain boundaries cause sublattice unbalance which is a sufficient condition for formation of local moments in graphene lattice. Coupling between these moments is always ferromagnetic because they are formed on the same sublattice. The 2D anisotropic Heisenberg model using self-consistent spin-wave theories has been applied in an attempt to provide rationale for the unexpectedly high Curie temperature of the ferromagnetic order observed in graphite, giving rise to  $T_C = 764$  K.

## Bibliography

- [1] Y. Kopelevich, P. Esquinazi, J. H. S. Torres, and S. Moehlecke, *J. Low. Temp. Phys.* **119**, 691 (2000).
- [2] J. Coey, M. Venkatesan, C. B. Fitzgerald, A. P. Douvalis, and I. S. Sanders, *Nature (London)* **420**, 156 (2002).
- [3] P. Esquinazi, A. Setzer, R. Höhne, C. Semmelhack, Y. Kopelevich, D. Spemann, T. Butz, B. Kohlstrunk and M. Lösche, *Phys. Rev. B* **66**, 024429 (2002).
- [4] P. Esquinazi, D. Spemann, R. Höhne, A. Setzer, K.-H. Han, and T. Butz, *Phys. Rev. Lett.* **91**, 227201 (2003).
- [5] K.-H. Han, D. Spemann, P. Esquinazi, R. Höhne, V. Riede, and T. Butz *Adv. Mater.* **15**, 1719 (2003).
- [6] A. W. Mombrú, H. Pardo, R. Faccio, O. F. de Lima, E. R. Leite, G. Zanelatto, A. J. C. Lanfredi, C. A. Cardoso, and F. M. Araújo-Moreira, *Phys. Rev. B* **71**, 100404 (2005).
- [7] P. Esquinazi, and R. Höhne, *J. Magn. Magn. Mater.* **290-291**, 20 (2005).
- [8] T. L. Makarova, B. Sundqvist, R. Höhne, P. Esquinazi, Y. Kopelevich, P. Scharff, V. A. Davydov, L. S. Kashevarova, and A. V. Rakhmanina, *Nature* **413**, 716-718 (2001); see however Retraction: *Nature* **440**, 707 (2006).
- [9] T. L. Makarova, *Semiconductors* **38**, 615 (2004).
- [10] A. V. Rode, E. G. Gamaly, A. G. Christy, J. G. Fitz Gerald, S. T. Hyde, R. G. Elliman, B. Luther-Davies, A. I. Veinger, J. Androulakis, and J. Giapintzakis, *Phys. Rev. B* **70**, 054407 (2004).

### 3.4 Bibliography

---

- [11] H. Ohldag, T. Tylizczak, R. Höhne, D. Spemann, P. Esquinazi, M. Ungureanu, and T. Butz, *Phys. Rev. Lett.* **98**, 187204 (2007).
- [12] S. Talapatra, P. G. Ganesan, T. Kim, R. Vajtai, M. Huang, M. Shima, G. Ramanath, D. Srivastava, S. C. Deevi, and P. M. Ajayan, *Phys. Rev. Lett.* **95**, 097201 (2005).
- [13] A. A. Ovchinnikov and V. N. Spector, *Synth. Met.* **27**, 615 (1988).
- [14] N. Park, M. Yoon, S. Berber, J. Ihm, E. Osawa, and D. Tománek, *Phys. Rev. Lett.* **91**, 237204 (2003).
- [15] M. Fujita, K. Wakabayashi, K. Nakada, and K. Kusakabe, *J. Phys. Soc. Jpn.* **65**, 1920 (1996).
- [16] P. O. Lehtinen, A. S. Foster, Y. Ma, A. V. Krasheninnikov, and R. M. Nieminen, *Phys. Rev. Lett.* **93**, 187202 (2004).
- [17] O. V. Yazyev and L. Helm, *Phys. Rev. B* **75**, 125408 (2007).
- [18] J. J. Palacios, J. Fernández-Rossier, and L. Brey, *Phys. Rev. B* **77**, 195428 (2008).
- [19] O. V. Yazyev, *Phys. Rev. Lett.* **101**, 037203 (2008).
- [20] R. Faccio, H. Pardo, P. A. Denis, R. Yoshikawa Oeiras, F. M. Araújo-Moreira, M. Veríssimo-Alves, and A. W. Mombrú, *Phys. Rev. B* **77**, 035416 (2008).
- [21] L. Pisani, B. Montanari, and N. M. Harrison, *New J. Phys.* **10**, 033002 (2008).
- [22] T. Kebe and A. Carl, *J. Appl. Phys.* **95**, 775 (2004).
- [23] <http://www.calipso.nl>
- [24] Y. Lu, M. Muñoz, C. S. Steplecaru, C. Hao, M. Bai, N. Garcia, K. Schindler, and P. Esquinazi, *Phys. Rev. Lett.* **97**, 076805 (2006).
- [25] D. Martínez-Martín and J. Gómez-Herrero, *Cond-Mat*, (unpublished) arXiv:0708.2994 (2007).
- [26] H. Wang, A. C. Papageorgopoulos, and N. Garcia, *Eur. Phys. J. B* **40**, 499 (2004).
- [27] D. Huertas-Hernando, F. Guinea, and A. Brataas, *Phys. Rev. B* **74**, 155426 (2006).



### 3. Ferromagnetism in graphite

---

- [28] R.-P. Methling, V. Senz, E.-D. Klinkenberg, Th. Diederich, J. Tiggesbäumker, G. Holzhüter, J. Bansmann, and K. H. Meiwes-Broer, *Eur. Phys. J. D* **16**, 173 (2001).
- [29] J. Barzola-Quiquia, R. Höhne, M. Rothermel, A. Sezer, P. Esquinazi, and V. Heera, *Eur. Phys. J. B* **61**, 127 (2008).
- [30] K. Nakada, M. Fujita, G. Dresselhaus, and M. S. Dresselhaus, *Phys. Rev. B* **54**, 17954 (1996).
- [31] K. Kusakabe and M. Maruyama, *Phys. Rev. B* **67**, 092406 (2003).
- [32] Y. Kobayashi, K. Fukui, T. Enoki, K. Kusakabe, and Y. Kaburagi, *Phys. Rev. B* **71**, 193406 (2005).
- [33] Y. Niimi, T. Matsui, H. Kambara, K. Tagami, M. Tsukada, and H. Fukuyama, *Phys. Rev. B* **73**, 085421 (2006).
- [34] Y. Kobayashi, K. Fukui, and T. Enoki, *Phys. Rev. B* **73**, 125415 (2006).
- [35] M. A. H. Vozmediano, M. P. Lopez-Sancho, T. Stauber, and F. Guinea, *Phys. Rev. B* **72**, 155121 (2005).
- [36] T. O. Wehling, A. V. Balatsky, M. I. Katsnelson, A. I. Lichtenstein, K. Scharnberg, and R. Wiesendanger, *Phys. Rev. B* **75**, 125425 (2007).
- [37] N. M. R. Peres, F. Guinea, and A. H. C. Neto, *Phys. Rev. B* **73**, 125411 (2006).
- [38] N. M. R. Peres, F. Guinea, and A. H. C. Neto, *Phys. Rev. B* **72**, 174406 (2005).
- [39] R. Y. Oeiras, F. M. Araújo-Moreira, N. Veríssimo-alves, R. Faccio, H. Pardo, and A. W. Mombrú, (unpublished) arXiv:0606533 (2006).
- [40] V. M. Pereira, F. Guinea, J. M. B. Lopes dos Santos, N. M. R. Peres, and A. H. Castro Neto, *Phys. Rev. Lett.* **96**, 036801 (2006).
- [41] V. M. Pereira, F. Guinea, J. M. B. Lopes dos Santos, N. M. R. Peres, and A. H. Castro Neto, *Phys. Rev. B* **77**, 115109 (2008).
- [42] H. Amara, S. Latil, V. Meunier, Ph. Lambin, and J.-C. Charlier, *Phys. Rev. B* **76**, 115423 (2007).
- [43] A. A. El-Barbary, R. H. Telling, C. P. Ewels, M. I. Heggie, and P. R. Briddon, *Phys. Rev. B* **68**, 144107 (2003).
- [44] Y. Ferro and A. Allouche, *Phys. Rev. B* **75**, 155438 (2007).

- [45] P. K. Wallace, *Phys. Rev.* **71**, 622 (1947).
- [46] M. Inui, S. A. Trugman, and E. Abrahams, *Phys. Rev. B* **49**, 3190 (1994).
- [47] A. Grüneis, C. Attaccalite, T. Pichler, V. Zabolotnyy, H. Shiozawa, S. L. Molodtsov, D. Inosov, A. Koitzsch, M. Knupfer, J. Schiessling, R. Follath, R. Weber, P. Rudolf, L. Wirtz, and A. Rubio, *Phys. Rev. Lett.* **100**, 037601 (2008).
- [48] E. H. Lieb, *Phys. Rev. Lett.* **62**, 1201 (1989).
- [49] H. Kumazaki and D. S. Hirashima, *Fyzika Nizkikh Temperatur*, **34**, 1025 (2008).
- [50] W. L. Wang, S. Meng, and E. Kaxiras, *Nano Letters* **8**, 241 (2008).
- [51] J. Fernandez-Rossier and J. J. Palacios, *Phys. Rev. Lett.* **99**, 177204 (2007).
- [52] Y. Zhang, S. Talapatra, S. Kar, R. Vajtai, S. K. Nayak, and P. M. Ajayan, *Phys. Rev. Lett.* **99**, 107201 (2007).
- [53] Y.-W. Son, M. L. Cohen, and S. G. Louie, *Nature (London)*, **444**, 347 (2006).
- [54] O. Hod, V. Barone, J. E. Peralta, and G. E. Scuseria, *Nano Letters* **7**, 2295 (2008).
- [55] F. Cervantes-Sodi, G. Csányi, S. Piscanec, and A. C. Ferrari, *Phys. Rev. B* **77**, 165427 (2008).
- [56] M. A. Ruderman and C. Kittel, *Phys. Rev.* **96**, 99 (1954); T. Kasuya, *Prog. Theor. Phys.* **16**, 45 (1956); K. Yosida, *Phys. Rev.* **106**, 893 (1957).
- [57] V. K. Dugaev, V. I. Litvinov, and J. Barnas, *Phys. Rev. B* **74**, 224438 (2006).
- [58] Y. Niimi, H. Kambara, T. Matsui, D. Yoshioka, and H. Fukuyama, *Phys. Rev. Lett.* **97**, 236804 (2006).
- [59] J. R. Hahn and H. Kang, *Phys. Rev. B* **60**, 6007 (1999).
- [60] R. Allenspach, *J. Magn. Magn. Mat.* **129**, 160 (1994).
- [61] J. Stöhr and H. C Siegmann, *Magnetism from fundamentals to nanoscale dynamics*, Springer, 2006.
- [62] D. M. Edwards and M. I. Katsnelson, *J. Phys.: Condens. Matter* **18**, 7209 (2006).
- [63] V. Yu. Irkhin, A. A. Katanin, and M. I. Katsnelson, *Phys. Rev. B* **60**, 1082 (1999).

### 3. Ferromagnetism in graphite

---

[64] Private communication with M. I. Katsnelson.

[65] O. V. Yazyev and M. I. Katsnelson, *Phys. Rev. Lett.* **100**, 047209 (2008).

## Chapter 4

# Graphene on silicon carbide

### 4.1 Introduction

Graphene is a flat monolayer of carbon atoms that are arranged in a two-dimensional (2D) honeycomb lattice. Since its experimental discovery in 2004 [1], it has attracted a lot of fundamental interest not only as the first true 2D material but mainly by showing unusual physical properties which have a great application potential in electronic devices [1–3]. This unique material combines low dimensionality with special electronic properties, where electrons are not described by Schrödinger equations but by relativistic Dirac equations. These properties are a direct consequence of its triangular crystallographic structure with two equivalent atoms ( $A$  and  $B$ ) in the unit cell. Graphene is a zero band gap semiconductor, characterized by a density of states that vanishes linearly close to the Fermi level. The energy spectrum is linear and consists of two Dirac cones centered at the opposite corners  $K$  and  $K'$  of the Brillouin zone. Due to the linear relation between energy and momentum, electrons in graphene mimic relativistic particles with zero rest mass and an energy-independent effective velocity  $\approx 10^6$  m/s. This differs from conventional metals and semiconductors where the energy spectrum can be approximated by a parabolic (free-electron-like) dispersion relation.

Graphene gives us thus a unique opportunity to study phenomena of quantum electrodynamics (QED) in a solid state material [4]. As a result, a number of new physical phenomena have emerged: the anomalous half-integer quantum Hall effect, which is observed even at room temperature [2], the minimal conductivity at the neutrality point [2], Klein tunneling [5], strong overcritical positron-like resonances in the Coulomb scattering cross section analogous to supercritical nuclei in QED [6], the Zitterbewegung in confined structures [7], anomalous Andreev reflections [8], and negative refraction in  $p$ - $n$  junctions [9]. However, from the technological point of

#### 4. Graphene on silicon carbide

---

view the most interesting properties are high mobility  $200,000 \text{ cm}^2/(\text{Vs})$  [10], the large phase coherence lengths of electrons [1, 3], the ability to tune carrier density by a gate voltage [1], the absence of backscattering [11], and spin and valley degrees of freedom which might be used in future spintronic devices [12]. Due to all this properties, graphene is considered as a potential candidate for replacing silicon in future electronic devices.

Graphene samples can be obtained by two preparation methods known by now. In the first "mechanical" method, the carbon flakes are peeled off from bulk graphite crystals and deposited onto a  $\text{SiO}_2/\text{Si}$  substrate [1]. By this way an almost freestanding graphene is produced and the carbon monolayer can be placed on any substrate of choice. The size of created graphene flakes, however, depends on the quality of the single crystalline graphite samples and despite many decades of graphite research, high quality single crystalline graphite samples are very difficult to obtain [13]. Moreover, one can hardly imagine that this method will be used for mass production of graphene in the future. The second preparation method uses epitaxial growth of graphite on a single-crystal substrates such as SiC, Ru, Ir, Ni and so on. From all these substrates silicon carbide is the most interesting for application purposes because it is a wide band gap semiconductor and the other substrates are metals. The growth of graphene on SiC is done by graphitization process at elevated temperatures. The ultrathin carbon layers are formed spontaneously by selective Si depletion of the SiC surface in ultra high vacuum [14] or argon atmosphere [15]. This method has apparent technological advantages over the exfoliation technique. It allows to precisely control the thickness of graphene grown on SiC to be either single or multiply layered depending on growth parameters [14]. The disadvantage is that the graphene layer is coupled to the substrate which might influence the electronic properties of graphene.

Electrons in single layer graphene on SiC are Dirac Fermions just as for the mechanically exfoliated graphene samples as was shown by transport as well as angle-resolved photoemission (ARPES) measurements [16, 17]. Most surprisingly, the electron spectrum of epitaxial graphene seems not to be strongly affected by the substrate, except that the Fermi energy is displaced due to electron transfer from the substrate. In particular, the Fermi level is located 0.45 eV above the Dirac point in the first graphene layer on the Si-terminated SiC surface [16]. There are two major differences between epitaxial graphene on SiC and exfoliated graphene samples: the quantum Hall effect has not been observed on epitaxial graphene yet and the mobility is an order of magnitude lower than in exfoliated graphene. The mobility of exfoliated graphene placed on  $\text{SiO}_2$  reaches  $25,000 \text{ cm}^2/(\text{Vs})$  at room temperature [2, 18], while it is only  $930 \text{ cm}^2/(\text{Vs})$  in epitaxial graphene on SiC(0001) [15]. The reason for this lays probably in the interaction with the substrate. Therefore, it is crucial for future

applications involving patterning of graphene on SiC to understand the electronic properties of graphene grown on the interface layer of the SiC(0001) surface. In general the complex structure of the interface of the SiC(0001) surface and the formation of the first graphene layer is still not fully understood and is under discussion in the literature. Scanning tunneling microscopy (STM) provides a very direct technique to probe the local electronic structure of this novel low-dimensional graphene system.

In this chapter, scanning tunneling microscopy and spectroscopy studies of few layered graphene on SiC(0001) are reported. The preparation method of graphene layers on SiC is described in the experimental section. Structural properties of graphene layers formed on the SiC surface are presented in section 4.3.1, where a special focus is dedicated to recognition of how many layers were formed on the SiC surface and on the structural differences between them. Electronic properties of graphene layers and the interface layer formed below them are characterized and discussed in section 4.3.2. Average and local electronic properties are studied by scanning tunneling spectroscopy and compared to other techniques probing the electronic structure of this system such as ARPES. In section 4.3.5, the electron scattering from defects is used to determine the graphene quasiparticle energy-momentum dispersion relation  $E(k)$  from the scattering wave oscillations produced around defects. Graphene phonons are studied by inelastic electron tunneling spectroscopy (IETS) in section 4.3.4. Gigantic asymmetric inelastic phonons signatures are observed on specific places of graphene monolayer in IETS. An inelastic electron tunneling model using nonequilibrium Green's function formalism (NEGF) is applied to explain these observations.

## 4.2 Experimental

The growth of atomically thin graphene samples was carried out in situ in ultra-high vacuum (UHV) on n-type 6H-SiC(0001) by thermal decomposition of Si at elevated temperatures. The growth process and characterization of the surface have been done according to the preparation method described by Berger et al. [14]. The n-doped SiC samples ( $1 - 2 \times 10^{18} \text{ cm}^{-3}$ ) have been obtained from Thomas Seyller, the University of Erlangen-Nürnberg, and have a specially treated SiC(0001) surface, showing micrometer large atomically flat regions in atomic force microscopy (AFM). A home-build e-beam heater has been used for the heating process, where the temperature has been monitored by a pyrometer using emissivity 0.9. The surface orientation has been examined with a low energy electron diffraction (LEED) after each heating step.

The heating procedure for obtaining few layer graphene on SiC consisted of several steps. First, SiC samples were degassed at 800°C for several hours in UHV. Afterwards they were heated to 1050°C to remove surface oxides. The  $(\sqrt{3} \times \sqrt{3})R30^\circ$  pattern

## 4. Graphene on silicon carbide

---

was observed in LEED, indicating a Si-terminated oxide free reconstruction [14]. An additional annealing step at 1100°C caused development of the  $(6\sqrt{3} \times 6\sqrt{3})R30^\circ$  pattern in LEED. A final heat treatment at 1250°C for 4 min resulted in a LEED pattern comparable to the results reported by Berger et al. [14], indicating one or more graphene layers formed on the sample surface. The annealing with the home-build e-beam heater, however, did not heat the sample uniformly, hence only  $30 \times 30 \text{ nm}^2$  atomically flat areas could be found with scanning tunneling microscopy.

Scanning tunneling experiments were performed in an Omicron GmbH LT-STM setup, working under UHV conditions ( $10^{-11}$  mbar) at 5 K. Electrochemically etched W tips were used in the constant current STM mode. Scanning tunneling spectroscopy (STS) and inelastic electron tunneling spectroscopy (IETS) have been obtained by using lock-in amplifiers [19]. Two lock-in amplifiers were connected to the STM to measure the first and second derivative of the tunneling current. For this purpose, an alternating voltage reference signal with a frequency 990 Hz and an amplitude 10 mV was superimposed to the bias voltage applied to the sample.

## 4.3 Results and discussions

### 4.3.1 Structural properties of few-layer graphene on SiC(0001)

Few layer graphene on 6H-SiC(0001) has been epitaxially grown by selective evaporation of silicon from the surface. In this graphitization process, graphene layers are formed spontaneously from the remaining carbon on the SiC surface at elevated temperatures. Figure 4.1 shows a LEED pattern of the SiC(0001) surface after the final heating procedure, which has been described in the experimental section. The LEED pattern demonstrates a complicated  $(6\sqrt{3} \times 6\sqrt{3})R30^\circ$  reconstruction with two coexisting hexagonal lattices. A schematic description of the LEED pattern is presented in figure 4.1b. The graphene lattice represented by the larger hexagon is seen together with a hexagonal pattern of the SiC lattice rotated by  $30^\circ$ . Their corresponding real space lattice constants are 3.08 Å for the SiC(0001) surface and 2.46 Å for graphene (graphite). The underlying SiC lattice is observed because LEED is sensitive up to a few atomic layers from the surface [20]. From the intensity of the SiC and graphene spots and by comparison with literature [14], it can be estimated that 1-3 graphene layers have been formed on the SiC surface. When more graphene layers were grown, the SiC spots fully disappeared from the LEED pattern and only graphitic spots were observed. This observation was also confirmed by other groups [14]. The six satellite spots around  $1 \times 1$  SiC and graphene spots together with the  $(6\sqrt{3} \times 6\sqrt{3})R30^\circ$  spots are due to a carbon rich interface layer. This interface layer serves most probably as the precursor layer for the formation of new graphene layers. More detailed discussion

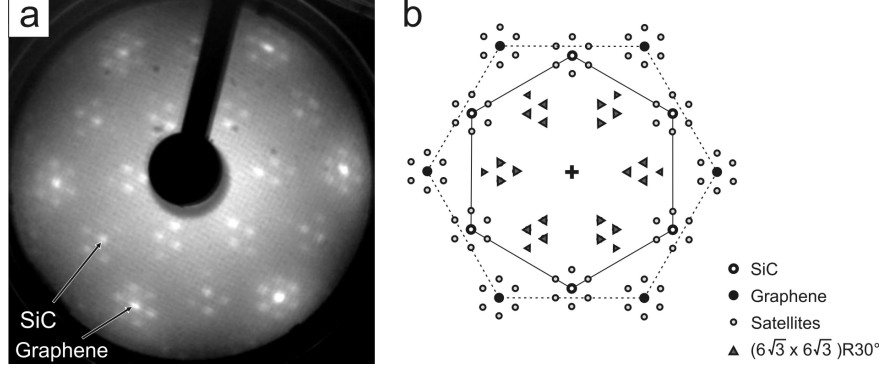


**Figure 4.1:** (a) A LEED pattern of 6H-SiC(0001) with a primary energy of 98 eV after annealing to 1250°C for 4 min. (b) An illustrative picture of the  $(6\sqrt{3} \times 6\sqrt{3})R30^\circ$  LEED pattern.

of a LEED characterization of the graphitization process on SiC surfaces can be found in [14, 21, 22].

In figure 4.2, STM topography pictures of large areas with atomic resolution on graphene monolayer and bilayer are shown. In order to compare them with LEED, the real space STM images have been transferred to reciprocal space via fast fourier transformation (FFT) as demonstrated in figures 4.2b and 4.2d. The FFT images display the same pattern as it has been observed by LEED (see figure 4.3), with only two differences that the SiC lattice spots are not visible and additional six spots in the center of the FFT image are present. The pattern in the center represents the  $6 \times 6$  structure of the SiC lattice. Its real space unit cell with 18 Å side length is pointed out by a dashed black diamond in the STM images in figures 4.2a and 4.2c. The six satellite spots around the graphite spots and in the center of FFT image have the same periodicities. However, the  $6 \times 6$  unit cell cannot explain the LEED and FFT patterns, therefore a larger  $(6\sqrt{3} \times 6\sqrt{3})R30^\circ$  unit cell with respect to the SiC lattice has to be constructed as has been discussed by Martensson *et al.* [21]. This structure is illustrated by the full diamond STM images in figure 4.2. The interpretation of the  $(6\sqrt{3} \times 6\sqrt{3})R30^\circ$  structure, however, remains controversial in literature [22]. The smallest mesh in the STM images is the graphene lattice with the lattice constant 2.46 Å. A set of three spots marked as  $(6\sqrt{3} \times 6\sqrt{3})R30^\circ$  in the FFT image represents the structure of the interface layer. Their corresponding real space periodicities are 0.64 nm and 0.52 nm.

Since the thermal desorption of silicon was not homogenous, different thickness of graphene was formed on the SiC surface. In figure 4.3, a transition between 1st, 2nd and 3rd graphene layers at two different bias voltages 650 mV (a) and 300 mV



#### 4. Graphene on silicon carbide

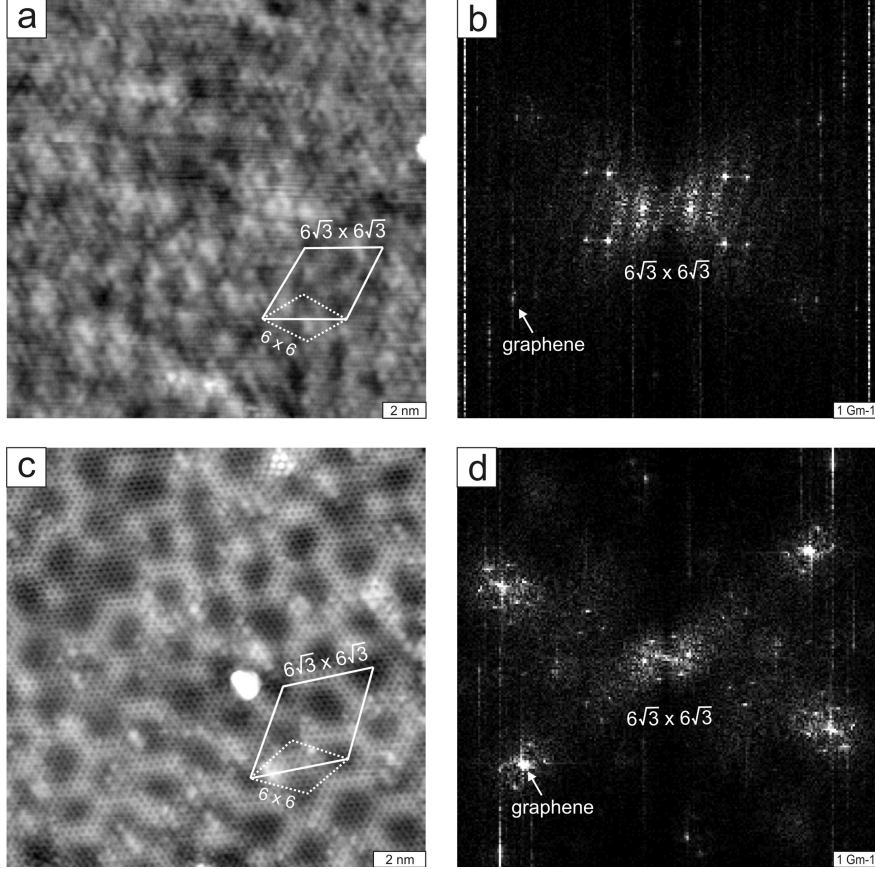


**Figure 4.2:** STM images of monolayer (a) and bilayer (c) graphene on SiC and their corresponding FFT images (b) and (d), respectively. The solid black diamond denotes the  $(6\sqrt{3} \times 6\sqrt{3})R30^\circ$  structure and dashed diamond represents the  $6 \times 6$  structure in respect to the SiC lattice. Scanning parameters: (a)  $20 \times 20 \text{ nm}^2$ ,  $V = 400 \text{ mV}$ ,  $I = 30 \text{ pA}$ ; and (c)  $17 \times 17 \text{ nm}^2$ ,  $V = 300 \text{ mV}$ ,  $I = 30 \text{ pA}$ .

(b) is illustrated. The first graphene layer has the surface corrugated by many small features, while the third graphene layer shows almost a smooth surface like graphite. The evaluation of the height corrugation on the individual graphene layers is depicted in figure 4.3c. It represents height histograms of  $40 \text{ nm}^2$  areas on 1st, 2nd and 3rd graphene layers measured at  $U = 650 \text{ mV}$ . The areas have been slope aligned and separated by average step heights. The height histograms on the individual graphene layers exhibit Gaussian distributions, which get narrower with increasing number of graphene layers. Their corresponding roughnesses measured at  $U = 650 \text{ mV}$  are  $12.2 \text{ pm}$ ,  $7.4 \text{ pm}$  and  $4.5 \text{ pm}$  on 1st, 2nd, and 3rd graphene layer, respectively. STM roughness has also been measured on the interface layer up to 3rd graphene layer on

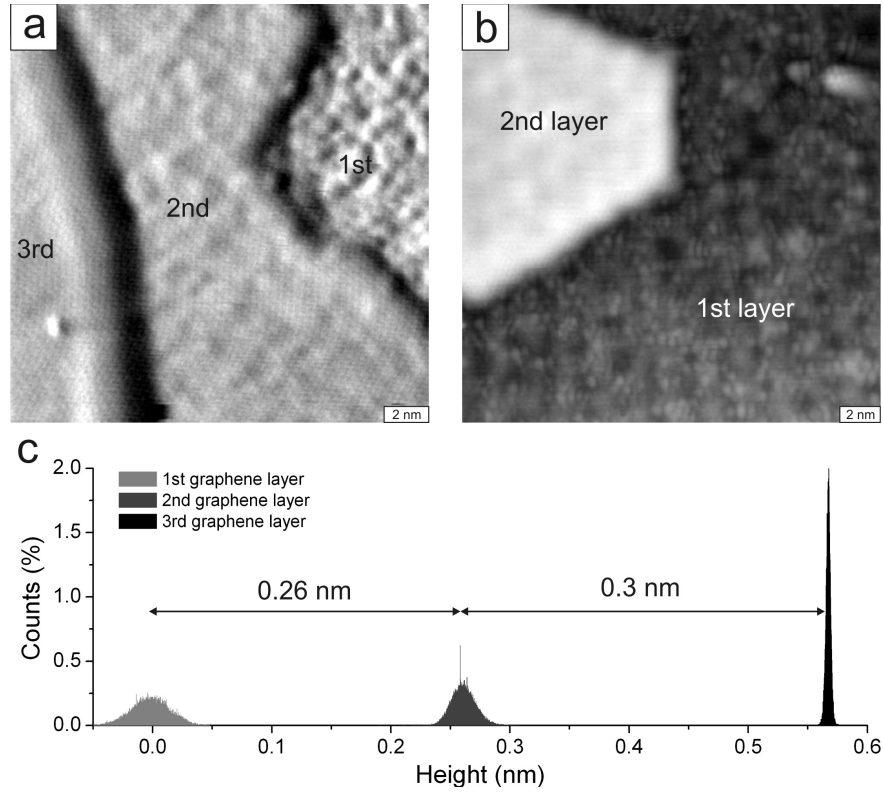


**Figure 4.3:** STM images demonstrating the growth of graphene layers on SiC(0001). (a) Current STM image of a "carpet" like transition between 1st, 2nd and 3rd graphene layers ( $20 \times 20 \text{ nm}^2$ ,  $V = 650 \text{ mV}$ ,  $I = 16 \text{ pA}$ ). (b) STM topography image of 1st and 2nd graphene layer on SiC with a step height 295 pm ( $22 \times 22 \text{ nm}^2$ ,  $V = 300 \text{ mV}$ ,  $I = 50 \text{ pA}$ ). (c) Height histogram of  $40 \text{ nm}^2$  areas on 1st, 2nd and 3rd graphene layers from image (a).

SiC by other group [23]. Lauffer *et al.* found very similar roughness on the individual graphene layers, which showed an exponential decay with additional graphene layers [23]. This result indicates that the roughness on the layers is caused by features belonging to the underlying interface layer and it is smoothed out by graphene overlays.

That graphene forms an overlay on the SiC surface can also be seen on the structure of step edges. A detail of a step edge of a few layers of graphene on SiC is shown in figure 4.4. The graphene atomic lattice is smoothly going over the step edge without a rupture in the crystalline structure. Such a continuous graphene layer is observed on all step edges. Graphene thus forms continues "carpet like" structure over the SiC surface. This fact has a very important consequence for possible applications,

#### 4. Graphene on silicon carbide

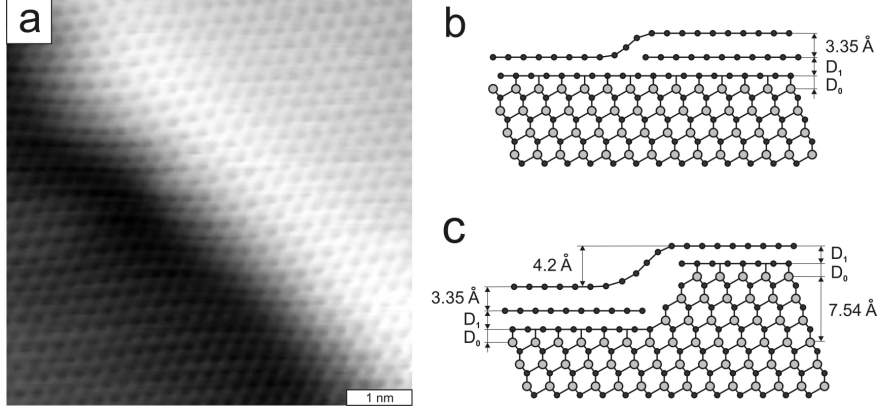


**Figure 4.4:** (a) STM image of a 390 pm step edge on a few layers of graphene on SiC(0001) ( $6.5 \times 6.5 \text{ nm}^2$ ,  $V = 500 \text{ mV}$ ,  $I = 60 \text{ pA}$ ). Atomic models of two possible step edges formed on few-layer graphene on SiC (b) and (c).

because a continuous graphene layer can be formed over whole SiC wafers.

Two different heights of step edges have been observed on the graphene layers on SiC. The first height was found around 300 pm (figure 4.3) and the other around 400 pm (figure 4.4). However, it is important to note that STM is not a proper tool for determining the real step height because it measures convolution of topography and local electronic structure. This can be seen for instance on the height of the step edges between the 1st and 2nd graphene layer in figure 4.3, where the height of the step was found 260 pm at  $U = 650 \text{ mV}$  and 295 pm at  $U = 300 \text{ mV}$ . Even though the height of the step edge shows dependence on the bias voltage, it does not change the fact that there are two different heights of step edges on few-layer graphene on SiC because they have been observed on the same STM images with identical tunneling parameters.

In figures 4.4b and 4.4c, possible atomic structures of two step edges are constructed. In the first one, the step edge is formed by additional graphene layer resulting in graphite like step edge with the step height 3.35 Å. This model is in accordance with a result of resonant tunneling spectroscopy [24], where the height difference between 1st and 2nd graphene layer on SiC has been measured 3.35 Å. The other observed step edge evinces a larger step height 4.2 Å as shown in figure 4.4c. The formation of this step edge was proposed by Lauffer *et al.* [23] and it reflects the fact that approximately three layers of SiC are needed to produce enough carbon to form one graphene layer.  $D_1$  denotes the separations between the 1st graphene layer and the 0 interface layer, and  $D_0$  between the 0 interface layer and SiC surface. These distances are not known experimentally. The reason is that the structure of

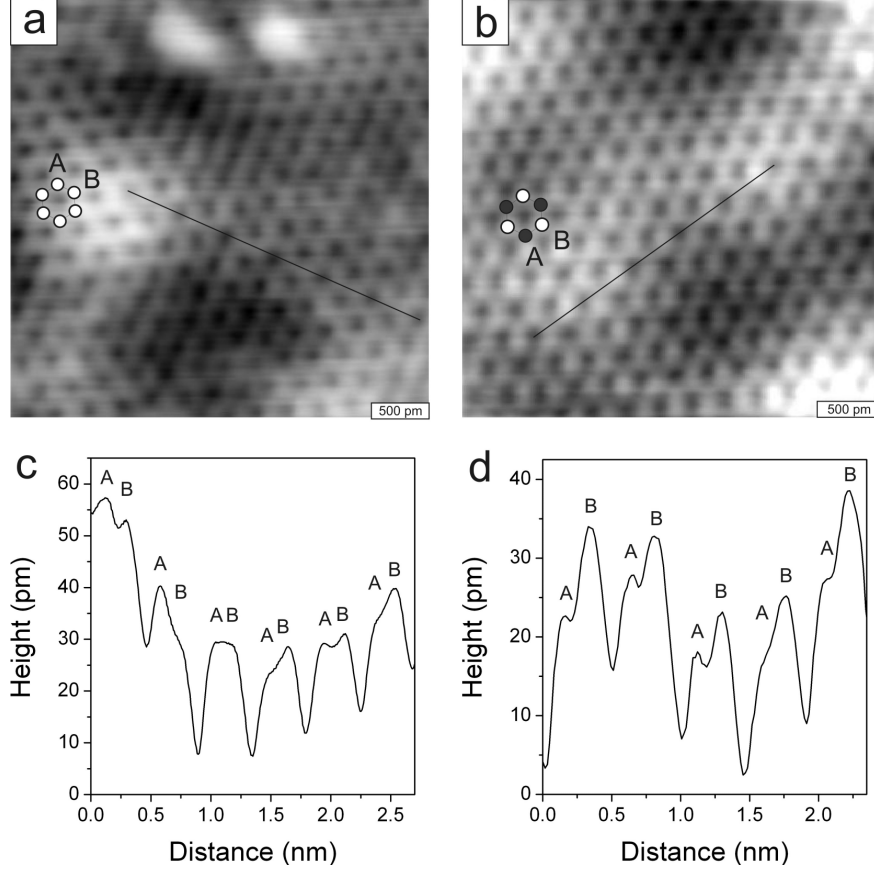


**Figure 4.5:** Atomically resolved STM images of the 1st graphene layer (a) and the 2nd graphene layer (b) on SiC and their corresponding cross sections along the black lines (c) and (d), respectively. Scanning parameters:  $3.5 \times 3.5 \text{ nm}^2$ ,  $V = 150 \text{ mV}$ ,  $I = 30 \text{ pA}$ .

the carbon rich interface layer is not clear so far. However, it is expected that the distance  $D_1$  is close to the layer separation in graphite sustaining weak van der Waals interaction, because the Dirac quasiparticles are preserved in the system showing linear dispersion in ARPES [16,17]. From the observation of two different step edges, it can be concluded that the growth mechanism of graphene on SiC is more complicated than a simple collapse of the three SiC layer as seen from the model in figure 4.4c. A redistribution of carbon atoms at the SiC surface must occur in the interface layer in order to be able to support formation of the step edge shown in figure 4.4b.

In figure 4.5, STM images of atomically resolved 1st and 2nd graphene layers are shown. All the carbon sites of the honeycomb graphene lattice are visible on monolayer graphene in STM. However, three carbon sites out of six are more pronounced

#### 4. Graphene on silicon carbide

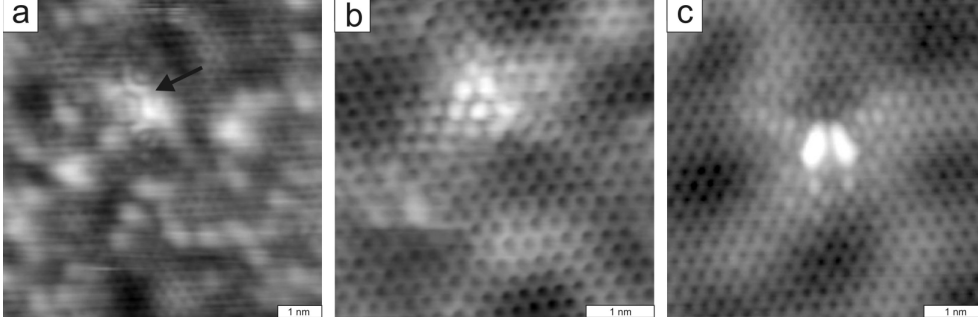


**Figure 4.6:** STM images of structural defects on monolayer (a) and bilayer graphene (b) and (c). Scanning parameters: (a)  $7.5 \times 7.5 \text{ nm}^2$ ,  $V = 420 \text{ mV}$ ,  $I = 30 \text{ pA}$ ; (b)  $4.5 \times 4.5 \text{ nm}^2$ ,  $V = 650 \text{ mV}$ ,  $I = 16 \text{ pA}$ ; and (c)  $5 \times 5 \text{ nm}^2$ ,  $V = 300 \text{ mV}$ ,  $I = 45 \text{ pA}$ .

on bilayer graphene, giving a clear sign of broken symmetry between the A and B sublattices. The AB asymmetry is better depicted in the cross section shown in figure 4.5d. In order to eliminate the slope caused by  $(6\sqrt{3} \times 6\sqrt{3})R30^\circ$  reconstruction a statistical difference between A and B carbon sites have been done. Averaged differences of STM heights between A and B sites are  $h_{B-A} = 0.15 \pm 0.5 \text{ pm}$  on the 1st graphene layer and  $h_{B-A} = 8.5 \pm 3.5 \text{ pm}$  on the 2nd graphene layer. This result shows a clear asymmetry between A and B carbon sites on the second layer, while graphene monolayer exhibits equivalent carbon sites independently on the bias voltage from 0.5 V to -0.5 V. In graphite, the AB asymmetry is due to a stacking order of graphene layers. The Bernal stacking (ABAB) in graphite produces two inequivalent carbon sites in the unit cell. The A sublattice has an atom in the layer below, whereas the B sublattice does not have an atom directly below. This causes that the  $\pi$  band of the A carbons is lowered by 0.7 eV from the  $\pi$  band of the B carbons, which is crossing the Fermi energy [25]. This results in that only the B carbon sites are observed in STM. Similarly, it shows that the stacking order in bilayer graphene in figure 4.5b is Bernal like (AB).

The major difference between monolayer and bilayer graphene in STM is in the appearance of bright protuberances at bias voltages higher than  $\pm 100 \text{ mV}$ . This has been already demonstrated by different roughnesses of these two layers. Bright features are clearly visible on single-layer graphene and only weakly on bilayer graphene. It has been concluded that the protuberances are caused by the interface layer and graphene layers cover them. Two of these protuberances can be seen in the upper part of figure 4.5a. They do not act as the structural defects in graphene lattice because they do not produce the typical  $(\sqrt{3} \times \sqrt{3})R30^\circ$  superstructure around them. The  $(\sqrt{3} \times \sqrt{3})R30^\circ$  superstructure has always been observed around structural de-

fects in graphene [26, 27] and graphite [28–30]. In figure 4.6, one structural defect in monolayer and two different point defects in bilayer graphene are shown. The  $(\sqrt{3} \times \sqrt{3})R30^\circ$  superstructure can be observed in the vicinity of the defects decaying from the defects. From the symmetry of the superstructure the internal structure can be extracted. The charge modulation around the defects of graphene reflects the symmetry of the defects [31]. In a theoretical study of atomic impurities (defects) in graphene [31] it has been demonstrated that single and double atomic defects result in different shapes of charge modulation. A single atomic defect resulted in a simple trigonal symmetry in the charge modulation around the defect, while a double atomic defect demonstrated two fold symmetry [31]. Accordingly, the defect in figure 4.6b could be a single vacancy and the defect in figure 4.6d could be due to a double vacancy. Interestingly, the defect in the monolayer graphene shows a sixfold symmetry with a ring in the center. Similar, defects with an almost perfect six-fold symmetry have also been observed in bilayer graphene on SiC [26, 27]. However, the six-fold symmetry appeared only in the vicinity of the defect, while three-fold symmetry was observed farther away from the impurity [27]. This showed that for bilayer graphene, the two sublattices do not contribute equally to the local density of states [27].

In summary, graphene monolayers and bilayers on SiC can be distinguished in STM due to different appearances of protuberances on their surfaces, which are caused in the interface layer underneath. Hence monolayer graphene demonstrates higher roughness than bilayer graphene. This difference is mainly apparent in the bias voltage range 100–400 mV. Monolayer graphene shows all the six carbon atoms equally strong in STM, whereas bilayer graphene demonstrates an asymmetry between the A and B sublattices, similar to graphite, due to a stacking order. Finally, the monolayer and bilayer graphene are separated by step edges of two possible heights 300 pm and 400 pm.

### 4.3.2 Electronic structure of epitaxial graphene

In this section, electronic structures of the interface layer and graphene layers on SiC(0001), probed by scanning tunneling microscopy and spectroscopy are discussed. STS curves measured on the 0 interface layer, 1st, and 2nd graphene layers are displayed in figure 4.7. The  $dI/dV$  curves represent spatial averages over 256 points obtained on  $15 \times 15 \text{ nm}^2$  STM areas. A band gap  $\approx 200 \text{ mV}$  is observed on the 0 interface layer with a localized electron state at  $-200 \text{ mV}$ . This result differs from STS measurements on the interface layer on SiC(0001) reported by Rutter *et al.* [32], where a larger 400 mV band gap and no localized states have been observed. The reason for this difference lies most probably in a disordered structure of the interface layer as will be discussed later in the text.

#### 4. Graphene on silicon carbide

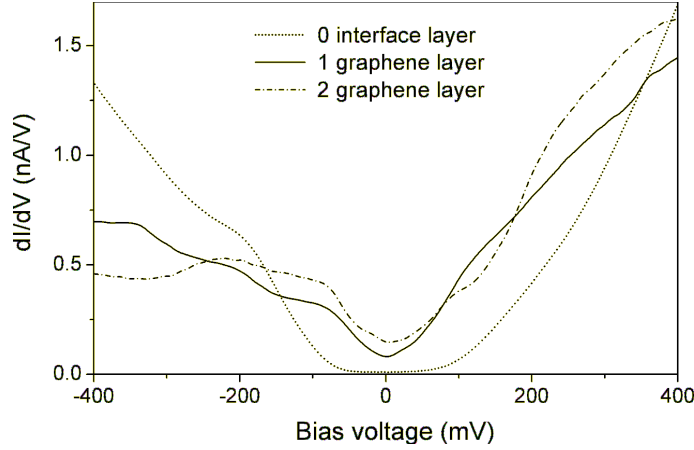


**Figure 4.7:** Spatially averaged STS curves on the 0 interface, 1st and 2nd graphene layers on SiC. Scanning parameters:  $V = 300$  mV,  $I = 50$  pA for graphene monolayer and bilayer and  $V = -200$  mV,  $I = 5$  pA for the 0 layer.

The first graphene and the second graphene layers show metallic behavior in STS measurements. Both systems have finite densities of states in the gap region of the interface layer. Their  $dI/dV$  curves evince an asymmetric DOS around the Fermi energy with larger densities in the empty states compared to the filled states. Surprisingly, a "gap-like" feature is observed at the Fermi energy evinced by a reduction of the  $dI/dV$  below  $\pm 80$  mV. The gap-like feature is not expected to appear in the DOS of either monolayer and bilayer graphene. It is known from photoemission experiments that graphene layers on SiC are electron doped, which results in a shift of the Dirac point towards negative values. The Dirac point is shifted to 0.45 eV in monolayer graphene and 0.31 eV in bilayer [33]. In STM and STS study [23], minima at -0.31, -0.19, and -0.13 V have been observed on  $dI/dV$  curves measured on 2, 3 and 4 graphene layer, respectively. These minima fitted well to the position of the Dirac points, which have been determined by ARPES [34]. A reduction of the DOS around -0.3 V in bilayer graphene is also observed in our data. In the single layer, however, no such a dip has been found around the Dirac point around the energy 0.45 eV. In order to understand the peculiar DOS of graphene layers and the interface layer, STS measurements have been analyzed on a local scale in the following sections.

##### First graphene layer

In figure 4.8, sets of scanning tunneling topography pictures on monolayer graphene are shown as a function of bias voltage. Two STM pictures taken with positive and negative bias voltages are shown above each other in order to visualize the difference

between filled (negative voltages) and empty (positive voltages) states. The influence of bias voltage was studied in the range from  $\pm 50$  mV to  $\pm 700$  mV. For this purpose, the STM images have been measured on the same  $10 \times 10$  nm<sup>2</sup> area at 5 K. Such a low temperature ensures that the thermal drift of the STM piezo-elements is negligible. At low bias voltages ( $\pm 50$  mV), the characteristic graphene atomic structure is visible indicating a single graphene layer. When the bias voltage is increased, bright dots start to appear till they fully dominate STM pictures at higher voltages. The structure of these bright dots remains practically constant in the range from  $\pm 300$  to  $\pm 700$  mV. Similar STM topography pictures have been discussed by Rutter et al. [32].

The positions of bright features are not the same in the filled and the empty states as symbolized by crosses and circles in figure 4.9. Circles point out the positions of the bright features in the filled states (-300 mV) and crosses in the empty states (300 mV). Even though the positions of the bright dots in negative and positive voltages are not exactly the same, they overlap each other on certain positions because of their  $\approx 0.5$  nm spatial extension. The origin of these features is still not fully understood, nevertheless, it is known from literature that they belong to the interface layer residing below the first graphene layer [23, 32, 35]. Thus graphene monolayer shows a transparency at bias voltages above  $\pm 100$  mV in STM.

Scanning tunneling spectroscopy has been measured locally on the bright features and in between on monolayer graphene in figure 4.10. Three characteristic  $dI/dV$  spectra have been found. All STS curves measured at different positions of the first layer graphene can be explained as a combination of these three curves. The three characteristic STS curves have been obtained with  $V = 300$  mV,  $I = 41$  pA and averaged over 10  $dI/dV$  curves. The first STS spectrum represents regions with a graphene character, where no bright features are observed in STM. It has the smallest electron density from all the curves and it does not possess any localized states. The second curve represents bright features, visible in negative bias voltage, marked by circles in figure 4.9. Two localized states are observed on this curve at -200 mV and -500 mV. The third  $dI/dV$  curve designates bright features visible in positive bias voltage that are marked by crosses in figure 4.9. This curve has the most asymmetric shape with a steep rise in the empty states due to a localized state at 500 mV. All STS curves on monolayer graphene on SiC(0001) show a minimum at the Fermi energy and an asymmetric shape, where the empty states are more pronounced than the filled states. The spatial extension of the localized states is approximately to 0.5 nm distance from the centers of bright features similarly as it is seen in STM topography. The localized states are originating from the interface layer as will become apparent in the following section.



#### 4. Graphene on silicon carbide

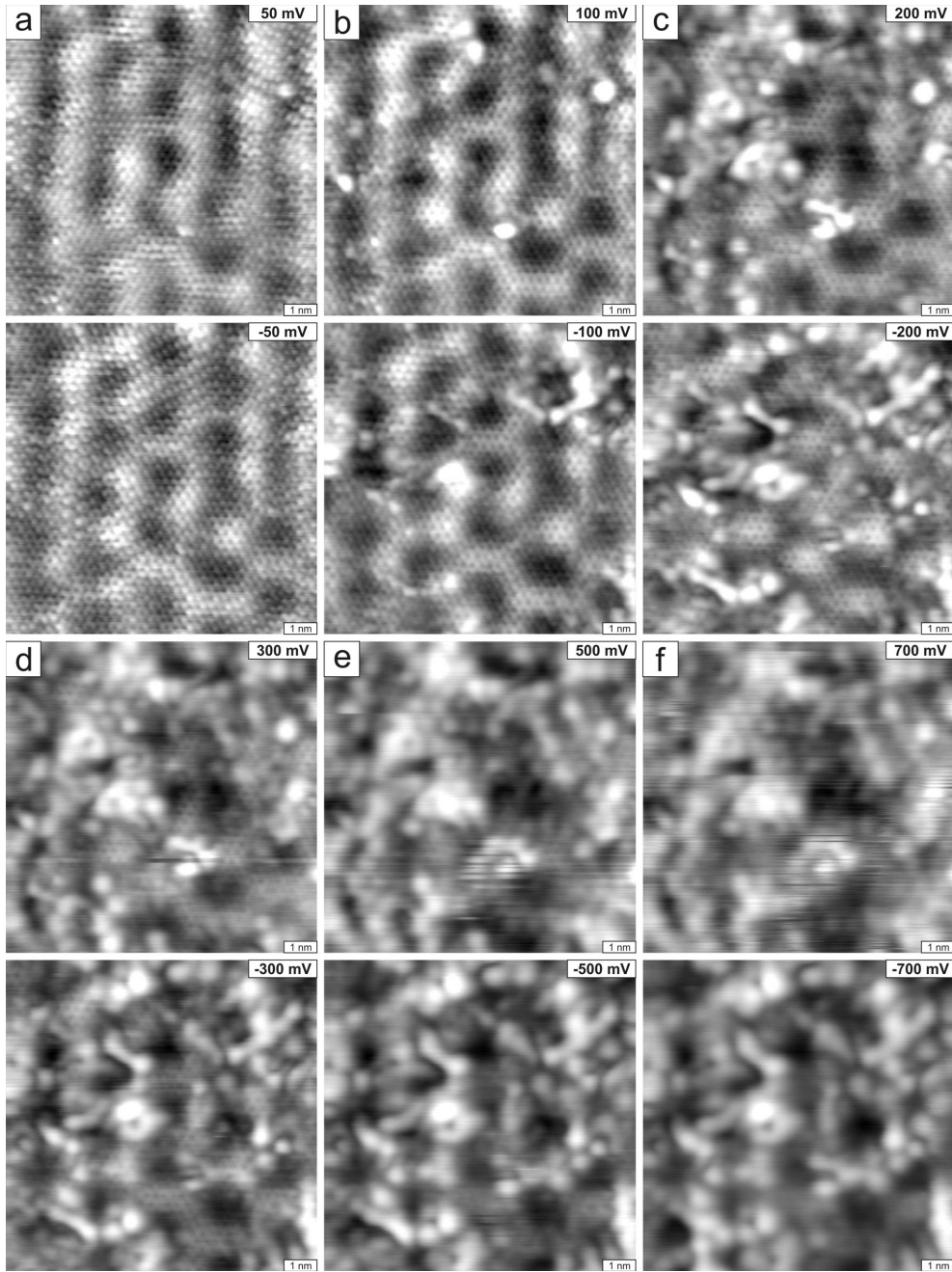


**Figure 4.8:** Sets of STM images on a graphene monolayer measured on the same  $10 \times 10 \text{ nm}^2$  area as a function of bias voltage. Scanning parameters:  $I_t = 5 \text{ pA}$ ,  $V =$  (a)  $\pm 50 \text{ mV}$ , (b)  $\pm 100 \text{ mV}$ , (c)  $\pm 200 \text{ mV}$ , (d)  $\pm 300 \text{ mV}$ , (e)  $\pm 500 \text{ mV}$  and (f)  $\pm 700 \text{ mV}$ .

### 4.3.3 Electronic structure of the interface layer

STM images of a 0 interface layer are presented in figure 4.11. The interface layer has differed from the 1st graphene layer by that STM did not show the graphene lattice on its surface and tunneling below  $\pm 200$  mV was not possible. The latter has already been demonstrated in the averaged  $dI/dV$  spectrum taken on the interface layer in figure 4.7, where a 200 mV band gap has been observed. The surface of the interface layer consists of bright protuberances with a radius around 0.5 nm similarly like on the first graphene layer. In order to visualize the difference between filled and empty states of the interface layer, the STM images in figure 4.11 have been measured with negative and positive bias voltages on the same area. The positions of the bright features were again marked out by crosses and circles denoting empty and filled states, respectively. Two additional additional bright features appeared at higher voltages ( $>400$  mV) compared to the first graphene layer. These features have been marked as  $c$  in empty states and  $d$  in filled states. The structure of bright features is disordered on the local scale but show an order on the large scale maintaining the  $(6\sqrt{3} \times 6\sqrt{3})R30^\circ$  unit cell as has been confirmed by LEED and large scale STM images (see figures 4.1 and 4.2).

A local analysis of scanning tunneling spectroscopy on the interface layer is presented in figure 4.12. Five characteristic  $dI/dV$  spectra representing different locations on the surface have been identified. Each STS spectrum has been measured with  $V = -200$  mV,  $I = 5$  pA and averaged over 10  $dI/dV$  measurements. The first two STS curves represent bright features in negative bias voltage and have been marked

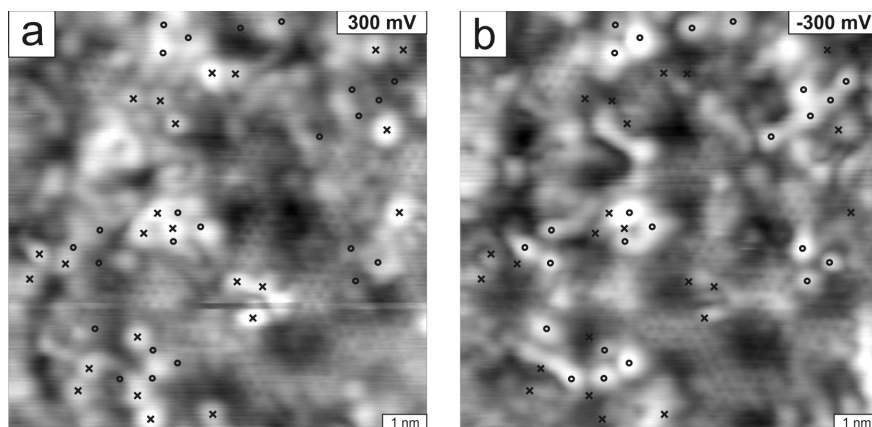


**Figure 4.9:** STM images of a  $10 \times 10$  nm<sup>2</sup> area on single-layer graphene on SiC taken with  $I_t = 5$  pA and  $V = 300$  mV (a) and  $V = -300$  mV (b). Circles point out the positions of the bright dots in the filled states and crosses in the empty states.

#### 4. Graphene on silicon carbide

---

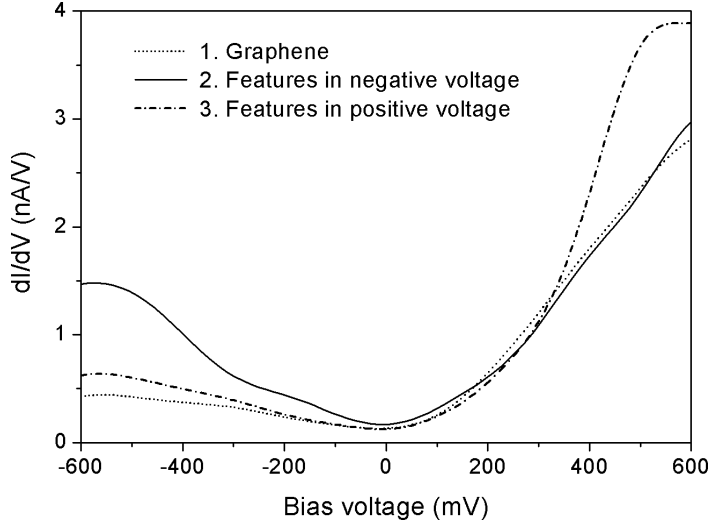


**Figure 4.10:** Three characteristic  $dI/dV$  spectra on monolayer graphene on SiC(0001). They have been averaged over 10 curves taken at  $V = 300$  mV,  $I = 41$  pA.

by circles and  $d$  in figure 4.11. They possess localized states at  $-200$  mV (circles) and  $-500$  mV ( $d$ ), where the latter peak is present only from its half. Third and fourth STS curves depict electronic structure of bright features visible in positive bias voltage, which were marked by crosses and  $c$  in figure 4.11. They exhibit localized electron states at  $200$  mV (crosses) and  $500$  mV ( $c$ ), where the latter is seen as a sharp increase above  $300$  mV. The local electronic structure of regions in between the bright features is characterized by the fifth STS curve in figure 4.12 showing the smallest electron density and no localized states.

The real band gap of the interface layer is formed in between two localized states at  $-200$  mV and  $200$  mV as it can be seen from the individual STS curves. When local STS measurements were spatially averaged (see figure 4.7), a smaller  $100$  mV gap was observed due to an expansion of electron states into the  $400$  mV gap. Such a behavior is characteristic for a disordered semiconductor, where electron states extend into the  $400$  mV gap due to a disorder in the interface layer. This shows consistency with the averaged STS data on the interface layer surface published by Rutter *et al.* [32], where  $400$  mV gap was reported. Therefore, the interface layers could have been in a different stages of Si depletions in our study and in reference [32], giving rise to different band gaps in the averaged STS spectra.

Since bright protuberances observed on the 0 and 1 layers show the same structure and electronic properties, they have the same origin. They are formed in the inter-

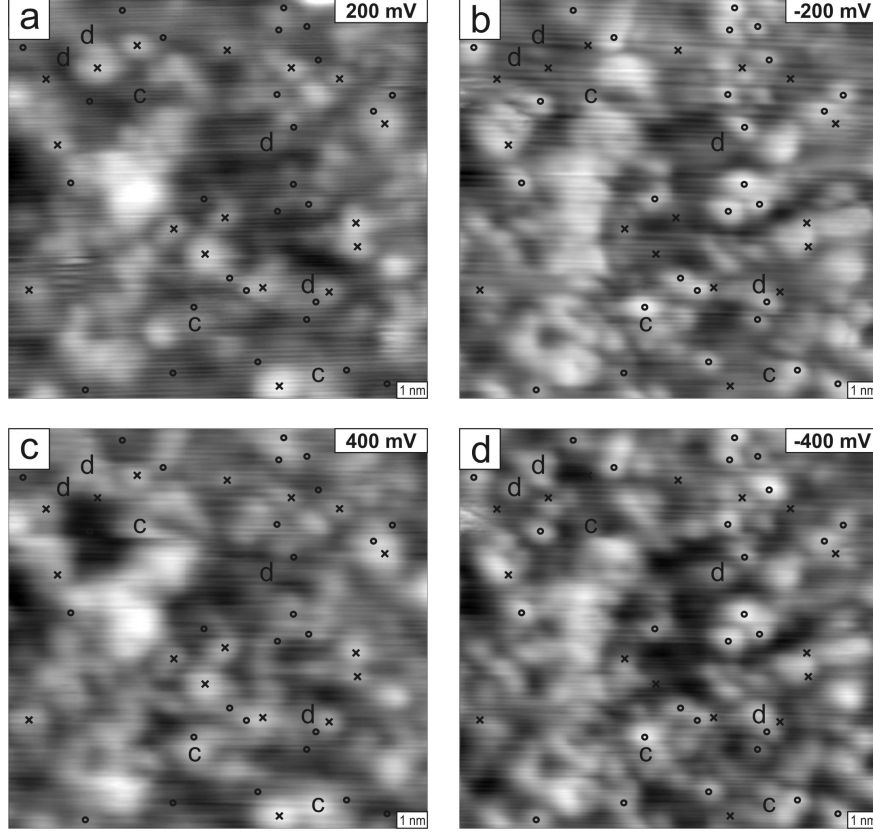


**Figure 4.11:** STM images of the same  $10 \times 10 \text{ nm}^2$  area on the 0 interface layer on SiC(0001) taken with  $I_t = 5 \text{ pA}$  and  $V = 300 \text{ mV}$  (a) and  $V = -300 \text{ mV}$  (b). Circles point out the positions of the bright dots in the filled states and crosses in the empty states.

face layer and due to a low electron density of graphene layers above and the large densities of the localized states, they protrude through the graphene layers, where they are detected by STM at higher bias voltages. An angle resolved photoelectron spectroscopy (ARPES) study [33] on the interface layer and the first graphene layer showed consistency to these findings. While the first graphene layer displayed well developed graphene  $\pi$  bands extending up to the Fermi level, the interface layer exhibited semiconducting properties with absent  $\pi$  bands [33]. The carbon rich interface layer with  $(6\sqrt{3} \times 6\sqrt{3})R30^\circ$  reconstruction on the SiC(0001) showed two localized states at the binding energies 0.5 and 1.6 eV [33]. The former localized state is identical to the localized state observed in STS at -0.5 mV (figure 4.10), characterizing the filled states. The other localized state observed in STS at -0.2 mV has not been

#### 4. Graphene on silicon carbide

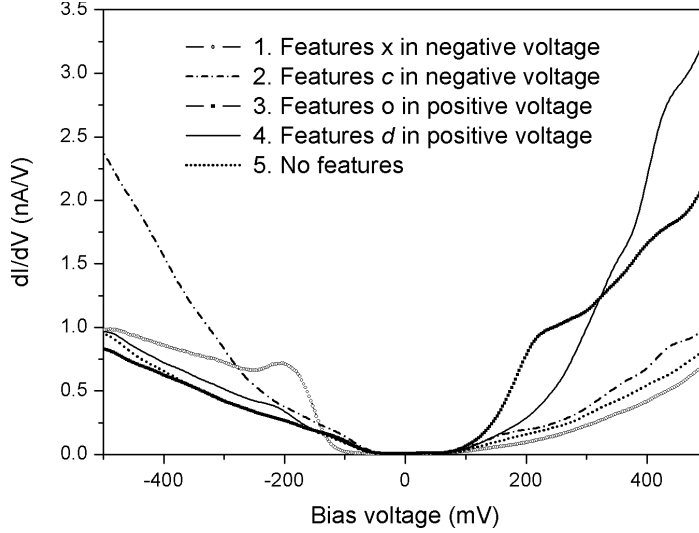


**Figure 4.12:** Five characteristic  $dI/dV$  spectra on the 0 interface layer on SiC(0001). The  $dI/dV$  curves have been averaged over 10 measurements taken at  $V = -200$  mV and  $I = 5$  pA.

identified in the photoemission experiments probably because of its lower intensity.

The localized states at -0.2 and -0.5 eV in the filled states, showing a high DOS and a flat dispersion in photoemission spectroscopy, could have caused incorrect identification of a band gap opening at the graphene Dirac point at 0.4 eV in [17]. This gap was attributed to a substrate interaction breaking the sublattice symmetry. Coincidentally, the localized states lie at the edges of the band gap, which has been determined in reference [17]. In another ARPES measurement on monolayer graphene on SiC(0001) published by Ohta *et. al* [36], no such gap has been found at the Dirac point and a different explanation of such a observation has been suggested, see discussion in [37]. Our STM and STS measurements also disprove a gap formation at the Dirac point. There is no gap or dip around the Dirac point in STS and the sublattice symmetry is unbroken on monolayer graphene (see figure 4.5).

Interestingly, the  $\sigma$  carbon bands have been found to be developed in the same way in the first graphene layer as well as in the interface layer in ARPES measurements [33]. The  $\sigma$  bands have been found at the same energy positions meaning that the average C-C bond length must be identical in both layers. Therefore, the interface layer must have carbon atoms arranged in the graphene like arrangement. Based on this fact Emtsev *et al.* [33] developed a structural model of the interface layer, which is consistent with most of the photoemission and STM data. Figure 4.13a shows this model of the interface layer, which consists of a single graphene monolayer placed

directly on the bulk-truncated SiC(0001) surface. The large black diamond indicates the unit cell of the resulting  $(6\sqrt{3} \times 6\sqrt{3})R30^\circ$  C-rich reconstruction. Previous models of the interface layer used stretched graphene layer by  $8^\circ$  in order to make it commensurate with the SiC lattice [38,39]. This resulted in a half-filled danglingbond-derived band that would account for the metallic nature of the interface, which is inconsistent with experimental findings. In the model of Emtsev, the graphene lattice is not fully commensurate with the SiC lattice, which causes that Si and C atoms are at different positions with respect to each other at different locations in the  $(6\sqrt{3} \times 6\sqrt{3})R30^\circ$  unit cell. This can be better seen in the model shown in figure 4.13b, where only underlying Si atoms of the Emtsev model are shown. The size of gray and black Si-atoms determines how distant are C-atoms in the graphene layer on top. The size of Si atoms is given by an exponential function. Gray circles show Si-atoms with C-atoms close above and black circles Si-atoms that have distant C-atoms. The overall structure of the bright features follows the  $6 \times 6$  superstructure but is inhomogeneous on the local scale in accordance to STM observations.

In the photoemission experiments on the interface layer, two types of carbon atoms ( $S1$  and  $S2$ ) next to the carbon bonded in SiC have been found by the high-resolution core level C  $1s$  spectra [33]. From the inhomogeneous structure in figure 4.13, it is clear that the strong coupling of only a part of the C atoms in the reconstruction layer to the substrate must occur. Accordingly, one-third of the C atoms in the carbon-rich interface layer strongly interacts with the dangling bonds of the underlying SiC(0001) surface, leading to component  $S1$  in reference [33]. This atomic position can be attributed to gray Si atoms in figure 4.13b that interact covalently with a C atom directly above. The other carbon atom component  $S2$  does not bind strongly to Si as found in reference [33], but only to surrounding carbons resulting in more  $sp^2$  character. These atomic positions are characterized by black Si atoms in figure 4.13b, where a Si atom is placed below the hollow part of the carbon hexagon. This must result in partly saturated Si dangling bonds because the interface layer does not show a change in the electronic and structural properties after exposing the sample to atmospheric conditions [40]. The peaks at -0.2 and -0.5 eV can be assigned to the C-atoms interacting strongly with the Si-dangling bonds (gray Si atom) of the underlying SiC(0001) surface, showing little LDOS compared to the unfilled LDOS above 0.2 eV. The other slightly more delocalized Si-saturated dangling bonds of the black atoms in figure 4.13b are probably responsible for the peaks at 0.2 and 0.5 eV. The peak at 0.5 eV with a localized character has also been observed in inverse photoemission experiments (KRIPES), which probed the empty states of graphene grown on SiC(0001) [41].

The model in figure 4.13 shows correctly two types of features that have been

#### 4. Graphene on silicon carbide

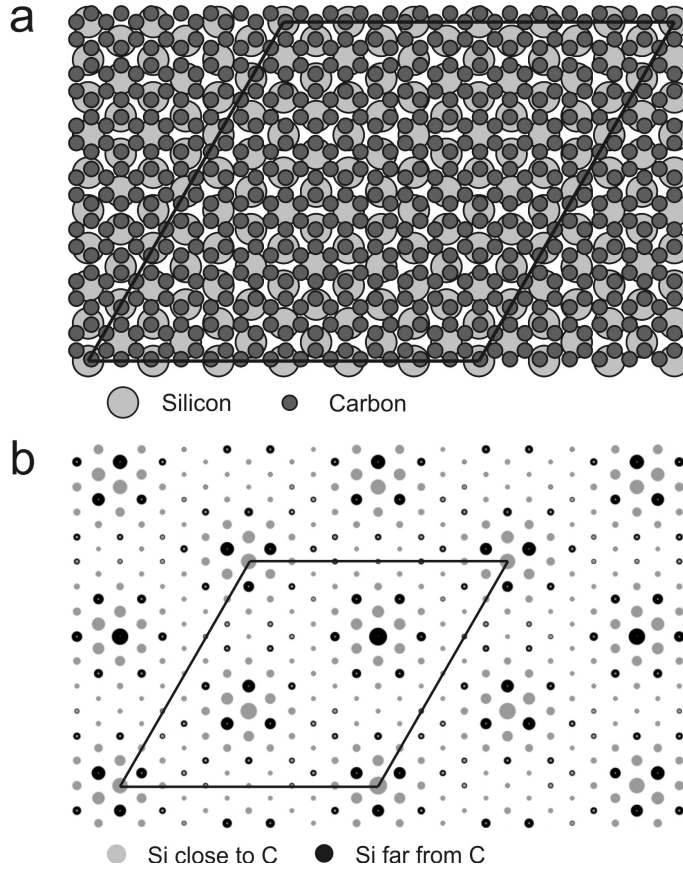


**Figure 4.13:** (a) A schematic model of graphene monolayer placed on the bulk-truncated SiC(0001) surface representing the 0 interface layer. The black diamond marks out the unit cell of the  $(6\sqrt{3} \times 6\sqrt{3})R30^\circ$  superstructure. (b) The same model showing only Si atoms, where the color and the size of the Si atom indicate the position of the nearest C-atom. Gray dots represent Si atoms with a C-atom directly above, while black Si atoms do not have C-atoms above.

found at different and near positions at negative and positive bias voltages. Even though the structure of this model does not show very good resemblance to our STM images, where a more or less disordered structure is observed, it is very alike to large scale STM images in the study of graphitization process of the SiC(0001) surface by Martensson *et al.* [21]. The disordered structure of the interface layer have probably been caused by the inhomogeneous growth resulting in only  $30 \times 30$  nm atomically flat terraces surrounded by larger defects. Therefore, our STM images of the interface layer can be explained on the base of the model shown in figure 4.13 only if adatoms or other defects in the structure are taken in to account. Thus, the structure of the

bright features could be dependent on the growth conditions as it has already been mentioned before in the connection to the different band gaps of the interface layer in our experiments and in reference [32].

#### 4.3.4 Inelastic tunneling spectroscopy

After the first graphene layer is formed, a gap-like feature is observed in STS as has been shown in figure 4.14. So the differential tunneling conductance is small at the Fermi level. From the photoemission experiments [16, 17, 33], however, one would expect a reasonable DOS at the Fermi level because of the electron doping, which causes a shift of the Dirac point to -0.45 eV [16]. Transport experiments showed likewise a higher electron density on a monolayer graphene on SiC [3, 15] than on exfoliated graphene placed on SiO<sub>x</sub>, where the Dirac point is in the vicinity of the Fermi energy [2, 42]. Thus epitaxial graphene on SiC demonstrates a metallic behavior with reasonably high mobility  $\mu = 1000 \text{ cm}^2/(\text{Vs})$  at  $T = 300\text{K}$  [15] and therefore the formation of a band gap can be excluded. Additionally, a similar gap-like feature is also observed on the graphene bilayer, see figure 4.14.

Another possibility of the appearance of the gap-like feature at the Fermi-level, as it has been presented by Zhang *et al.* [42] on exfoliated graphene supported on a silicon oxide surface, is the inability to tunnel into the  $\pi$  states due to a small tunneling probability at the Fermi-level. This is overcome by the assistance of a phonon at 63 meV coupled with  $\sigma$  states, which is making the tunneling possible at energies higher than the phonon energy. The experimental findings of Zhang *et al.* have been supported by theoretical modeling of Wehling *et al.* [43]. This was found for exfoliated graphene placed on a Si surface covered with the natural SiO<sub>2</sub> layer. In figure 4.14, it is shown that phonon contributions have also been observed on monolayer graphene on SiC(0001) in inelastic tunneling spectroscopy (IETS).

The inelastic tunneling features are usually observed as peaks (or dips) in the second derivative of the current voltage ratio at the threshold where the electronic energy associated with the bias voltage  $|eV|$  just matches the oscillator energy  $\hbar\omega$  [44]. Figure 4.14 shows two inelastic peaks in  $d^2I/dV^2$  corresponding to out of plane acoustic graphene phonons at 16 mV and 70 mV. The  $dI/dV$  and  $d^2I/dV^2$  spectra have been averaged over 4096 points. Similar phonon modes at 16 mV and 58 mV have been found before on graphite in IETS [45]. Electrons can tunnel only elastically below the phonon energy, however, when  $|eV| > \hbar\omega$ , a new inelastic channel opens and a step in the conductivity is observed. Phonon-induced inelastic tunneling in single molecules deposited on metal surfaces typically leads to conductivity changes in the order of only  $\Delta\sigma/\sigma \approx 1\%$  [46]. The normalized change in differential conductance  $\Delta\sigma/\sigma$  is directly proportional to the cross section for inelastic excitation and it is obtained



#### 4. Graphene on silicon carbide

by normalizing the peak area in  $d^2I/dV^2$  to conductance. In monolayer graphene on SiC, the inelastic peak intensities are  $\approx 10\%$  for both phonon contributions at 16 mV and 70 mV in figure 4.14. Surprisingly, the tunneling conductivity changed by a much larger factor 13 outside the gap-like feature on the exfoliated graphene [42]. This has been explained by a different mechanism based on the phonon-mediated tunneling process which involves momentum-conserving virtual transitions between 2D electron bands in graphene.

The mechanism of the phonon-assisted tunneling in graphene was supported by observation of bias dependent wavefunction spatial decay rates [42]. Below the inelastic threshold electrons have to tunnel directly into graphene states having large crystal momentum parallel to the surface ( $k_{\parallel} = K$  or  $K'$ ). Such states tend to decay rapidly in the vacuum region above a surface, since their evanescent local density of states (LDOS) falls off as  $\exp(-z/\lambda)$ , where  $\lambda^{-1} = 2\sqrt{2m\phi/\hbar^2 + k_{\parallel}^2}$  is decay length,  $\phi$  is the workfunction and  $m$  is the mass of an electron [42]. At voltages outside of the gap (i.e. at energies above the inelastic threshold), however, the tunneling can be enhanced due to the presence of frozen phonon at  $K$  ( $K'$ ) which helps mixing between the Dirac  $\pi$  electrons states at  $K$  ( $K'$ ) with the nearly free  $\sigma$  electron states at  $\Gamma$  with  $k_{\parallel} \approx 0$  [43]. Such mixed states extend further into the vacuum, leading to a larger decay length [43]. Accordingly, different tunnel decay lengths have been observed inside (0.25 Å) and outside (0.45 Å) of the gap on exfoliated graphene [42]. The bias dependent wavefunction spatial decay rates can also be seen in figure 4.15 on monolayer graphene grown on SiC. The decay rates are 0.89 Å for bias voltages in

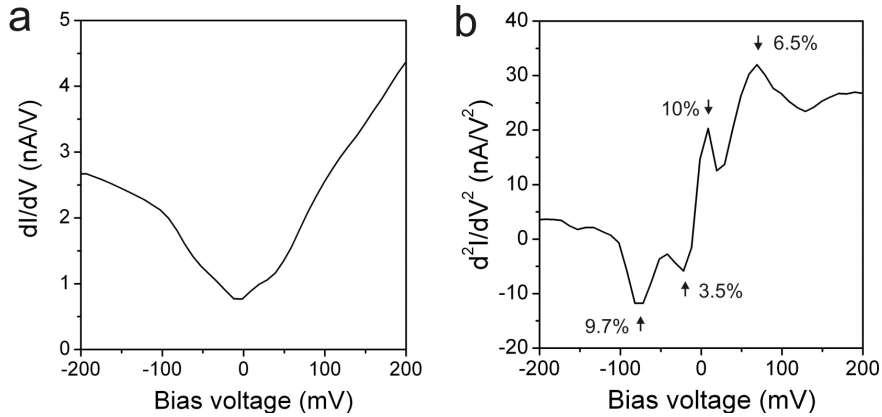


**Figure 4.14:** (a)  $dI/dV$  and (b)  $d^2I/dV^2$  spectra averaged over  $64 \times 64$  grid on graphene monolayer on SiC(0001). Inelastic peaks intensities  $\Delta\sigma/\sigma$  are indicated at the each attributed phonon peak in  $d^2I/dV^2$ . Scanning parameters:  $V = 50$  mV,  $I = 70$  pA.

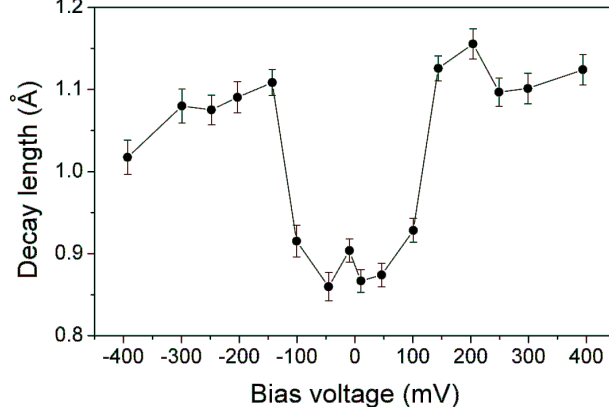


**Figure 4.15:** Tunnel current decay length of 1st layer graphene on SiC(0001) probed at different bias voltages. The decay lengths have been determined from  $I(z)$  spectroscopy at fixed  $U$  by fitting it by an exponential function  $I(z) = A \exp(-z/\lambda)$ . Error bars represent standard deviations of the measurements.

between  $\pm 100$  mV and  $1.1 \text{ \AA}$  for larger bias voltages. The decay length  $\lambda$  has been determined from  $I(z)$  spectroscopy performed at fixed bias voltage  $U$  by fitting it by an exponential function  $I(z) = A \exp(-z/\lambda)$ .

Although the results measured on epitaxial graphene in figures 4.14 and 4.15 look similar to the data by Zhang *et al.* measured on exfoliated graphene [42], the mechanism is different. Firstly, both out of plane acoustic phonon contributions at 16 meV and 70 meV have similar intensities but only latter phonon can assist the virtual tunneling to  $\sigma$  electrons since it has the right momentum because it is centered at the  $K/K'$  points, whereas the other out-of-plane acoustic phonon at 16 meV cannot play the same role because it is located at  $\Gamma$  point. Secondly, the tunneling decay rates are observed to change exactly at the edge of the gap of the interface layer (see figure 4.7), whose states are known to have a large spatial extension since they are seen even upon formation of two graphene layers above it. Thirdly, the shape of the gap-like feature is rather V like than a sharp U as expected for the phonon mediated tunneling. The ratio of the conductivity in the gap and outside is only  $(dI/dV_{out})/(dI/dV_{in}) = 3$  in our experiment in comparison to 13 in reference [42]. From comparison between our tunneling parameters  $V = 50$  mV,  $I = 70$  pA and tunneling parameters of Zhang *et al.*  $V = 0.5$  V,  $I = 100$  pA, a larger tip sample distance can be expected in our experiment, which would mean on contrary a larger  $(dI/dV_{out})/(dI/dV_{in})$  ratio. This ratio has been approximated in reference [42] by

$$(dI/dV_{out})/(dI/dV_{in}) \approx \frac{1}{7.4} \left( \frac{V_{el-ph}}{E_{\sigma}} \right)^2 \exp \left[ \left( \lambda_{k_{||}=0}^{-1} - \lambda_{k_{||}=K}^{-1} \right) z \right], \quad (4.3.1)$$

#### 4. Graphene on silicon carbide

---

where  $V_{el-ph}$  is the intrinsic graphene electron-phonon coupling matrix element connecting electronic states at the  $\Gamma$  and  $K$  points in reciprocal space and  $E_\sigma$  is the energy of intermediate states near the  $\Gamma$  point on the  $\sigma^*$  band. From this expression an experimental electron-phonon coupling strength  $V_{el-ph} \approx 0.4$  eV was extracted, which was consistent with a theoretical estimate of  $V_{el-ph} \approx 0.5$  eV based on a simple tight-binding model [47]. The estimation has been done with these parameters:  $\lambda_{k\parallel=0}^{-1} = 0.25$  Å,  $\lambda_{k\parallel=K}^{-1} = 0.45$  Å,  $E_\sigma \approx 4$  eV from ref. [48], and the STM tip height  $z \approx 5$  Å was estimated from the tip-sample junction impedance  $2 G\Omega$ . If equation 4.3.1 is applied to our results by using the same parameters except for  $\lambda_{k\parallel=0}^{-1} = 0.89$  Å,  $\lambda_{k\parallel=K}^{-1} = 1.1$  Å and  $(dI/dV_{out})/(dI/dV_{in}) = 3$ , we get the tip-sample separation  $36$  Å, which is larger than in reference [42], as expected, but unrealistic in STM. This means either that the electron-phonon coupling is extremely large ( $> 5$  eV) or the mechanism is different.

The last but the most important difference between the STM observations of Zhang *et al.* [42] on exfoliated graphene and on epitaxial graphene on SiC is a spatially inhomogeneous character of the inelastic contribution. In figure 4.16, STM topography images together with  $dI/dV$  and  $d^2I/dV^2$  maps have been measured simultaneously on the same area on a graphene monolayer grown on SiC(0001). The  $d^2I/dV^2$  images depict intensities of the inelastic peak contribution of the phonon mode at  $\pm 70$  mV. Surprisingly, the peak intensities vary spatially by a large factor reaching values around 50 among some places. Similarly like for the bright features, the high IETS intensities are not at the same locations in the positive and negative bias voltage. The places of the high inelastic peak intensity coincides with places where localized states at  $\pm 200$  mV are observed in  $dI/dV$  (see figure 4.16).

Three extreme local  $dI/dV$  and  $d^2I/dV^2$  spectra and the spatially averaged spectra from figure 4.16 are exhibited in figure 4.17. The local spectra have been averaged only over 10 measurements, therefore they have a larger noise level in comparison to the averaged spectra. STS and IETS curves measured on places with a high inelastic IETS feature at -70 mV are presented in figure 4.17a. They are located at positions where the localized states at -200 mV are observed in STM. The intensity of the inelastic feature reaches a gigantic value  $\Delta\sigma/\sigma \approx 50\%$  in negative bias voltage, while the IETS peak in positive voltage is a half-size. Moreover, a second harmonic phonon mode is observed at -140 mV in  $d^2I/dV^2$  with a intensity approximately 5 times smaller than the intensity of the first harmonic mode. Figure 4.17b represents places with a high inelastic peak at +70 mV that are positioned on the bright features observed in positive bias voltage and characterized by localized states at 200 mV. Similarly like for the previous IETS spectra, an enormous inelastic peak intensity together with the second harmonic contribution are observed but only for

### 4.3 Results and discussions

the inelastic peak in the positive bias voltage. Characteristic  $dI/dV$  and  $d^2I/dV^2$  spectra obtained on locations displaying a small IETS contribution at  $\pm 70$  mV are shown in figure 4.17c. The inelastic phonon fingerprints demonstrate the normalized change in differential conductance only  $\Delta\sigma/\sigma \approx 10\%$  for both phonons at 16 mV and 70 mV. No second order phonon modes are seen in this IETS spectra. The averaged  $dI/dV$  and  $d^2I/dV^2$  curves over the whole STM area in figure 4.16 are shown in figure 4.17d. Three inelastic excitations are observed at 16 mV, 70 mV and 140 mV, where the highest intensity has the phonon at 70 mV which shows even its second harmonic.

The shape of the gap-like feature is different for all three characteristic local measurements in figure 4.17. While it is U-like at the places where a large inelastic phonon contribution at  $\pm 70$  mV together with localized states of the interlayer are measured,

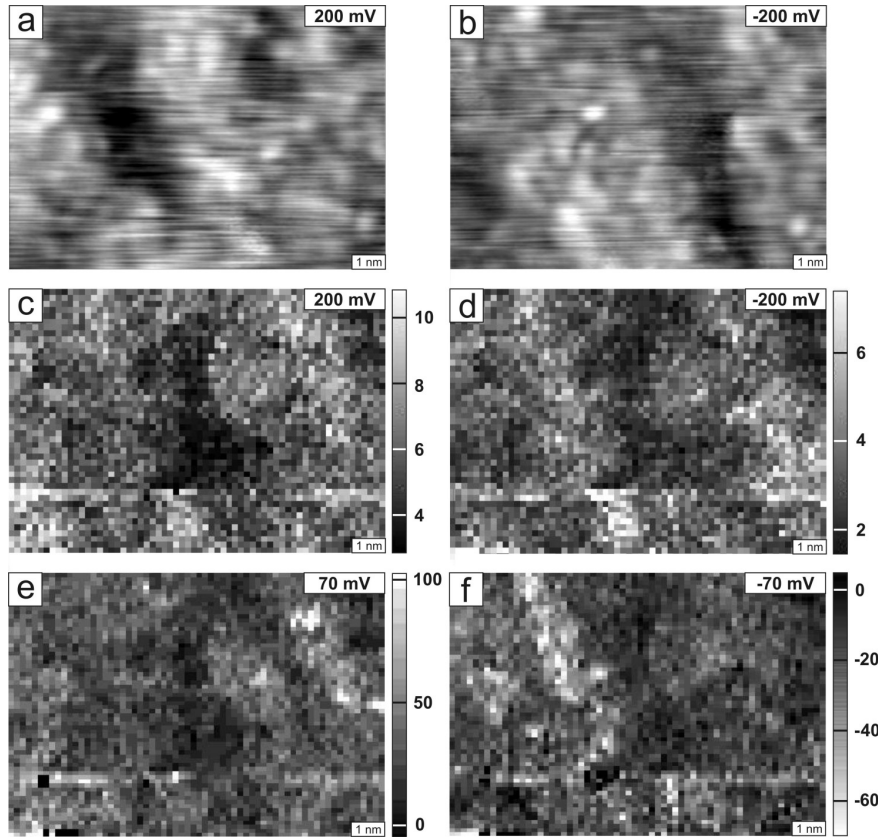


**Figure 4.16:** STM, STS and IETS images of the same  $12 \times 8 \text{ nm}^2$  area on graphene monolayer on SiC.  $dI/dV$  and  $d^2I/dV^2$  maps were taken with  $U = 50$  mV and  $I = 50$  pA.

#### 4. Graphene on silicon carbide

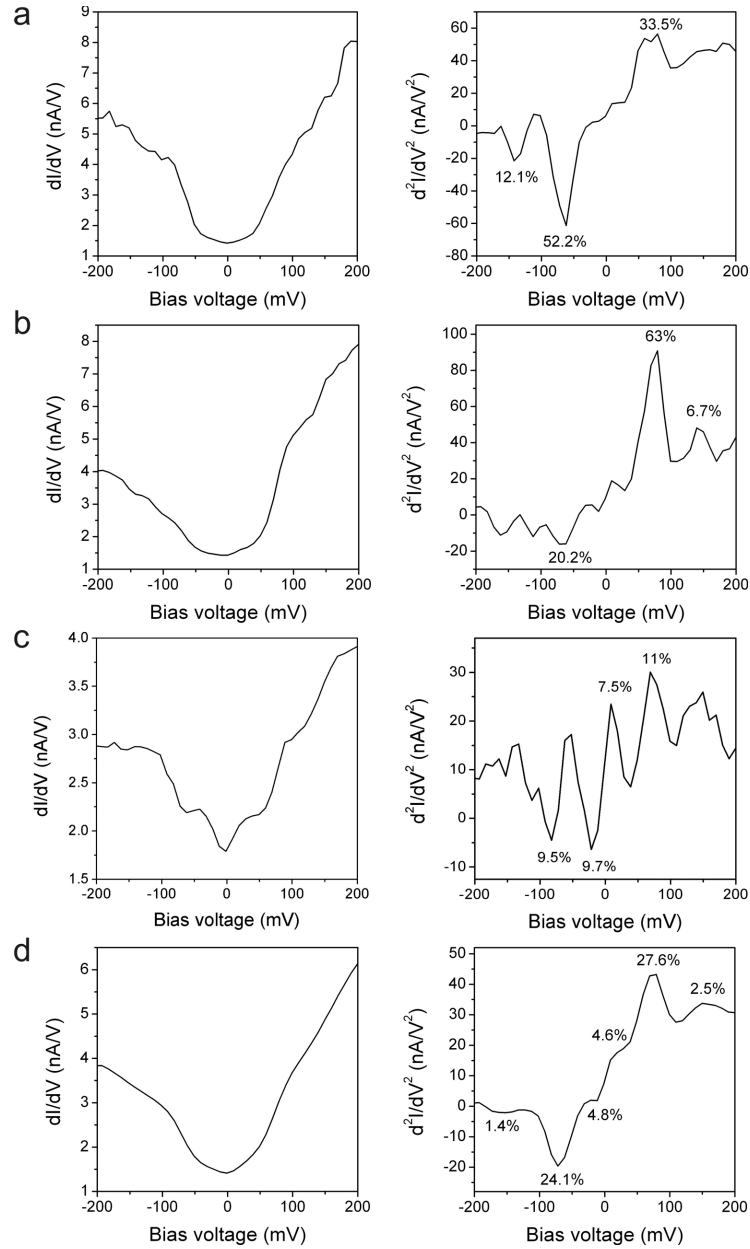


**Figure 4.17:**  $dI/dV$  and  $d^2I/dV^2$  spectra on graphene monolayer on SiC taken at  $V = 50$  mV and  $I = 50$  pA. The spectra represent curves from figure 4.16 showing: large inelastic contribution in negative bias voltage (a), large inelastic contribution in positive bias voltage (b), small inelastic contribution (c), and the spatial average (d). The local spectra have been averaged over 10 measurements.

it is stepped V shape at the places where no localized states exist. The averaged  $dI/dV$  curve in figure 4.17 contains both contributions which makes the the shape of the gap-like feature something in between V and U. The gap-like feature would be present in the  $dI/dV$  even if the inelastic channels would not have contributed to the tunneling current. This can be better seen on the  $dI/dV$  curve in 4.17c, where the additional inelastic tunneling channels create steps in the conductance. Even if these inelastic channels were removed a reduction at the Fermi level will be present. Therefore, strong inelastic fingerprints of phonos are not fully responsible for such a gap-like feature on graphene grown on SiC(0001) but are representations of another phenomenon which will be introduced in section 4.3.6.

The observation of large phonon contribution in IETS on the places imprinted by localized states can be explained on the basis of the normal inelastic tunneling in the presence of a large electron-phonon coupling. A nonequilibrium Green's function formalism for inelastic tunneling is used for this purpose to find the highest possible inelastic contributions in the STM experiments in the following section. This theory will demonstrate on a simplified model that the largest asymmetric inelastic peaks are expected to be observed in IETS exactly on places with narrow localized states if a large electron-phonon coupling is present.

### Inelastic tunneling theory with nonequilibrium Green's function formalism

In this section the general nonequilibrium Greens function formalism of an inelastic electron tunneling through a junction consisting of a graphene layer (molecule) is described. The effect of the mutual influence between the phonon and the electron subsystems on the electron tunneling process is considered within a general self-consistent scheme according to work of Galperin *et al.* [44]. This many-body theory takes correctly into account the influence of the contact population, the effects of the electronic subsystem on the phonon dynamics, and as well as interference effects which are disregarded in simpler elastic scattering approaches using Landauer formalism [44, 49].

In figure 4.18, the system under study is schematically illustrated. The tip and substrate are represented by a left and a right lead, which are free electron reservoirs in thermal equilibrium and coupled through a bridging graphene system. Graphene electronic structure is modeled as a one electron level for simplicity. The assumption that the electrodes are in thermal equilibrium under the steady-state operation of the junction corresponds to a weak coupling situation (i.e., conduction much smaller than  $e^2/\pi\hbar$ ), which characterizes well most of the molecular junctions [44]. Graphene phonon modes with energy  $\hbar\Omega_0$  are divided into two groups. The primary phonons interact with the electronic system, whereas the secondary phonons couple only to

#### 4. Graphene on silicon carbide

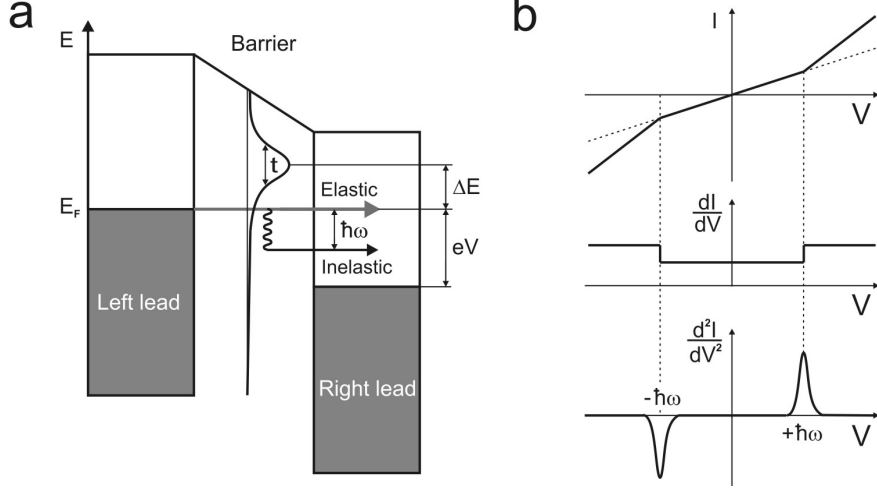


**Figure 4.18:** Diagram of the level structure in inelastic tunneling (a) and its signature in  $I/V$ ,  $dI/dV$  and  $d^2I/dV^2$  spectra in STM (b). Only one electron level is assumed in the position of graphene for simplicity.

the primary phonons. The secondary phonons represent the environment which is assumed to be in thermal equilibrium. Electron-phonon interaction in the leads is disregarded. In this system, the primary phonons are driven by the non equilibrium electronic system, while interchanging energy with their thermal environment. The general zero-order Hamiltonian in second quantization takes the form

$$\hat{H}_0 = \sum_{i,j} t_{i,j} \hat{c}_i^\dagger \hat{c}_j + \sum_{k \in L,R} \epsilon_k \hat{d}_k^\dagger \hat{d}_k + \sum_l \Omega_l \hat{a}_l^\dagger \hat{a}_l + \sum_m \omega_m \hat{b}_m^\dagger \hat{b}_m. \quad (4.3.2)$$

The four terms on the right hand side represent respectively electrons on the graphene system (molecule) and in the leads, the primary subset of phonon harmonic modes and secondary subset of harmonic modes representing the thermal environment. In the first term,  $\hat{c}_i^\dagger$  ( $\hat{c}_i$ ) are creation (annihilation) operators for electrons in the graphene bridge and  $t_{ij} = E_i$  is interstate coupling, where  $E_i$  is the energy of electronic state  $i$ . Electron states in left and right lead with their corresponding creation (annihilation) operators  $\hat{d}_k^\dagger$  ( $\hat{d}_k$ ) and energies  $\epsilon_k$  are labeled by  $k \in L, R$ . The wide band limit is assumed for them, which means that the electronic levels in the leads form a continuous band with a flat density of states. Primary phonon states in the molecular bridge labeled by  $l$  are represented by creation (annihilation) operators  $\hat{a}_l^\dagger$  ( $\hat{a}_l$ ) and energies  $\hbar\Omega_l$ . Primary phonon states are phonon states which couple to electron states. In the last term,  $\hat{b}_m^\dagger$  ( $\hat{b}_m$ ) are creation operators for the secondary phonon states in the bridge, which are labeled by  $m$  and have energies  $\hbar\omega_m$ . Secondary phonon states do not couple to electron states.

The zero-order description is complemented by the interaction Hamiltonian

$$\hat{H}_1 = \sum_{k \in L, R; i} (V_{ki} \hat{d}_k^\dagger \hat{c}_i + V_{ik} \hat{c}_i^\dagger \hat{d}_k) + \sum_{l, i} M_i^l \hat{A}_l \hat{c}_i^\dagger \hat{c}_i + \sum_{l, m} U_m^l \hat{A}_l \hat{B}_m, \quad (4.3.3)$$

where  $\hat{A}$  and  $\hat{B}$  are phonon displacement operators, defined as  $\hat{A} = (\hat{a}_l^\dagger + \hat{a}_l)$  and  $\hat{B} = (\hat{b}_m^\dagger + \hat{b}_m)$ . The three terms in 4.3.3 represent, respectively, coupling between electron states  $i$  and the leads  $k \in L, R$  denoted by  $V_{ki}$ , coupling of the primary phonons to the electronic system,  $M_m^l$ , and interaction of the local phonon modes with their thermal environment,  $U_m^l$ .

In general, the eigenstates of the Hamiltonian  $\hat{H} = \hat{H}_0 + \hat{H}_1$  cannot be calculated exactly. However, some of the properties of a system such as the total current through the junction (equation A-31) and the density of electronic states on the bridge (equation A-32) can be deduced by using Green's functions. This approach is called the non equilibrium Green's function (NEGF) approach. The exact description of this formalism using the self-consistent Born approximation can be found in appendix or in references [44, 50]. In short, it starts with a  $\hat{H}_0$  such that  $\hat{H} = \hat{H}_0 + \hat{V}$ , where  $\hat{H}_0$  is a Hamiltonian that may be solved exactly and  $\hat{V}$  is the rest of the total Hamiltonian, whose effects are small. Then it uses an iteration approach where the input starts with a system completely described by  $\hat{H}_0$  to which  $\hat{V}$  is added and the change of the system is studied. This is repeated till convergence when the initial and final states are identical. The main parameters in the NEGF model are: the electron phonon coupling  $M$ , the inherent width of the electronic level  $t$ , the position of the electronic level with respect to the Fermi level of the leads  $\Delta E$ , and the couplings to the left and right leads  $\Gamma_L$  and  $\Gamma_R$ , respectively.

Our model describes situations with a weak electron-phonon coupling in a non resonant regime. The NEGF method is based on perturbation theory with the electron-phonon coupling  $M$  as the perturbation parameter. This is valid only if  $M$  is small in comparison to the inverse traversal time [50], which determines how long the electron stays on the electronic level of graphene during tunneling. The condition of a weak electron-phonon coupling thus imposes the limitation of our approach

$$\left| \frac{M}{\sqrt{\Delta E^2 + \Gamma^2}} \right| \ll 1. \quad (4.3.4)$$

The model is valid only if the molecule-lead coupling is not too large, the width of the electronic level is not too narrow and the position of the electronic level is not very close to the Fermi level of the leads. If the molecule-lead coupling was so strong that the electron transmission probability would be nearly 1, depletion of the electrons can occur in the negatively biased lead with energies in the conduction window (i.e. between the Fermi energy of the left lead and the Fermi energy of the



#### 4. Graphene on silicon carbide

---

right lead). This would give rise to an increased reflection at the onset  $eV = \hbar\Omega$ , which is otherwise prohibited by the Fermi exclusion principle, and a negative step in the contribution appears like it has been observed in a point contact spectroscopy [51]. Since assumption 4.3.4 must hold to use perturbation theory and  $\Gamma$  must be small to use leads in thermal equilibrium,  $\Delta E$  must be large, which implies that this model is only valid for the non resonant regime.

In figure 4.19, the modeled  $dI/dV$  and  $d^2I/dV^2$  spectra using the NEGF method containing one electronic level in the tunneling barrier are shown. Two special cases are considered. The first one describes a situation where a broad electronic level with  $t = 20$  eV is placed in the tunneling barrier. The second case demonstrate an infinitely sharp electronic level which is broadened only by the coupling to the leads  $\Gamma_L = \Gamma_R = 0.15$  eV. Except for the inherent broadening parameter, the same calculation parameters have been used in both cases:  $M = 0.4$  eV,  $\Gamma_L = \Gamma_R = 0.15$  eV,  $\Delta E = 1$  eV and  $\hbar\Omega = 130$  meV. As a result very small inelastic peaks are observed for the broad electronic level, where only the first harmonic phonon mode arises in  $d^2I/dV^2$  having peak intensities  $\Delta\sigma/\sigma = 0.05\%$ . On the other hand, the sharp electronic level has produced much larger inelastic features showing both the first harmonic contribution and the second harmonics. Moreover, there is an obvious asymmetry between the inelastic peaks observed in positive and negative bias voltages. The IETS peaks in positive bias voltage, which are close to the electronic level, have  $\Delta\sigma/\sigma(+\hbar\Omega) = 7.1\%$  and  $\Delta\sigma/\sigma(+2\hbar\Omega) = 1\%$ , while the peaks in negative voltage are  $\Delta\sigma/\sigma(-\hbar\Omega) = 6.7\%$  and  $\Delta\sigma/\sigma(-2\hbar\Omega) = 0.5\%$ . This result shows qualitatively consistent picture with the IETS experimental observations on graphene on SiC, where asymmetric peaks have been observed on the places containing localized electron states. However, a quantitative matching could not been reached since the result in figure 4.19b is at the limit of our approach and shows the highest possible inelastic peak intensities.

The role of different NEGF parameters on the inelastic peak intensity is presented in table 4.1. Both first and second phonon harmonics were studied. In general, the largest influence on the intensity had the shape of the electronic level and the magnitude of the electron-phonon coupling. In order to get the largest inelastic signatures, large  $M$  and small  $t$  have to be used. The couplings to the leads affected the intensity of IETS peaks in such a way that the symmetric couplings to both leads  $\Gamma = \Gamma_L = \Gamma_R$  have produced the largest  $\Delta\sigma/\sigma$  and therefore it has been used in all results shown in table 4.1. For smaller couplings  $\Gamma$  a larger  $\Delta\sigma/\sigma$  was obtained. The position of the electronic level  $\Delta E$  has also modified the IETS peak intensities, however, this parameter has been studied in very limited range (see table 4.1). Smaller  $\Delta E$  gave rise to higher IETS intensities. The calculations using a large electron-phonon cou-

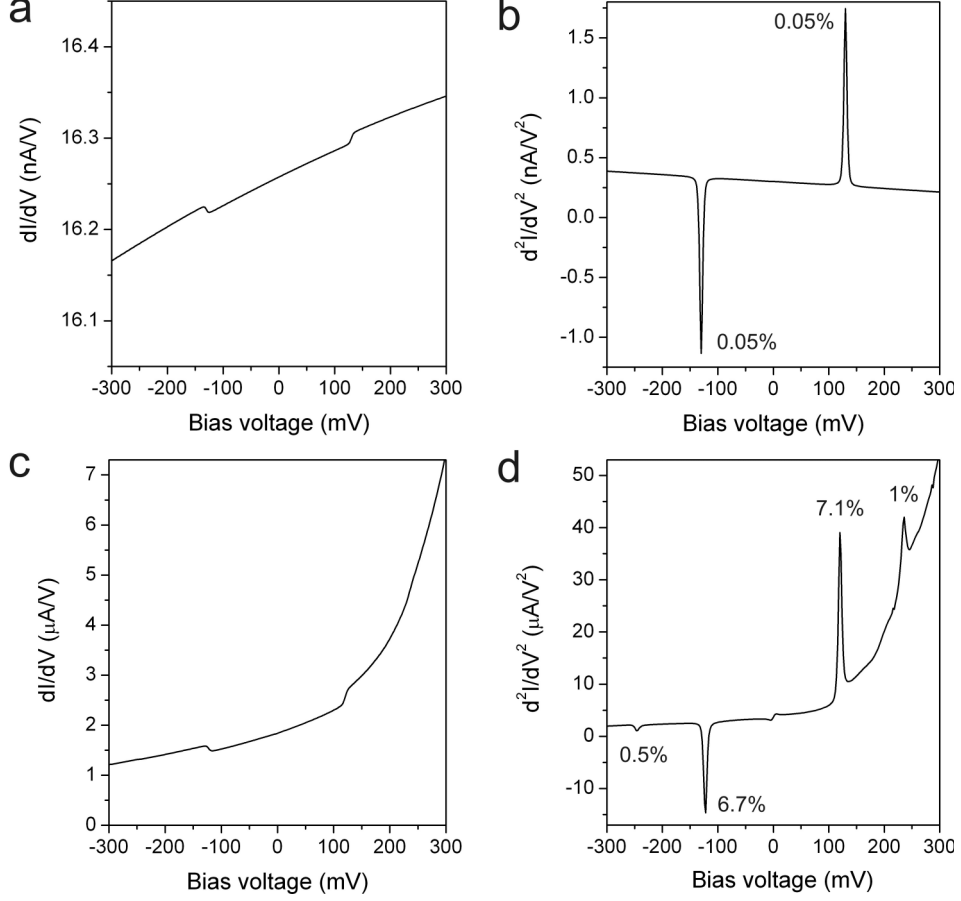


**Figure 4.19:** Modeled  $dI/dV$  and  $d^2I/dV^2$  spectra using the non equilibrium Green's function method (NEGF) in the non resonant case. (a) and (b) have been calculated with a broad 20 eV energy level; and (c) and (d) with an infinitely sharp energy level, which was broadened only via coupling to the leads. The IETS peak intensities  $\Delta\sigma/\sigma$  are indicated next to the IETS peaks. NEGF parameters:  $M = 0.4$  eV,  $\Delta E = 1$  eV,  $\Gamma_L = \Gamma_R = 0.15$  eV and  $\hbar\Omega = 130$  meV.

plings ( $M = 5$  eV) had problems with convergence and resulted in spikes at higher energies in  $dI/dV$  and  $d^2I/dV^2$  spectra. The second harmonic contribution together with the asymmetry between the negative and positive bias voltage IETS peaks have been observed only for narrow electronic states which were close to the Fermi level.

The limitation of our NEGF model given by expression 4.3.4 does not allow us to correctly mimic the experimental conditions in the IETS experiment in figure 4.17. These parameters would be required for it:  $\Delta E = 0.2$  eV,  $\Gamma_L = \Gamma_R = 0.1$  eV and  $M > 0.5$  eV in order to produce inelastic peaks with larger intensities than  $\Delta\sigma/\sigma \approx$

#### 4. Graphene on silicon carbide

---

**Table 4.1:** The influence of the parameters in the NEGF model  $t$ ,  $M$ ,  $\Delta E$  and  $\Gamma$  on the IETS peak intensities  $\Delta\sigma/\sigma$ . Parameter  $t$  determines the half width of the electronic level,  $M$  is electron-phonon coupling,  $\Delta E$  denotes position of the electronic level and  $\Gamma = \Gamma_L = \Gamma_R$  is coupling to the leads. The phonon energy is  $\hbar\Omega = 130$  meV and  $2\hbar\Omega$  denotes the second harmonic contribution. The units of the NEGF parameters are in eV and IETS intensities are in %.

$t$	$M$	$\Delta E$	$\Gamma$	$\frac{\Delta\sigma}{\sigma}(+\hbar\Omega)$	$\frac{\Delta\sigma}{\sigma}(-\hbar\Omega)$	$\frac{\Delta\sigma}{\sigma}(+2\hbar\Omega)$	$\frac{\Delta\sigma}{\sigma}(-2\hbar\Omega)$
20	0.3	1	0.2	0.0278	0.0278	0	0
20	0.4	1	0.15	0.0473	0.0473	0	0
20	0.4	0.9	0.15	0.0474	0.0474	0	0
0	0.1	1	0.2	0.2	-	0.01	-
0	0.3	1	0.2	3.1	-	0.09	-
0	0.4	1	0.2	6.6	6.4	0.69	0.45
0	0.4	1	0.15	7.1	6.7	1.0	0.5
0	0.4	0.9	0.2	7.8	7.0	1.3	0.7
0	0.4	0.9	0.15	9.0	8.3	1.4	1.0
0	0.5	1	0.2	13.0	-	1.9	-

50%. Nevertheless, the results of our NEFG model have shown a promising route how to reach such a large inelastic contribution in IETS. This means a large electron-phonon coupling and the presence of the sharp electronic level in the vicinity of the phonon energy. In order to perform a correct calculation to describe experimental conditions another perturbation parameter than  $M$  has to be used.

From the strong inelastic phonon signatures in IETS on graphene grown on silicon carbide it can be concluded that the electron-phonon coupling is large in this system. NEFG model of the IETS curves has shown that it has to be even larger than the predicted value  $\approx 0.5$  eV by a simple tight-binding model [47] to be able to produce IETS peak intensities  $\Delta\sigma/\sigma \approx 50\%$ . This is, however, valid only for the phonon mode at 70 meV with  $K$  or  $K'$  symmetry points. The other phonon 16 meV centered at  $\Gamma$  point has produced much smaller IETS peaks ( $\Delta\sigma/\sigma \approx 10\%$ ), meaning that the electron-phonon coupling is smaller at  $\Gamma$  point and it can be close to the theoretically predicted value in [47]. The electron phonon coupling in graphene on SiC(0001) seems to be thus anisotropic having a larger electron-phonon coupling at  $K$  or  $K'$  points. Similar conclusions have been drawn in a self-consistent analysis of the photoemission spectra on graphene monolayers grown on SiC(0001), where kinks have been observed in the electronic dispersion near the Fermi level which have attributed to many-body interactions [52,53]. The electron-phonon couplings extracted from the modeled photoemission spectra have been found to be anisotropic and much larger (3.5-5 times) than theoretically predicted values [52]. In intercalated thin graphite CaC<sub>6</sub>, similarly,

the electron-phonon coupling has been found to be anisotropic with the electron-phonon coupling constant ranging from 0.39 (for  $\varphi \approx 0^\circ$ ) to 1.54 (for  $\varphi \approx 60^\circ$ ) [54]. The momentum averaged value was 0.67 [54]. Such a strong electron-phonon coupling could explain the pairing mechanism in this superconductive material with  $T_C = 11.6$  K [54].

### 4.3.5 Electron scattering in graphene monolayer

Structural defects act as scattering centers for free electrons as it has been demonstrated with STM on metal surfaces at low temperatures [55]. Scattered electron waves interfere with the incoming waves giving rise to local modifications of the electron density which generates standing wave patterns in the surrounding of defects known as Friedel oscillation. Friedel oscillation can be seen as a result of the screening of the impurity charge by the conducting electrons. Detailed information on the Friedel oscillations around the defect can be obtained by a STM and STS analysis of the standing electron wave around the scattering center. The period of the corresponding modulation of the electronic density is the inverse of twice the Fermi wave vector  $k_F$ , which is in general not an integer multiple of the underlying crystal lattice [56]. In graphite, Friedel oscillations are characterized by the  $(\sqrt{3} \times \sqrt{3})R30^\circ$  superstructure, which has been observed around point defects, step edges and grain boundaries of graphite in STM [28, 29, 57]. The same pattern has also been found around point defects in graphene [26].

Graphene quasiparticles may scatter and interfere due to the presence of short-range potentials which are arising from atomic-scale defects that locally break the symmetry of the Hamiltonian [58]. This leads to a violation of the quasiparticle symmetry conservations. Such elastic scattering by short range potentials mixes electron states of the same energy but different wavevectors  $\mathbf{k}$ , which may lie on the same constant energy contour (intravalley scattering) or on different contours of the same energy (intervalley scattering) [26]. In either case, the presence of a backscattering component results in a standing-wave pattern from the superposition of incident and scattered Bloch states,  $\mathbf{k}_1$  and  $\mathbf{k}_2$ . The wavevector of the standing wave is  $\mathbf{k} = \mathbf{k}_2 - \mathbf{k}_1$  with wavelength  $\lambda = 2\pi/k$ . This scattering wavelength is determined from the quasiparticle energy-momentum dispersion relation  $E(\mathbf{k})$ . Scanning tunneling microscopy is a powerful tool to map these scattering wave oscillations on the nanometer scale with a high energy resolution giving thus opportunity to study the quasiparticle dispersion relation [59].

In figure 4.20, a STM image and its corresponding fast Fourier transformation (FFT) image of graphene monolayer on SiC(0001) are shown. Low bias voltage  $U = -50$  mV has been applied between the STM tip and the graphene sample in order to

#### 4. Graphene on silicon carbide

probe electrons at the Fermi level. The real-space  $(\sqrt{3} \times \sqrt{3})R30^\circ$  superstructure is seen all over the STM topography in figure 4.20a. It is demonstrated by a hexagonal pattern showing a larger lattice periodicity than the graphene atomic mesh. In the reciprocal space shown by the FFT image in figure 4.20b, the  $(\sqrt{3} \times \sqrt{3})R30^\circ$  pattern forms six spots at  $K$  and  $K'$  points of the first graphene Brillouin zone. The larger pattern surrounded by six satellite spots in the FFT image belong to the graphene lattice. No structural defects have been found on the graphene surface in the scanned area. The same STM image has already been shown in figure 4.8, where the graphene surface was probed at different bias voltages. Since the electronic modifications of the electron density caused by structural defects extend even up to 9 nm from defects as it has been shown in another STM study of point defects in a graphene bilayer on SiC(0001) [26], it is not possible to determine whether this pattern is caused by defects lying out of the  $10 \times 10 \text{ nm}^2$  scanning area or by the presence of the localized electron states sticking out from the interface layer. The first option is quite probable since only  $30 \times 30 \text{ nm}^2$  atomically flat areas surrounded by undefined regions have been formed on our SiC(0001) surface owing to the inhomogeneous heating procedure caused by e-beam heating in UHV.

The electron scattering from point defects can be better visualized by mapping directly the local electron density around point defects at low bias voltages. Figure 4.21 depicts STM topography,  $dI/dV$  and  $d^2I/dV^2$  maps of a  $10 \times 10 \text{ nm}^2$  area on monolayer graphene with a structural defect in the middle. The point defect appear as a bright protrusion in the STM and  $dI/dV$  images and as a dark spot in the  $d^2I/dV^2$  images. The electron scattering from the defect is observed as a circular standing

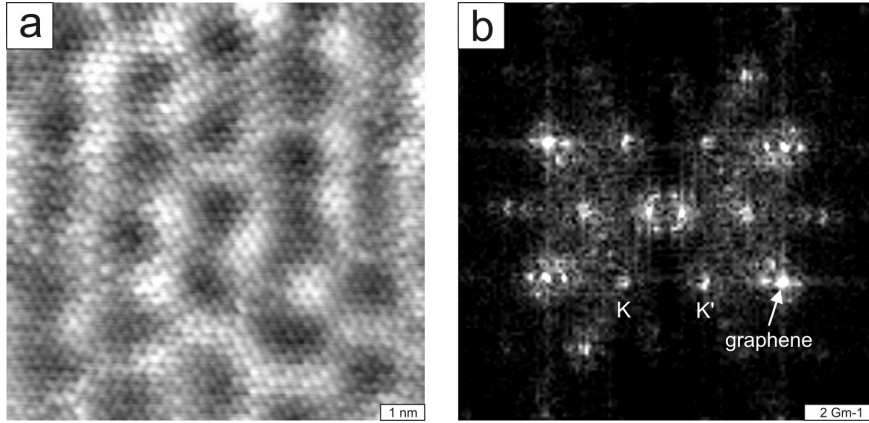


**Figure 4.20:** STM image of a  $10 \times 10 \text{ nm}^2$  area on the 1st graphene layer on SiC(0001) taken with  $U = -50 \text{ mV}$  and  $I_t = 5 \text{ pA}$ . (b) FFT image of a current STM image showing the  $(\sqrt{3} \times \sqrt{3})R30^\circ$  superstructure and the graphene lattice.

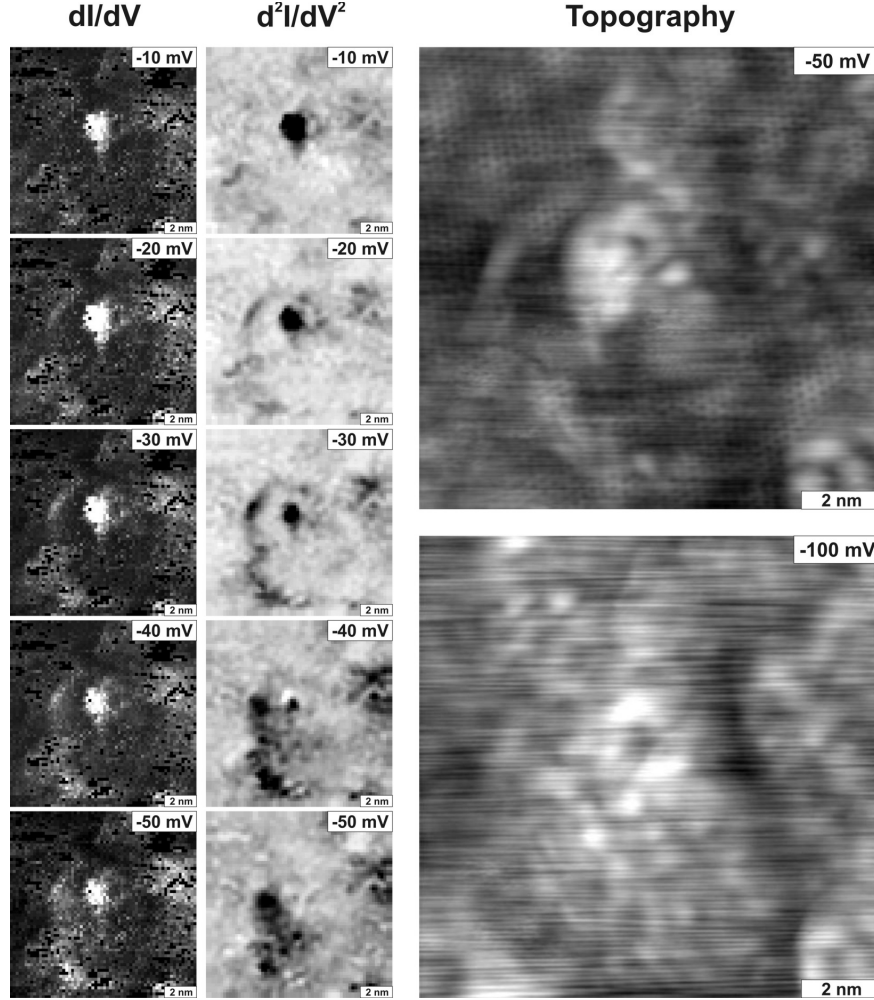


**Figure 4.21:** Electron scattering from a defect in monolayer graphene on SiC(0001) obtained at different bias voltages. The defect appear as a bright protrusion in STM topography and  $dI/dV$ , while it shown as a dark spot in a  $d^2I/dV^2$  map. The electron wave front can be seen the best in the  $d^2I/dV^2$  map, because of the small intensity. Scanning parameters:  $10 \times 10 \text{ nm}^2$ ,  $U = 50 \text{ mV}$  and  $I_t = 50 \text{ pA}$ .

wave in both  $dI/dV$  and  $d^2I/dV^2$  maps. By changing the bias voltage the circular electron wave front surrounding the defect changes its size. This is better seen in the  $d^2I/dV^2$  map because of the small intensity of the circular pattern in  $dI/dV$ . The size of the ring representing the scattered electron wave front increases as the bias voltage is decreased (see figure 4.21). The diameter of ring represents the wavelength of the scattered electron wave,  $\lambda = 2\pi/k$ . The wavevector of the scattered wave  $k$  is

#### 4. Graphene on silicon carbide

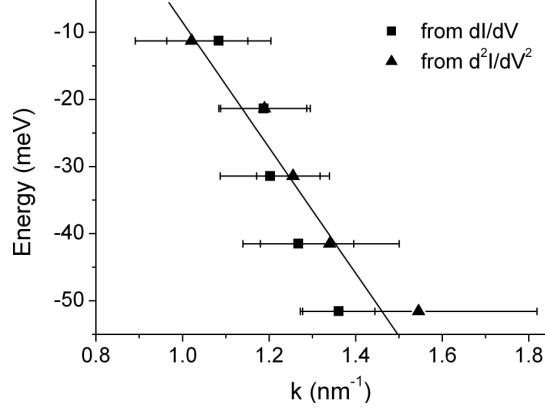


**Figure 4.22:** Dispersion relation of energy  $E$  and momentum  $k$  of the scattered electrons from a defect shown in figure 4.21. The  $k$  was determined from the diameter of the ring either using  $dI/dV$  or  $d^2I/dV^2$  maps. The points have been fitted by  $y = (-93 \pm 14)x + (85 \pm 17)$ .

shown as a function of bias voltage in figure 4.22. It represents the electron energy dispersion relation  $E(k)$ . The scattering wave vectors have been determined by two ways: from  $dI/dV$  and  $d^2I/dV^2$  maps.

In figure 4.21, an linear dependence between energy and momentum is observed as expected for single layer graphene on SiC  $E = v_F \hbar k + E_D$ , where  $E_D$  denotes the position of the Dirac point due to a electron doping from the SiC substrate. The effective velocity extracted from the linear fit is  $v_F = (1.4 \pm 0.2) \times 10^5$  m/s and the position of the Dirac point is  $E_D = (85 \pm 17)$  meV. Surprisingly, the Dirac point is not at -450 meV as it was observed by ARPES on graphene monolayer on SiC(0001) at room temperature [16,17], but at positive energy. The effective velocity is also smaller than expected value for free standing graphene 1/300 of the velocity of light [1]. On the bilayer graphene on SiC(0001), similar determination of the dispersion relation using STM has been reported [26]. A slightly different method has been used to determine the dispersion relation in this STM study. The size of spots at the K and K' points of graphene corresponding to the scattered electron waves has been measured in FFT transformed  $dI/dV$  maps. The determined effective velocity and position of the Dirac point were  $v_F = 9.7 \times 10^5$  m/s and  $E_D = -330$  meV [26]. These values corresponded well to the photoemission experiments on the bilayer graphene on SiC [36]. The reason can lie in the quality of graphene layers formed on SiC(0001) in the experiments of Rutter *et al.* [26] and in our experiment. The disordered structure together with the small sizes of atomically flat areas on our graphene sample could cause the smaller electron effective velocity and the shift of the Dirac point can be only local.

### 4.3.6 Is graphene on SiC a 2D superconductor?

So far, it has been shown that the interface layer contains strongly filled and unfilled localized states in energy as well as in real space. The localized states are randomly distributed over the interface layer, causing large electronic disorder in the interface layer and maybe in the first and second graphene layers as well. The V-shaped gap-like features measured at 5 K on a graphene monolayer and bilayer (see figure 4.7) show a reduction of the tunneling conductivity at the Fermi energy. This gap-like feature seems to be closely related to graphene phonons because it starts exactly at the energy (70 meV) of the out of plane acoustic phonon (K point). These observations on graphene grown on SiC show a resemblance to the behavior of superconductors, which have often disordered structure, exhibit similar reduction at the Fermi level, called pseudogap, and the mechanism of Cooper pairing is mediated by phonons in some superconducting materials (BCS theory) [60]. The characteristics of superconductivity in a material appear when the temperature is lowered below a critical temperature  $T_C$ . The transition to superconducting state is accompanied by abrupt changes in various physical properties, for instance by a sudden drop of the resistivity to zero below  $T_C$  at low currents.

Temperature dependent electron transport in few-layer graphene on SiC(0001) has been investigated by four-point probe measurements using van der Pauw method [61]. This method effectively eliminates contact resistivity, giving rise to a correct sheet resistance of the measured sample. The resistance measurements have been conducted in an automated probe station setup equipped with a flow cryostat in He atmosphere. The resistance has been measured on the same graphene/SiC sample that has been characterized by STM, STS and IETS in the previous sections. In order to make electric connection, four copper wires have been silver-glued on top of the graphene layer.

Figure 4.23 shows sheet resistance of the few-layer graphene on SiC(0001) measured as a function of temperature. When the graphene sample was cooled down from room temperature, the in-plane resistance slowly rose from  $1.2 \times 10^{-4} \Omega$  to a saturation value  $\approx 3.5 \times 10^{-4} \Omega$  below 100 K. A similar rise of resistance has also been observed in highly oriented pyrolytic graphite (HOPG) [62]. Such a behavior is not expected for a metal, where resistance diminishes with decreasing temperature, and it represents rather the behavior of insulators. More surprisingly, a dramatic drop of resistance is observed at very low temperatures. This drop in resistance is better depicted in figure 4.24, where the sheet resistance is plotted in a smaller temperature range around the drop as a function of magnetic field applied perpendicular to the graphene plane. The fall of graphene resistance is almost by two orders of magnitude from  $5 \times 10^{-4} \Omega$  to  $2 \times 10^{-5} \Omega$  at  $B = 0$  T. The onset of the resistance drop, charac-



#### 4. Graphene on silicon carbide

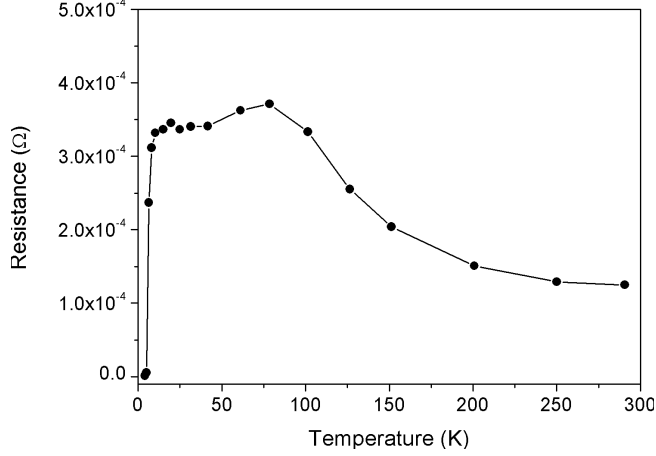


**Figure 4.23:** Sheet resistance of few-layered graphene on SiC(0001) measured as a function of temperature in zero magnetic field and  $I = 1 \mu\text{A}$ .

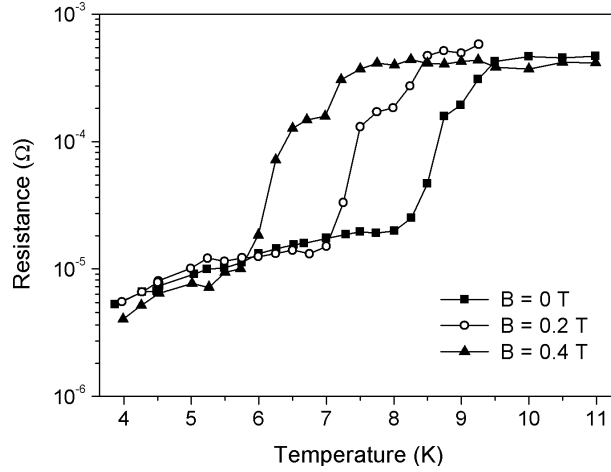


**Figure 4.24:** Sheet resistance (logarithmic scale) of few-layered graphene on SiC(0001) versus temperature for the indicated applied magnetic fields at  $I = 3 \mu\text{A}$ . The orientation of magnetic field was perpendicular to the graphene plane.

terized by a transition temperature  $T_C$ , shows dependence on the strength of applied magnetic field. The transition temperatures are  $T_C(0 \text{ T}) = 9 \text{ K}$ ,  $T_C(0.2 \text{ T}) = 8 \text{ K}$  and  $T_C(0.4 \text{ T}) = 7 \text{ K}$ .

The sensitivity of  $T_C$  to magnetic fields suggests a connection with superconductivity. Since graphene is a two dimensional (2D) crystal, it can be only 2D superconductivity because underlying SiC sample is a familiar wide band semiconductor, which is not known to manifest superconductivity. Superconductivity in 2D does not

lead to a fully coherent superconducting state below  $T_C$  like in 3D superconductors but to a fluctuating 2D superconductivity [63]. The real superconducting state in 2D appears at lower temperatures below the Berezinskii-Kosterlitz-Thouless (BKT) transition temperature  $T_{BKT}$  [64, 65]. Above  $T_{BKT}$ , the true superconductivity is destroyed by phase fluctuations due to the unbinding of thermally excited vortex-antivortex pairs, which lead to a finite resistivity [63–65]. Accordingly, the region below the drop of the resistance in graphene on SiC (figure 4.24) can represent the fluctuating 2D superconductivity characterized by  $T_C^{2D} = 9$  K. The real 2D superconducting state with a zero resistance can lie then below 4 K, i.e. below the temperature limit of our setup. In order to find  $T_{BKT}$  and determine whether this graphene/SiC sample is reaching the real superconducting state, another point probe setup capable of measurements at lower temperatures has to be used.

Several ideas have been proposed how to make graphene superconducting by doping in literature [66, 67]. Graphene on SiC(0001) is doped from the underlying SiC substrate by the means of disordered localized states of the interface layer. The mechanism of 2D fluctuating superconductivity in graphene is most probably based on the strong electron-phonon coupling between graphene electrons interacting with localized electron states formed at the SiC(0001) substrate/graphene interface and  $z$ -acoustic phonons of graphene. The strong electron-phonon coupling has been identified by inelastic electron tunneling spectroscopy in section 4.3.4. The inelastic electron tunneling contributions corresponding to the graphene phonon at 70 meV exhibited giant values  $\approx 50\%$  of the tunneling current in particular at the positions of the localized states of the underlying interface layer. The electron-phonon coupling is generally larger for more localized electron states [68]. This has been found in density-functional calculations on amorphous silicon, where localized states of defects or topological disorder exhibited an anomalously large electron-phonon coupling [68]. In superconductivity of graphite intercalated compounds [69], the electron-phonon coupling is expected to be the most likely responsible for the pairing mechanism, as recent studies suggested [54, 70, 71]. Similarly, the strong coupling between the "modified graphene electrons", due to the interaction with interface localized defect states, and the  $z$ -acoustic phonon mode of graphene could lead to superconductivity in graphene on SiC.

The unusual temperature dependence of resistance (4.23) and the V-shaped gap-like feature measured at 5 K on a graphene monolayer and bilayer (figure 4.7) can be indicative for a low temperature glass phase. An intermediate metallic glassy phase has been predicted to form a transition between the normal metal and insulator [72]. In many disordered electronic systems, electron-electron interactions and disorder are equally important and their competition often leads to glassy dynamics of elec-

#### 4. Graphene on silicon carbide

---

trons. A way of thinking can be the following as was described by Dobrosavljevic *et al.* [72] considering an extended Hubbard model of disordered electrons, where two routes to Anderson or Mott localization can occur. The Anderson route, which is the most probable in our case because of the large disorder, is from a Fermi-liquid via a metallic glass state to a Mott-Anderson glass [72]. Crossing the critical line from a Fermi-liquid to a metallic glass results in collective excitations of low energy charge rearrangements inside the glassy phase. At finite temperatures electrons undergo inelastic scattering from such collective excitations, leading to an unconventional resistivity versus temperature behavior. The gap-like feature can be described as an Efros-Shklovskii gap [72].

The appearance of gap-like features can have also another origin in pseudogap, as discussed for several layered compounds such as TaSe<sub>2</sub>, La<sub>1.2</sub>Sr<sub>1.8</sub>Mn<sub>2</sub>O<sub>7</sub> [73] and the lightly doped high- $T_C$  parent compounds [74]. The origin of the pseudogap is still under discussion, but there are more and more indications that electron correlation and disorder effects of the charge carriers are involved [73,74]. In the lightly doped high- $T_C$  parent materials, Kohsaka *et al.* [74] has shown that doping of a Mott-Hubbard (MH) system is radically different from a conventional semiconductor. The underdoped high- $T_C$  materials show a pseudogap with a strong asymmetry in the DOS outside the pseudogap region, which is an indication of the charge carrier correlation effects. A similar asymmetry with more pronounced DOS in the empty states is observed in the STS curves measured on graphene on SiC (see figure 4.7). The parent substrate for the growth of graphene, the SiC(0001) surface, is a two-dimensional Mott-Hubbard insulator. Photoemission and scanning tunneling data [75,76] support clearly a two-dimensional MH insulator with a bandgap of 2 eV for the 6H-SiC(0001) material surface. The surface bandgap of SiC(0001) is formed out of the Si- $p_z$  dangling bond orbitals, which do not form a metallic ground state with a half-filled narrow band, but a MH insulator due to Coulomb effects, as was shown by Anisimov *et al.* [76]. This system forms the substrate for growing single and multilayers of graphene by a heating procedure in ultra-high vacuum. However, it is not known whether the surface of SiC substrate remains a MH insulator upon a heat treatment that forms the carbon rich interface layer and graphene layers. Interestingly, Bostwick *et al.* [16] showed a small modification of the linear dispersion at 200 meV accompanied by a kink structure and described this to electron-phonon coupling but it could be caused by electron correlations as well. The additional photoemission broadening of the energy distribution curves due to self-energy effects between 0.2-0.5 eV below the Fermi-level can be a result of similar electron correlation effects.

Another curious observation is the "free-electron" scattering around a structural defect as is shown in figure 4.21. Bias-dependent topography plots show that the

energy dispersion in real space results in a linear  $E(k_{\parallel})$  dispersion curve by a Fourier transformation. However, the Dirac point has been shifted to positive bias voltages, +0.1 eV as is shown in figure 4.22. This is a very interesting observation, an electron-doped graphene layer with a Dirac point at -0.45 eV can locally be shifted to positive values. A possible explanation is that the charge density waves are disturbed locally by structural defects, thereby distorting the phase of the waves leading to a shift of the chemical potential locally. Free charge carriers in the disturbed potential area of the charge density wave can scatter from the potential associated by the structural defect forming Friedel oscillations. Also Artermenko *et al.* [77] explains that free carriers of opposite sign to the majority charge carriers will play an important role in local screening around impurity or defect sites (small metal islands) in glassy states of quasi one-dimensional systems at low temperature. This is an additional indication that the electronic behavior of a single graphene layer grown on SiC(0001) is completely different than an exfoliated graphene layer due to the strong interaction between the localized electron and hole states of the interface layer structure and the Dirac electrons of graphene.

## 4.4 Conclusions

The successful formation of few layer graphene on SiC(0001) has been performed by the heating procedure in ultra high vacuum. STM topography and STS measurements have shown that a single graphene layer grown on a SiC(0001) substrate is still affected by the electronic structure of the interface layer of SiC. The graphene monolayer has manifested transparency at bias voltages  $> 100$  mV in STM, by displaying localized states of the underlying interface layer in STM. The semiconducting carbon rich SiC(0001) substrate/graphene interface has a disordered structure with sharp localized electron states in the filled and empty states. The electronic structures of the first and second graphene layers studied by STS have revealed an unexpected gap-like feature located at the Fermi energy. This gap-like feature starts at  $\pm 70$  meV, which is the energy of the out of plane acoustic phonon of graphene. The appearance of the gap-like feature is probably due to charge modulations from graphene electrons interacting with localized interlayer electron states, indicating that electron correlation effects play an important role for the charge carrier behavior at the Fermi-level. Inelastic electron tunneling spectroscopy on the monolayer graphene has measured a gigantic inelastic phonon contribution for the out of plane acoustic phonon (70 meV) of graphene, reaching a 50% intensity of the IETS peaks. This inelastic contribution has been enhanced particularly on the places with localized electron states of the interface layer. Such a high inelastic tunneling contribution is an indication of a strong electron-

#### 4. Graphene on silicon carbide

---

phonon coupling. Temperature dependent resistance measurements on the few-layer graphene (1-3) on SiC(0001) have shown an unexpected behavior at low temperatures. A sharp drop in resistance has been observed at 9 K, which could be shifted to lower temperatures by applied external magnetic field. This drop of resistance has been attributed to a phase transition to a two-dimensional fluctuating superconductivity state. The pairing mechanism of superconductivity in graphene/SiC is most probably based on strong electron-phonon coupling between graphene electrons interacting with localized electron states formed at the SiC(0001) substrate/graphene interface and  $z$ -acoustic phonons of graphene.

### Bibliography

- [1] K. S. Novoselov, A. K. Geim, S. V. Morozov, D. Jiang, Y. Zhang, S. V. Dubonos, I. V. Grigorieva, and A. A. Firsov, *Science* **306**, 666 (2004).
- [2] K. S. Novoselov, A. K. Geim, S. V. Morozov, D. Jiang, M. I. Katsnelson, I. V. Grigorieva S. V. Dubonos, and A. A. Firsov, *Nature* **438**, 197 (2005).
- [3] C. Berger, Z. Song, T. Li, X. Li, X. Wu, N. Brown, C. Naud, D. Mayou, A. N. Marchenkov, E. H. Conrad, P. N. First, and W. A. de Heer, *Science* **312**, 1191 (2006).
- [4] M. I. Katsnelson and K. S. Novoselov, *Solid State Commun.* **143**, 3 (2007)
- [5] M. I. Katsnelson, K. S. Novoselov, and A. K. Geim, *Nature Phys.* **2**, 620 (2006).
- [6] A. V. Shytov, M. I. Katsnelson, and L. S. Levitov, *Phys. Rev. B* **99**, 246802 (2007).
- [7] N. M. R. Peres, A. H. Castro Neto, and F. Guinea, *Phys. Rev. B* **73**, 241403(R) (2006).
- [8] F. Miao, S. Wijeratne, Y. Zhang, U. C. Coskun, W. Bao, and C. N. Lau, *Science* **317**, 1530 (2007).
- [9] V. V. Cheianov, V. Fal'ko, and B. L. Altshuler, *Science* **315**, 1252 (2007).
- [10] S. V. Morozov, K. S. Novoselov, M. I. Katsnelson, F. Schedin, D. C. Elias, J. A. Jaszczak, and A. K. Geim, *Phys. Rev. Lett.* **100**, 016602 (2008).
- [11] T. Ando and T. Nakanishi, *J. Phys. Soc. Jpn.* **67**, 2857 (1998).
- [12] C. L. Kane and E. J. Mele, *Phys. Rev. Lett.* **95**, 226801 (2005).

- 
- [13] A. K. Geim and K. S. Novoselov, *Nature Materials* **6**, 183 (2007).
- [14] C. Berger, Z. Song, T. B. Li, X. Li, A.Y. Ogbazghi, R. Feng, Z. Dai, A. N. Marchenkov, E. H. Conrad, P. N. First, and W. A. de Heer, *J. Phys. Chem. B* **108**, 19912 (2004).
- [15] K. V. Emtsev, A. Bostwick, K. Horn, J. Jobst, G. L. Kellogg, L. Ley, J. L. Mcchesney, T. Ohta, S. A. Reshanov, E. Rotenberg, A. K. Schmid, D. Waldmann, H. B. Weber, and T. Seyller, (unpublished) arXiv:0808.1222 (2008).
- [16] A. Bostwick, T. Ohta, T. Seyller, K. Horn, and E. Rotenberg, *Nature Physics* **3**, 36 (2007).
- [17] S. Y. Zhou, G.-H. Gweon, A. V. Federov, P. N. First, W. A. de Heer, D.-H. Lee, F. Guinea, A. H. Castro Neto, and A. Lanzara, *Nature Materials* **6**, 770 (2007).
- [18] Y.-W. Tan, Y. Zhang, K. Bolotin, Y. Zhao, S. Adam, E. H. Hwang, S. Das Sarma, H. L. Stormer, and P. Kim, *Phys. Rev. Lett.* **99**, 246803 (2007).
- [19] J. H. A. Hagelaar, The role of the electron trajectory in scanning tunneling microscopy: elastic and inelastic tunneling through NO on Rh(111), Ph.D. thesis, Eindhoven University of Technology (2008).
- [20] M. A. van Hove, *Surf. Sci.* **49**, 181 (1975).
- [21] P. Martensson, F. Owman, and L. I. Johansson, *Phys. Stat. Sol. B* **202**, 501 (1997).
- [22] C. Riedl, U. Starke, J. Bernhardt, M. Franke, and K. Heinz, *Phys. Rev. B* **76**, 245406 (2007).
- [23] P. Lauffer, K. V. Emtsev, R. Graupner, Th. Seyller, L. Ley, S. A. Reshanov, and H. B. Weber, *Phys. Rev. B* **77**, 155426 (2008).
- [24] H. Yang, G. Baffou, A. J. Mayne, G. Comtet, G. Dujardin, and Y. Kuk, *Phys. Rev. B* **78**, 041408(R) (2008).
- [25] J.-C. Charlier, J.-P. Michenaud, X. Gonze, and J.-P. Vigneron, *Phys. Rev. B* **44**, 13237 (1991).
- [26] G. M. Rutter, J. N. Crain, N. P. Guisinger, T. Li, P. N. First, and J. A. Stroscio, *Science* **317**, 219 (2007).
- [27] L. Simon, C. Bena, F. Vonau, D. Aubel, H. Nasrallah, M. Habar, and J. C. Perruchetti, (unpublished) arXiv:0807.2813 (2008).

#### 4. Graphene on silicon carbide

---

- [28] H. A. Mizes and J. S. Foster, *Science* **244**, 559 (1989).
- [29] K. F. Kelly, D. Sarkar, G. D. Hale, S. J. Oldenburg, and N. J. Halas, *Science* **273**, 1371 (1996).
- [30] J. G. Kushmerick, K. F. Kelly, H.-P. Rust, N. J. Halas, and P. S. Weiss, *Phys. Chem. B* **103**, 1619 (1999).
- [31] T. O. Wehling, A. V. Balatsky, M. I. Katsnelson, A. I. Lichtenstein, K. Scharnberg, and R. Wiesendanger, *Phys. Rev. B* **75**, 125425 (2007).
- [32] G. M. Rutter, N. P. Guisinger, J. N. Crain, E. A. A. Jarvis, M. D. Stiles, T. Li, P. N. First, and J. A. Stroscio, *Phys. Rev. B* **76**, 235416 (2007).
- [33] K. V. Emtsev, F. Speck, Th. Seyller, and L. Ley, *Phys. Rev. B* **77**, 155303 (2008).
- [34] T. Ohta, A. Bostwick, J. L. McChesney, T. Seyller, K. Horn, and E. Rotenberg, *Phys. Rev. Lett.* **98**, 206802 (2007).
- [35] V. W. Brar, Y. Zhang, Y. Yayon, and T. Ohta, *Appl. Phys. Lett.* **91**, 122102 (2007).
- [36] T. Ohta, A. Bostwick, T. Seyller, K. Horn, and E. Rotenberg, *Science* **313**, 951 (2006).
- [37] Correspondence between: E. Rotenberg, A. Bostwick, T. Ohta, J. L. McChesney, T. Seyller, and K. Horn; and S.Y. Zhou, D.A. Siegel, A.V. Fedorov, F. El Gabaly, A. K. Schmid, A.H. Castro Neto, D.-H. Lee, and A. Lanzara, *Nature Materials* **7**, 258 (2008).
- [38] F. Varchon, R. Feng, J. Hass, X. Li, B. Ngoc Nguyen, C. Naud, P. Mallet, J.-Y. Veuillen, C. Berger, E. H. Conrad, and L. Magau, *Phys. Rev. Lett.* **99**, 126805 (2007).
- [39] A. Mattausch and O. Pankratov, *Phys. Rev. Lett.* **99**, 076802 (2007).
- [40] Private communication with Thomas Seyller.
- [41] I. Forbeaux, J.-M. Themlin, J.-M. Debever, *Phys. Rev. B* **58**, 16396 (1998).
- [42] Y. Zhang, V. W. Brar, F. Wang, C. Girit, Y. Yayon, M. Panlasigui, A. Zettl, and M. F. Crommie, *Nature Physics* **4**, 627 (2008).
- [43] T. O. Wehling, I. Grigorenko, A. I. Lichtenstein, and A. V. Balatsky, *Phys. Rev. Lett.* **101**, 216803 (2008).

- [44] M. Galperin, M. A. Ratner, and A. Nitzan, *J. Chem. Phys.* **121**, 11965 (2004).
- [45] L. Vitali, M. A. Schneider, K. Kern, L. Wirtz, and A. Rubio, *Phys. Rev. B* **69**, 121414(R) (2004).
- [46] B. C. Stipe, M. A. Rezaei, and W. Ho, *Science* **280**, 1732 (1998).
- [47] J. Jiang, R. Saito, Ge. G. Samsonidze, S. G. Chou, A. Jorio, G. Dresselhaus, and M. S. Dresselhaus, *Phys. Rev. B* **72**, 235408 (2005).
- [48] K. Sugawara, T. Sato, S. Souma, T. Takahashi, and H. Suematsu, *Phys. Rev. B* **73**, 045124 (2006).
- [49] R. Landauer, *Philos. Mag.* **21**, 863(1970).
- [50] E. Rossen, Influence of substrate and tip on inelastic electron tunneling spectroscopy, M.Sc. thesis, Eindhoven University of Technology (2007).
- [51] R. H. M. Smit, Y. Noat, C. Untiedt, N. D. Lang, M. C. van Hemert and J. M. van Ruitenbeek, *Nature* 419, 906 (2002).
- [52] J. L. McChesney, A. Bostwick, T. Ohta, K. Emtsev, T. Seyller, K. Horn, and E. Rotenberg, (unpublished) arxiv:0809.4046 (2008).
- [53] J. L. McChesney, A. Bostwick, T. Ohta, K. Emtsev, T. Seyller, K. Horn, and E. Rotenberg, (unpublished) arxiv:0705.3264 (2008).
- [54] T. Valla, J. Camacho, Z-H. Pan, A. V. Fedorov, A. C. Walters, C. A. Howard, and M. Ellerby, (unpublished) arXiv:0803.0254 (2008).
- [55] M. F. Crommie, C. P. Lutz, and D. M. Eigler, *Nature* **363**, 524 (1993).
- [56] S. Rouzière, S. Ravy, J.-P. Pouget, and S. Brazovskii, *Phys. Rev. B* **62**, R16231 (2000).
- [57] J. Červenka, C. F. J. Flipse, *J. Phys.: Conf. Ser.* **61**, 190 (2007).
- [58] N. M. R. Peres, F. Guinea, and A. H. C. Neto, *Phys. Rev. B* **73**, 125411 (2006).
- [59] M. Morgenstern, J. Klijn, Chr. Meyer, M. Getzlaff, R. Adelung, R. A. Römer, K. Rosnagel, L. Kipp, M. Skibowski, and R. Wiesendanger, *Phys. Rev. Lett.* **89**, 136806 (2002).
- [60] K. Fossheim, *Superconductivity: physics and applications*, Chichester: Wiley, Sudbo Asle, 2004.



#### 4. Graphene on silicon carbide

---

- [61] L. J. van der Pauw, *Philips Research Reports* **13**, 1 (1958).
- [62] Z. Wang, F. Xu, C. Lu, H. Zhang, Q. Xu, J. Zhu, (unpublished) arXiv:0801.3298 (2008).
- [63] Q. Li, M. Hücker, D. D. Gu, A. M. Tsvelik, and J. M. Tranquada, *Phys. Rev. Lett.* **99**, 067001 (2007).
- [64] V. L. Berezinskii, *Zh. Eksp. Teor. Fiz.* **61**, 1144 (1971); *Sov. Phys. JETP* **34**, 610 (1972).
- [65] J. M. Kosterlitz and D. J. Thouless, *J. Phys. C* **6**, 1181 (1973).
- [66] B. Uchoa and A. H. Castro Neto, *Phys. Rev. Lett.* **98**, 146801 (2007).
- [67] T. C. Choy and B. A. McKinnon, *Phys. Rev. B* **52**, 14539 (1995).
- [68] R. Atta-Fynn, P. Biswas, and D. A. Drabold, *Phys. Rev. B* **69**, 245204 (2004).
- [69] M. S. Dresselhaus and G. Dresselhaus, *Adv. Phys.* **51**, 1 (2002).
- [70] G. Lamura, M. Aurino, G. Cifariello, E. Di Gennaro, A. Andreone, N. Emery, C. Hérold, J.-F. Marêché, and P. Lagrange, *Phys. Rev. Lett.* **96**, 107008 (2006).
- [71] G. Csányi, P. B. Littlewood, A. H. Nevidomskyy, C. J. Pickard, and B. D. Simons, *Nature Phys.* **1**, 42 (2005).
- [72] V. Dobrosavljević, D. Tanasković, and A. A. Pastor, *Phys. Rev. Lett.* **90**, 016402 (2003).
- [73] B. Kyung, S. S. Kancharla, D. Senechal, A.-M. S. Tremblay, M. Civelli, G. Kotliar, *Phys. Rev. B* **73**, 165114 (2006).
- [74] L. Bartosch, P. Kopietz, *Eur. Phys. J. B* **28**, 29 (2002).
- [75] V. Ramachandran and R. M. Feenstra, *Phys. Rev. Lett.* **82**, 1000 (1999).
- [76] V. I. Anisimov, A. E. Bedin, M. A. Korotin, G. Santoro, S. Scandolo, and E. Tosatti, *Phys. Rev. B* **61**, 1752 (2000).
- [77] Artermenko, *JETP Lett.* **61**, 779 (1995).

## Chapter 5

# Wet deposition of fullerenes

### 5.1 Introduction

Since the discovery of  $C_{60}$  [1], many studies have been performed in order to understand the basic properties of this complex molecule and to develop possible applications [2–4]. Many of these possible applications will require deposition of  $C_{60}$  films onto surfaces. Therefore, the initial nucleation and growth of fullerene films have been investigated on a variety of surfaces [4]. So far the preparation of fullerene films has been successfully performed mainly by a thermal evaporation in ultra high vacuum (UHV) [5–10] or inert gas atmosphere [11]. Unfortunately, the majority of fullerene derivatives cannot be deposited by thermal evaporation because they undergo a thermal decomposition. These molecules exhibit a variety of physical properties that cannot be found in pure fullerenes. For this reason, an alternative technique for deposition of very thin films is needed.

The  $C_{60}$  molecule is the most common fullerene which has been used as a basic component in a variety of new carbon nanostructures including:  $C_{60}$  dimers [12], polymers [13], endohedral fullerenes [14, 15], peapod nanotubes [16] and single-molecule transistors [17]. In addition to the flexibility as nanostructural building blocks, fullerene systems can also be electronically tuned from semiconducting, metallic to superconducting properties via charge doping [18, 19]. The superconductivity in alkali-doped fullerides has been observed at temperatures as high as at the best conventional superconductors: 19 K for  $K_3C_{60}$ , 30 K for  $Rb_3C_{60}$ , and up to 33 K for  $RbCs_2C_{60}$  [20]. Similarly fullerenes complexes can be made magnetic via addition of different atoms or molecules. Recently discovered endohedral fullerenes  $N@C_{60}$  [14] and  $P@C_{60}$  [15] are such examples. Endohedral fullerenes are the novel forms of the fullerene-based materials in which an atom (N, P) is implanted into the hollow fullerene cage. Experimentally electron spin resonance (ESR) studies [14, 15] revealed that endohedral

## 5. Wet deposition of fullerenes

---

nitrogen and phosphorous in  $C_{60}$  sit in the center of the cage and remain atomic due to the quartet electronic spin states observed. The electron spin of these endohedrals has a remarkably long lifetime that makes it a useful embodiment of a qubit for electron spin quantum computation [21–23]. However,  $N@C_{60}$  and  $P@C_{60}$  cannot be thermally evaporated at  $T = 500 - 600^\circ\text{C}$  due to the insufficient thermal stability of the endohedral atom [24].

In this chapter, a new wet deposition technique for production of very thin fullerene films is presented. This technique can be applied to any fullerene which cannot be thermally evaporated but can be dissolved in toluene or carbon disulfide ( $CS_2$ ). It uses a special nebulizer to spray coat a fullerene solution onto a sample surface under ambient conditions. This technique has been successfully applied on graphite and gold surfaces on which  $C_{60}$  has been widely studied by different surface techniques before [5–10, 25–27]. The resulting morphology of layers formed at the interface of a thin solution film and a graphite surface have been investigated with atomic force microscopy (AFM) as a function of a sprayer-sample distance and a solution concentration in section 5.3.1. Different morphologies of the film have been observed depending on the deposition parameters. In section 5.3.2, molecular thick  $C_{60}$  films have been spray coated on Au(111). These  $C_{60}$  films have been studied by scanning tunneling microscopy and spectroscopy and compared to evaporated  $C_{60}$  on Au(111).

## 5.2 Experimental

The deposition of fullerenes was performed in air at room temperature. A commercially available Meinhard nebulizer TR-30-K1 [29] connected to the argon gas supply was used for spray coating. The nebulizer was kept at a certain small angle in respect to the vertical position during spray coating to avoid landing of big droplets onto the graphite surface.  $C_{60}$  solutions were prepared by dissolving of 99.5% pure solid  $C_{60}$  powder in  $CS_2$  or toluene to the desired concentration. Only about few microliters of a fullerene solution have been needed for the formation of one monolayer on sample surfaces. HOPG samples were cleaved with an adhesive tape before each deposition. The Au(111) surface has been prepared by flame annealing of 100 nm thick Au films on mica in air. MultiMode Scanning Probe Microscope with the Nanoscope IV controller from Veeco Instruments was employed for AFM measurements in the tapping mode in air. Scanning tunneling microscopy has been measured in an Omicron GmbH LT-STM setup working under UHV conditions ( $10^{-11}$  mbar). For this purpose, the freshly spray coated  $C_{60}$  films on Au(111) have been transferred directly to UHV STM setup in order to avoid oxidation in air. The  $C_{60}/\text{Au}(111)$  sample has been heated to  $150^\circ\text{C}$  in UHV for 1 hour in order to remove water and other organic contaminants

before STM experiments. STM measurements were performed at 78 K and 4 K in the constant current mode with mechanically formed Pt/Ir tips. STS spectra have been obtained by using a lock-in amplifier technique.

## 5.3 Results and discussions

### 5.3.1 Spray coating of $C_{60}$ in solution

For a successful formation of very thin fullerene films by spray coating, one needs to produce very fine droplets from a solution in order to homogeneously disperse a very small amount of a liquid sample over a surface. A commercially available Meinhard nebulizer TR-30-K1 has been purchased for this purpose. This nebulizer can produce uniform 10 to 20  $\mu\text{m}$  droplets with aqueous solutions according to the producer [29]. For toluene or  $\text{CS}_2$  solutions, the size of droplets is expected to be smaller because of their smaller density, surface tension and viscosity in comparison to water. A schema of the Meinhard nebulizer is shown in figure 5.1. The principle of this nebulizer is based on a flow of a carrier gas (Ar or  $\text{N}_2$ ), which causes a suction in the capillary containing a sample solution. Thus, a sample is pushed out from the capillary to the nozzle where it is dispersed into small droplets. For spray coating of fullerenes, the nebulizer was positioned in a vertical position above the sample. The graphite and Au(111) substrates have been chosen for their known inertness, cleanness and atomic flatness and because  $C_{60}$  has been studied extensively on these substrates by different techniques including STM and STS [5–10, 25–27].

The nebulizer-sample distance has been found as the main parameters for spray coating of fullerenes in solution. By changing the distance of the nebulizer from a sample, the surface wetting can be controlled. The surface wetting has a direct effect on the thickness of a  $C_{60}$  layer formed on a surface. Table 5.1 shows the influence of the nebulizer-sample distance on the film morphology on graphite for two

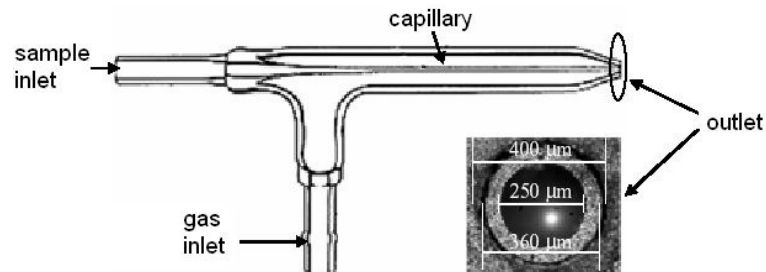


**Figure 5.1:** Schematic picture of the Meinhard nebulizer TR-30-K1.

## 5. Wet deposition of fullerenes

---

**Table 5.1:** Fullerene films morphologies on HOPG as observed by AFM for different spraying distances  $D$  of the nebulizer towards sample surface. The  $C_{60}$  concentration were  $C_{CS_2} = 1.42$  g/l and  $C_{toluene} = 0.57$  g/l.

$D_{CS_2}$ (cm)	$D_{toluene}$ (cm)	Film character (film height)
0-5	0-10	"3-D film" - high clusters (10 - 100 nm)
7-11	15-20	"2-D film" - low clusters (1 - 5 nm)
> 14	> 25	Solitary clusters (10 - 50 nm)

solvents. Spray coated  $C_{60}$  films on graphite surfaces have been studied by AFM. The dependence on the distance can be principally divided into three cases for both solvents at the fixed solution concentration. For small distances, a substrate surface was visibly wetted with a solution similarly like in drop coating. The drop coating of fullerenes is known to produce big clusters with a height up to few hundred nanometers on graphite surfaces [30]. Since fullerenes are free to move in both solvents [31],  $C_{60}$  molecules could diffuse and aggregate in large clusters while the solution was present on graphite surface till the solvent fully evaporated. When the distance between the nebulizer and sample was too large, large solitary clusters have been found on a surface. The solvent in the droplets evaporated totally during the time of flight to the surface, so only solitary clusters have been found on a surface. Usually one such a solitary cluster was found in an area of  $5 \times 5 \mu\text{m}$ . From the volume of the cluster and the concentration of the solution, the size of the incident droplet has been determined to be in the order of few micrometers.

The optimal nebulizer-sample distance for the ultrathin film formation has been established to be 7 – 11 cm for  $CS_2$  and 15 – 20 cm for toluene solutions. Shorter spraying distances have been found for  $CS_2$  than for toluene because  $CS_2$  has a faster evaporation rate. All spray coated fullerene films exhibited an island like structure on HOPG surfaces showing small flat clusters with a maximum height 5 nm. In figure 5.2, two AFM images of such flat fullerene clusters on graphite are shown. Fullerenes can be recognized on the graphite surface by a dark contrast in comparison to graphite in the AFM phase image (figures 5.2b and 5.2d). The phase angle of probe oscillation in tapping mode AFM is sensitive to the dissipation energy between tip and surface. Different material properties as viscoelasticity, friction, adhesion, hardness and others are hidden in the dissipation energy [32, 33]. Therefore phase imaging is a powerful technique for distinguishing different surface compounds, which cannot be seen from topography image. The fullerene clusters in figure 5.2 demonstrate predominantly a monolayer height as can be seen in the line profile across one of the clusters. This result of the step height of the fullerene clusters is in good agreement with the STM results on  $C_{60}$  films on HOPG prepared by thermal evaporation in UHV [10], where

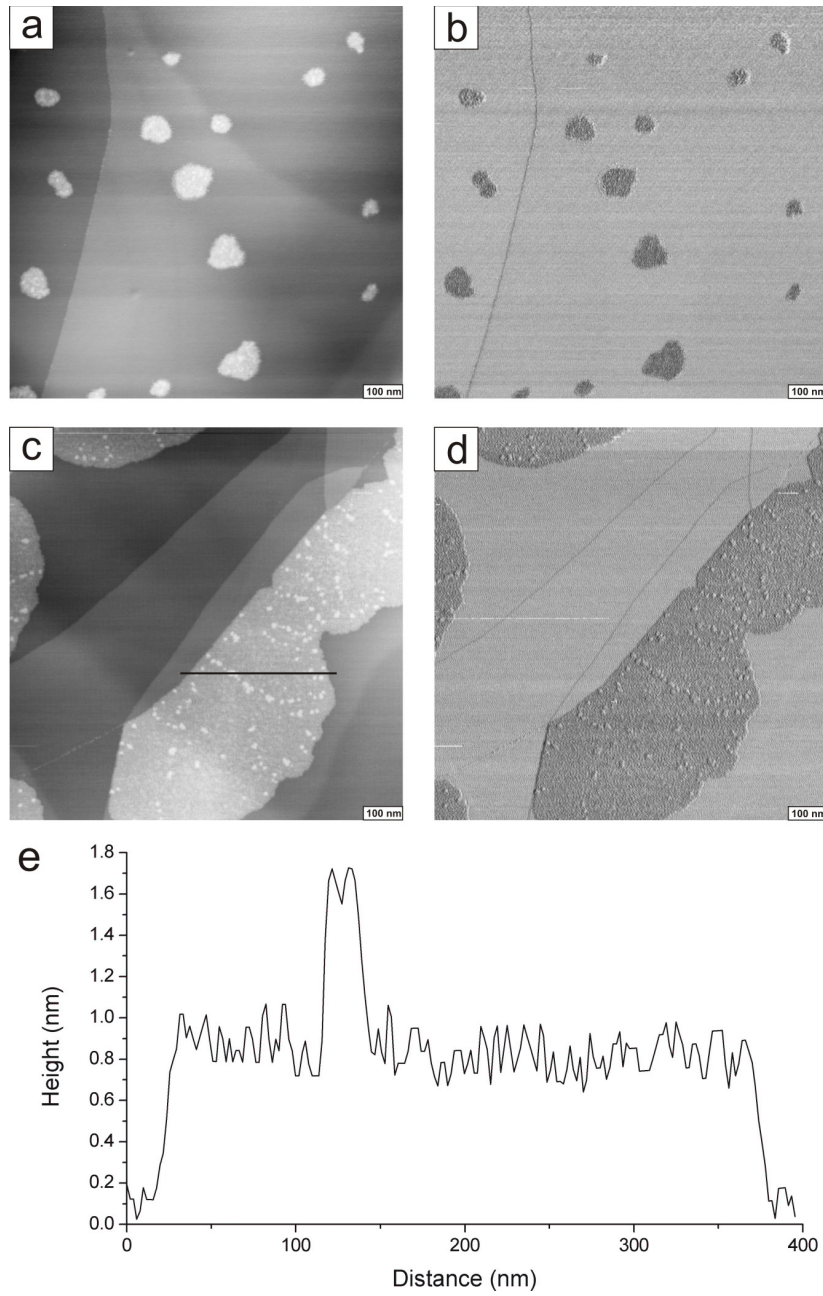


**Figure 5.2:** AFM images of spray-coated fullerene clusters on a  $1 \times 1 \mu\text{m}$  area on HOPG: (a) and (c) topography images, (b) and (d) phase images, and (e) a line profile along the black line across the cluster in figure (c).

## 5. Wet deposition of fullerenes

---

the first  $C_{60}$  layer have shown 1.05 nm height and the height of next layers was 0.85 nm. These values also agree well with simulation results using the Girifalco potential for the  $C_{60}$ - $C_{60}$  interaction and the Ruoff-Hickmann potential for the  $C_{60}$ -HOPG interaction [34]. The thickness of the second  $C_{60}$  layer is smaller than the first layer because  $C_{60}$  molecules in the second layer reside in the valleys created between  $C_{60}$  molecules of the first layer.

The concentration of fullerene solution should have also influence on the fullerene film formation since it is related to the number of fullerenes in the atomized solution droplets. However, the used concentrations 0.15 – 2 g/l have not lead to qualitative modification of the film morphologies for both toluene and  $CS_2$  solutions. The only noticed effect was at lower concentrations where a smaller density and lateral size of clusters have been observed. The nebulizer-sample distance has served as a better way to control the concentration of fullerenes in dispersed droplets because of the fast evaporation rate of both solvents.

Thus the mechanism of the film formation prepared by a spray coating is related to the ultra-thin film of the solution formed on the surface. The solution film wets the macroscopic area of the surface, upon which the material diluted in the solution forms a film during dewetting and drying process at the solution-sample interface. This process can be principally considered as "crystallization" [35]. In spray coating, the control over the wetting of the surface is mediated by controlling the nebulizer-sample distance, which has a direct influence on the film morphology. The successful formation of the ultrathin films is based on the certain distance at which droplets at the moment of the landing onto the surface contain still some solvent, which allows spreading of the fullerenes but the solvent evaporates so rapidly that  $C_{60}$ 's do not have time to aggregate in higher clusters. This idea is confirmed by that clusters are spread on the terraces as well as at step edges of HOPG (see figure 5.2a). It was shown that increased mobility of  $C_{60}$  in UHV resulted in the formation of clusters near the step-edges [9], however, we have not observed such preferential locations of fullerene clusters.

### 5.3.2 $C_{60}$ on Au(111)

Fullerenes have been spray coated on gold surface in the same way as on graphite as described in previous section. A clean Au(111) surface prepared by flame annealing is shown by AFM and STM in figure 5.3. Few hundred nanometer atomically flat terraces have been produced by this way as can be seen in AFM. The well known stripy Au(111) surface reconstruction in STM gives a clear evidence about the cleanness of this surface [36,37]. Figure 5.3d shows the gold surface after deposition of fullerenes. A vertical line observed on the right side of this image belong to a series of clusters

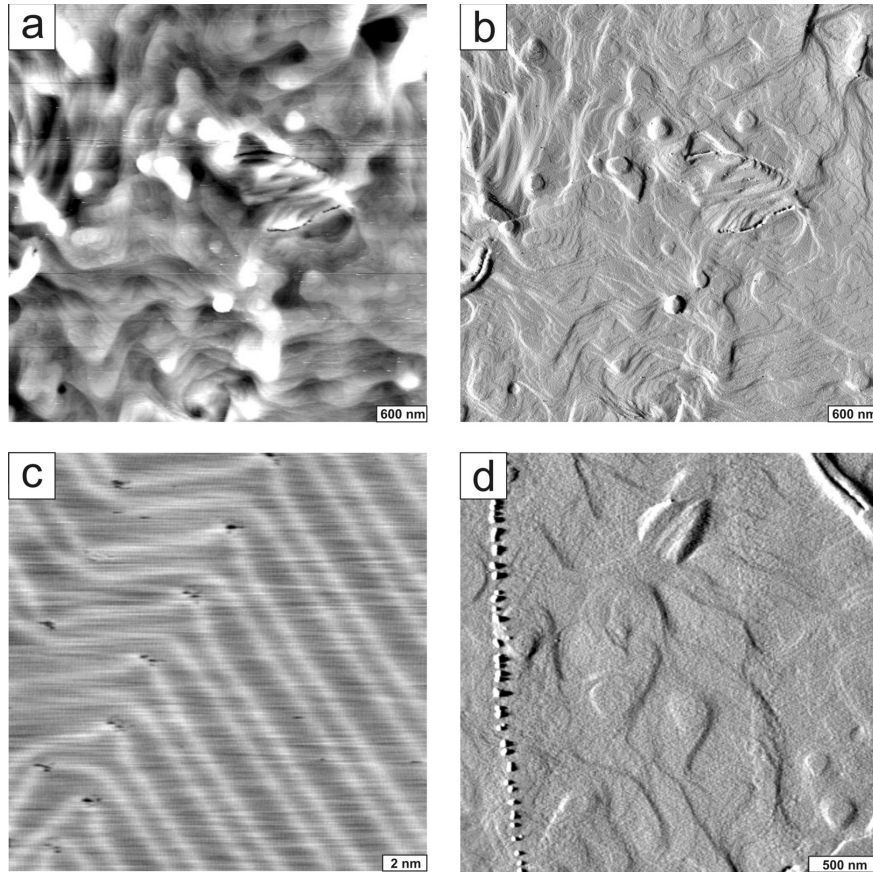


**Figure 5.3:** A clean Au(111) surface imaged by AFM height (a), AFM amplitude (b) and by STM (c). (d) An amplitude AFM image of spray coated  $C_{60}$  in  $CS_2$  on a Au(111) surface.

formed at the perimeter of a fullerene droplet due to a "coffee stain" effect [38]. Fullerene clusters inside of the droplet perimeter can be hardly seen in AFM image because of their small height although the amplitude AFM image has been used for better contrast.

STM images of molecularly resolved  $C_{60}$  clusters on Au(111) are demonstrated in figure 5.4. One monolayer clusters of  $C_{60}$  are organized in the hexagonal closed packed arrangement with the lattice parameter  $d = 1.05 \pm 0.05$  nm. In thermally evaporated  $C_{60}$  clusters, the intermolecular distance was found 1.002 nm [27].  $C_{60}$  molecules are seen as spheres at 78 K due to the free rotation of molecules around its axis. Numerous defects in the crystallographic structure of the ordered fullerene clusters are observed in STM. Clusters with no translation order have been observed



## 5. Wet deposition of fullerenes

---

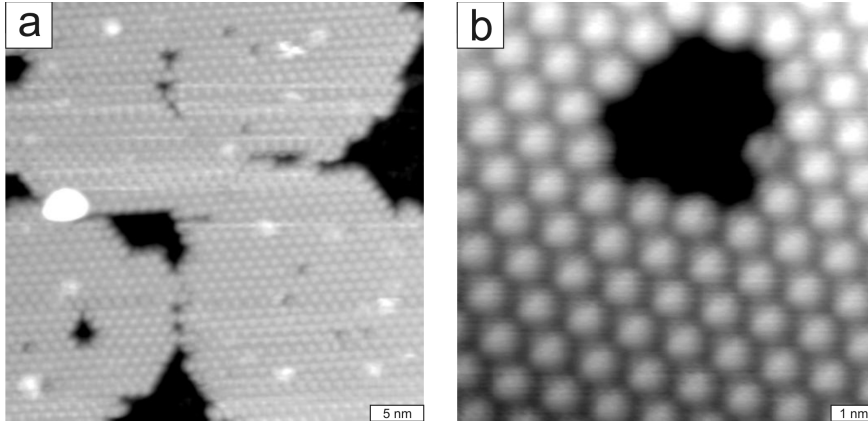


**Figure 5.4:** STM images of  $C_{60}$  spray coated on Au(111) measured with  $U = 2.2$  V and  $I = 5$  pA at 78 K.  $C_{60}$  clusters are arranged in close packed hexagonal arrangement with lattice parameter  $d = 1.05 \pm 0.05$  nm.

on the surface as well but with a much lower occurrence. Our results show that the spray-coated  $C_{60}$  on Au(111) shows comparable results in comparison to a thermally evaporated  $C_{60}$  on the nanometer scale [25]. In order to get larger ordered clusters a heat treatment would have to be applied similarly like for thermally evaporated  $C_{60}$ .

When the temperature is lowered to 4 K, the molecular rotations of  $C_{60}$  freeze-up, and the molecular orientation can be determined. In figure 5.5, high resolution STM images of  $C_{60}$  molecules on Au(111) at 4 K are shown.  $C_{60}$  molecules exhibit a characteristic intramolecular structure composed of lobes [26]. An orientational order is observed inside the clusters, whereas diverse orientations of  $C_{60}$  molecules are occurring at the edges of clusters. The orientation order in clusters is achieved due to a homogeneous mutual interaction between  $C_{60}$  molecules, which is broken at the edges. This fact is indicative of a very weak interaction between  $C_{60}$  and Au(111) because the  $C_{60}$ - $C_{60}$  interaction is known to be weak van der Waals [4]. The internal structure of the molecule shows dependence on the applied bias voltage as can be seen from the difference between two upper STM images imaged with positive bias voltage (figures 5.5a,b) and negative bias voltage (figures 5.5c,d). This is because STM probes different molecular orbitals of the molecule at different voltage [26]. In the empty states (positive bias voltage), the structures resemble the shape of the LUMO constant-DOS isosurfaces, as revealed by density functional calculations for a free  $C_{60}$  molecule [39]. The lobes represent the accumulation of DOS around the pentagonal faces of the icosahedral cage. In the filled states (negative bias voltage), the HOMO resonances are imaged with STM [26]. Thus, from the knowledge of the molecular orbitals at the particular energy, the exact orientation of molecule can be

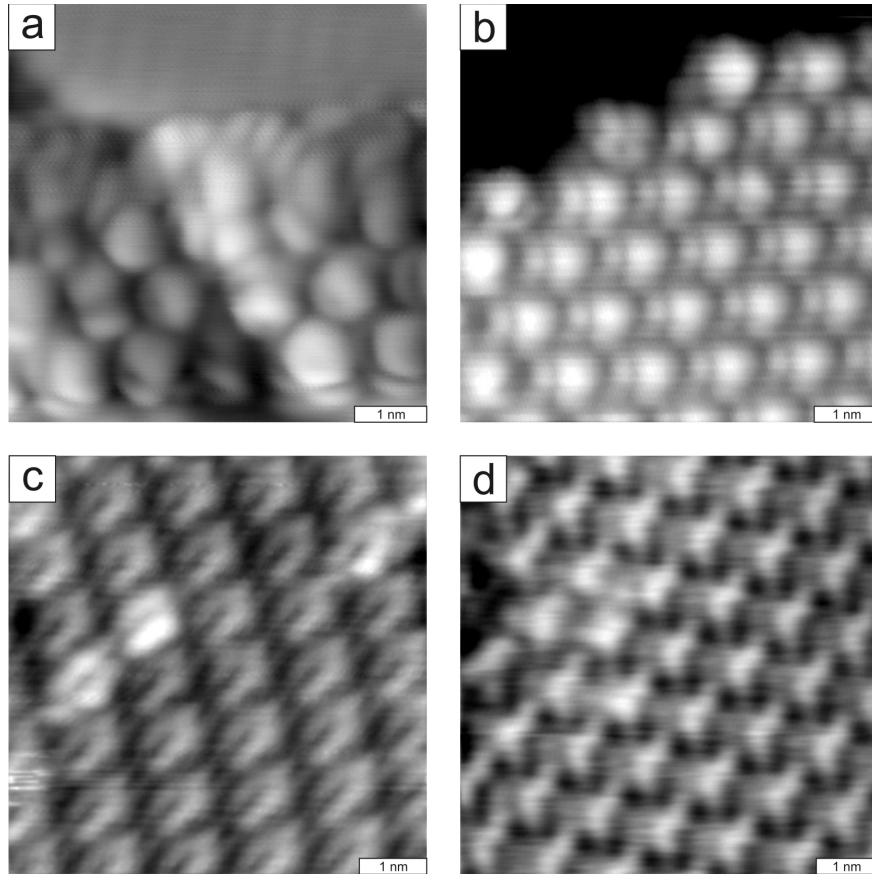


**Figure 5.5:** High resolution STM images of  $C_{60}$  spray coated on Au(111) showing internal structures of  $C_{60}$  molecules. The STM images have been imaged at (a)  $U = 2.2$  V,  $I = 5$  pA, (b)  $U = 2.53$  V,  $I = 85$  pA, (c)  $U = -2.0$  V,  $I = 130$  pA, and (d)  $U = -2.0$  V,  $I = 5$  pA.

determined. For more information about this topic the reader is referred to [26, 39].

The local electronic structure of  $C_{60}$  adsorbates have been measured via differential conductance  $dI/dV$  spectroscopy. Figure 5.6 shows typical  $dI/dV$  spectra obtained on top of a single  $C_{60}$  molecule adsorbed in the first and second  $C_{60}$  layer on the Au(111) surface. Three main resonance peaks are observed in the  $\pm 3$  V energy range in both  $C_{60}$  layers. The amplitude of these peaks has varied strongly over the surface of a single molecule similarly like in STS measurements of evaporated  $C_{60}$  on Au(111) [26]. The resonance peaks of a single  $C_{60}$  are centered at -1.8 V (HOMO), 0.7 V (LUMO), and 2 V (LUMO+1) in the first  $C_{60}$  layer. Two  $dI/dV$  spectra from the second  $C_{60}$  layer are shown in figure 5.6. They have been taken on two different positions of the

## 5. Wet deposition of fullerenes

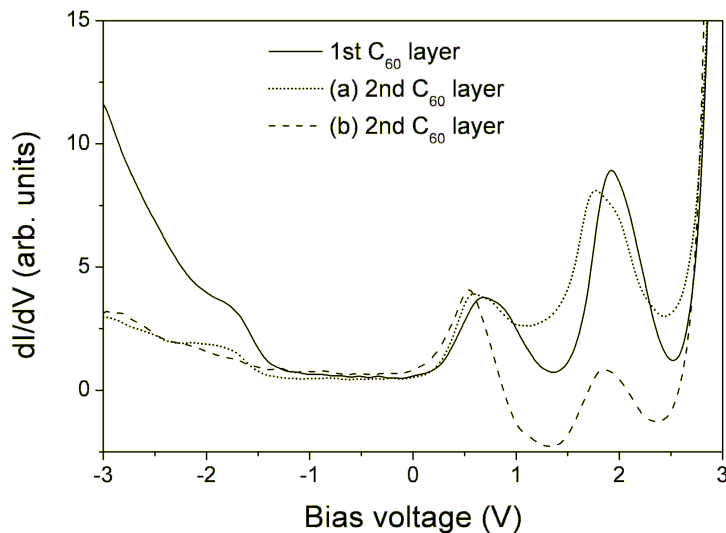


**Figure 5.6:**  $dI/dV$  spectra of a single  $C_{60}$  molecule in a cluster on Au(111) at  $T = 4$  K. The STS spectra were taken on the first and second  $C_{60}$  layer for comparison. Two  $dI/dV$  curves are shown for the second  $C_{60}$  layer, which were measured on the same molecule but at different positions. One depicts an normal  $dI/dV$  curve (a), while the second one exhibits negative differential conductance (b). Tunneling parameters were  $U = 2.2$  V and  $I = 10$  pA.

same  $C_{60}$ . Both  $dI/dV$  curves show approximately the energy positions of the  $C_{60}$  resonances at -1.8 V (HOMO), 0.6 V (LUMO), and 1.8 V (LUMO+1) in the second layer.

Fullerene adsorption on Au(111) surfaces has been extensively studied during recent years [26–28]. In the STM study of thermally evaporated  $C_{60}$  on Au(111), a slightly larger band gap (HOMO-LUMO) of 2.7 eV have been observed [26], in comparison to 2.5 eV in our case. The resonances were positioned at -1.7 V (HOMO), 1.0 V (LUMO), and 2.2 V (LUMO+1) [26]. Although  $C_{60}$  exhibits a 1.0 eV larger band gap than in the gas phase [40], it has been shown by a combination of STS and density functional calculations that the charge transfer between  $C_{60}$  and Au(111) is fairly small [26]. Photoelectron spectroscopy study of  $C_{60}$  on Au has indicated that there is a subtle interplay between several interacting and opposing effects, which results in a interfacial dipole to be directed from the adsorbent to the metal [28]. It is known that the electron distribution at the Au surface extends rather far into the vacuum [28], therefore this interfacial dipole can be associated with the rearrangement of the metal electronic tails due to the overlap with the adsorbed organic molecules. Since the LUMO resonance of  $C_{60}$  layer on the Au(111) surface lies far from the Fermi level, small changes in its alignment does not alter significantly the charge state of

the fullerene, therefore the level shifts are entirely due to screening effects from the underlying metal surface [26]. Accordingly, the small difference between the band gaps in the first (2.5 eV) and second  $C_{60}$  layer (2.4 eV) can be attributed to the increased distance from the gold surface and consequently to reduced screening.

Interestingly, the second  $dI/dV$  curve measured on a  $C_{60}$  molecule in the second layer goes through negative values for  $U > 0.9$  V in figure 5.6. This effect is called negative differential resistance (NDR) in literature. NDR is characterized by the phenomenon of decreasing current with increasing voltage in  $I(V)$  curves and is used in several important electronic components [41, 42]. Recently, it has been observed in quantum dots [43, 44] and in STM studies of molecules with narrow resonance electron states, including  $C_{60}$  [45, 46]. The observation of NDR has been reported on a  $C_{60}$  bilayer on Au(111) prepared by thermal evaporation in UHV [46]. An increase in NDR has been observed with a larger tip-sample separation and increasing bias voltage similarly like in figure 5.6. The principle of NDR in  $C_{60}$  is based on the tunneling into a narrow resonance peaks and a voltage-dependent increase in the tunneling barrier height [46]. However, the NDR effect is absent on a monolayer  $C_{60}$  on Au(111). This is because  $C_{60}$  monolayer has an increased interaction in comparison with the Au(111) substrate, which broadens the width of the  $C_{60}$  resonance and adds a constant metallic density of states background to the monolayer electronic structure. Conduction through such a metallic continuum overpowers the current drop due to a voltage-dependent barrier and prevents NDR from emerging [46]. This could also

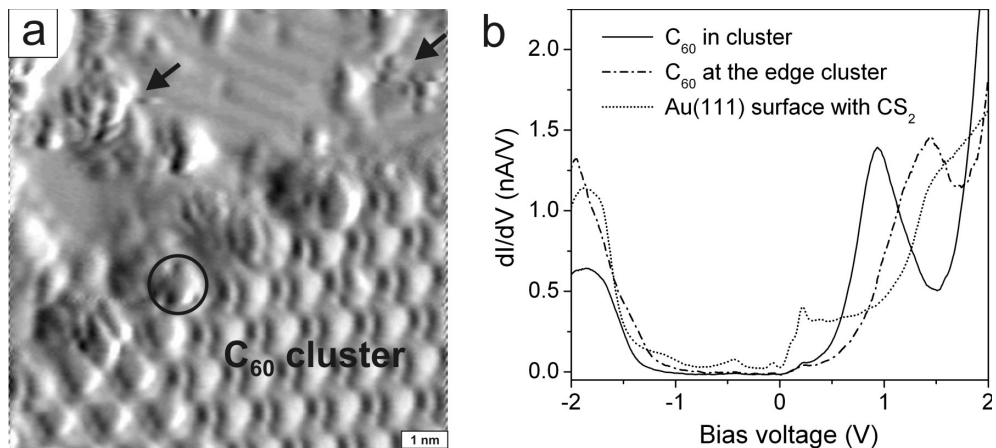


**Figure 5.7:** (a) A current STM image of a  $CS_2$  residues next to a  $C_{60}$  cluster on the Au(111) surface. (b)  $dI/dV$  spectra taken on a  $CS_2$  contamination,  $C_{60}$  at the edge of the cluster and inside of the ordered cluster. The arrows indicate the positions, where the  $dI/dV$  spectra were taken on  $CS_2$  residues. The circle marks out the measured  $C_{60}$  molecule at the edge of the cluster.

## 5. Wet deposition of fullerenes

---

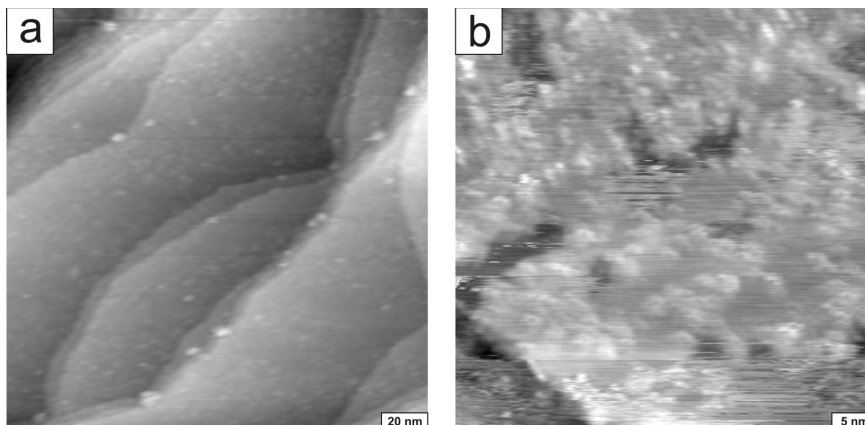


**Figure 5.8:** STM images of toluene residues on a Au(111) surface. The gold surface was spray coated by pure toluene in air.

explain, why NDR is not observed on certain positions of  $C_{60}$  in the second layer in figure 5.6. Most probably those are positions on the molecule, where is a lower DOS of a LUMO molecular orbital (see figure 5.5).

So far it seems to be that spray coating of fullerenes leads to similar results compared to thermal evaporation. However, solvent residues have been found to be attached to the gold surface after spray coating of fullerene solutions. The solvent has not evaporated totally as expected but remained attached to the gold surface. In figure 5.7,  $CS_2$  residues on the gold surface next to the  $C_{60}$  cluster are shown. Since  $CS_2$  molecules demonstrated only 1.5 Å height in STM in comparison to 1 nm high  $C_{60}$ , a current STM image has been shown. The local electronic structure of  $CS_2$  residues measured by STS (5.7b) shows a peak at 0.2 V. The small peak at -0.5 V is related to the surface state of Au(111) [36]. However, the electronic structure of the  $C_{60}$  molecules seems not to be affected. Even the  $C_{60}$  molecules at the edge of the cluster do not show signs of the  $CS_2$  states. The LUMO resonance of the  $C_{60}$  molecule at the edge of the cluster is located at the energy 1.4 eV, similarly like a free standing  $C_{60}$  molecule on Au(111) [47].

Solvent contamination remained attached to the gold surface also in the case of toluene. A STM image of a toluene spray-coated Au(111) surface is shown in figure 5.8. Toluene covers whole gold surface. The solution contamination could not be removed even when the sample was heated to 250°C for 2 hours. For this reason a solvent contamination will be always present on gold surfaces, nevertheless, its influence on the electronic properties of fullerenes is negligible for  $CS_2$  as shown in figure 5.7. However, this influence has not been studied for toluene.

## 5.4 Conclusions

A new wet deposition technique for production of very thin fullerene films was successfully developed. This technique could be especially useful for fullerene derivatives, which cannot sustain high temperatures to be evaporated in UHV. Our alternative deposition technique can be applied to fullerenes dissolved in toluene or carbon disulfide. It uses a special nebulizer to spray coat fullerene solution onto a sample surface under ambient conditions. Spray coating of C<sub>60</sub> has been studied on graphite and gold surfaces. Monolayer thick C<sub>60</sub> films have been formed on both surfaces at particular deposition parameters as confirmed by AFM and STM. The structural and electronic properties of spray coated C<sub>60</sub> films on Au(111) have been shown comparable results to thermally evaporated C<sub>60</sub>. However, solvent residues remained attached to the gold surface and could not be removed.

## Bibliography

- [1] H. W. Kroto, J. R. Heath, S. C. O'Brien, R. F. Curl and R. E. Smalley, *Nature* **318**, 162 (1985).
- [2] W. Krätschmer, L. D. Lamb, K. Fostiropoulos and D. R. Huffman, *Nature* **347**, 354 (1990).
- [3] P. Rudolf, M.S. Golden and P.A. Brühwiler, *J. Electr. Spectros. Relat. Phenom.* **100**, 409 (1999).
- [4] M. S. Dresselhaus, G. Dresselhaus, P. C. Eklund, *Science of Fullerenes and Carbon Nanotubes*, Academic Press, San Diego, 1996.
- [5] S. Suto, A. Kasuya, C. W. Hu, A. Wawro, K. Sakamoto, T. Goto, and Y. Nishina, *Thin Solid Films* **281-282**, 602 (1996).
- [6] M. F. Luo, Z. Y. Li and W. Alison, *Surf. Sci.* **402-404**, 437 (1998).
- [7] P. A. Brühwiler, A. J. Maxwell, P. Baltzer, S. Andersson, D. Arvanitis, L. Karlsson, and N. Mårtensson, *Chem. Phys. Lett.* **279**, 85 (1997).
- [8] H. Ulbricht, G. Moos, and T. Hertel, *Phys. Rev. Lett.* **90**, 095501 (2003).
- [9] D. J. Kenny and R. E. Palmer, *Surf. Sci.* **447**, 126 (2000).
- [10] S. Szuba, R. Czajka, A. Kasuya, A. Wawro, and H. Rafii-Tabar, *Appl. Surf. Sci.* **144-145**, 648 (1999).

## 5. Wet deposition of fullerenes

---

- [11] M. Haluska, H. Kuzmany, V. Vybornov, P. Rogl, and P. Fejdl, *Appl. Phys. A* **56**, 161 (1993).
- [12] G. Oszlányi, G. Bortel, G. Faigel, M. Tegze, L. Gránásy, S. Pekker, P. W. Stephens, G. Bendele, R. Dinnebier, G. Mihály, A. Jánossy, O. Chauvet and L. Forró, *Phys. Rev. B* **51**, 12228 (1995).
- [13] P. W. Stephens, G. Bortel, G. Faigel, M. Tegze, A. Jánossy, S. Pekker, G. Oszlányi and L. Forró, *Nature* **370**, 636 (1994).
- [14] T. Almeida Murphy, T. Pawlik, A. Weidinger, M. Höhne, R. Alcalá, and J. M. Spaeth, *Phys. Rev. Lett.* **77**, 1075 (1996).
- [15] C. Knapp, N. Weiden, H. Kass, K.- P. Dinse, B. Pietzak, M. Waiblinger and A. Weidinger, *Mol. Phys.* **95**, 999 (1998).
- [16] D. J. Hornbaker, S.-J. Kahng, S. Misra, B. W. Smith, A. T. Johnson, E. J. Mele, D. E. Luzzi, and A. Yazdani, *Science* **295**, 828 (2002).
- [17] H. Park, J. Park, A. K. L. Lim, E. H. Anderson, A. P. Alivisatos, and P. L. McEuen, *Nature* **407**, 57 (2000).
- [18] A. F. Hebard, M. J. Rosseinsky, R. C. Haddon, D. W. Murphy, S. H. Glarum, T. T. M. Palstra, A. P. Ramirez and A. R. Kortan, *Nature* **350**, 600 (1991).
- [19] R. C. Haddon, A. F. Hebard, M. J. Rosseinsky, D. W. Murphy, S. J. Duclos, K. B. Lyons, B. Miller, J. M. Rosamilia, R. M. Fleming, A. R. Kortan, S. H. Glarum, A. V. Makhija, A. J. Muller, R. H. Eick, S. M. Zahurak, R. Tycko, G. Dabbagh and F. A. Thiel, *Nature* **350**, 320 (1991).
- [20] K. Tanigaki, I. Hirose, T.W. Ebbesen, J. Mizuki, Y. Shimakawa, Y. Kubo, J. S. Tsai, and S. Kuroshima, *Nature* **356**, 419 (1992).
- [21] W. Harneit, *Phys. Rev. A* **65**, 032322 (2002).
- [22] D. Suter and K. Lim, *Phys. Rev. A* **65**, 052309 (2002).
- [23] J. Twamley, *Phys. Rev. A* **67**, 052318 (2003).
- [24] M. Waiblinger, K. Lips, W. Harneit, and A. Weidinger, *Phys. Rev. B* **64**, 159901 (2001).
- [25] E. I. Altman and R. J. Colton, *Phys. Rev. B* **48**, 18244 (1993).
- [26] X. Lu, M. Grobis, K. H. Khoo, S. G. Louie, and M. F. Crommie, *Phys. Rev. B* **70**, 115418 (2004).

- 
- [27] G. Schull and R. Berndt, *Phys. Rev. Lett.* **99**, 226105 (2007).
- [28] S. C. Veenstra, A. Heeres, G. Hadziioannou, G. A. Sawatzky, H. T. Jonkman, *Appl. Phys. A* **75**, 661 (2002).
- [29] <http://www.meinhard.com>
- [30] H. Yu, J. Yan, Y. Li, and W. S. Yang, *Surf. Sci.* **286**, 116 (1993).
- [31] M. V. Korobov, A. L. Mirakyan, N. V. Avramenko, G. Olofsson, A. L. Smith, and R. S. Ruoff, *J. Phys. Chem. B* **103**, 1339 (1999).
- [32] J. P. Cleveland, B. Anczykowski, A. E. Schmid, and V. B. Elings, *Appl. Phys. Lett.* **72**, 2613 (1998).
- [33] S. N. Magonov, V. Elings, and M. H. Whangbo, *Surf. Sci. Lett.* **375**, L385 (1997).
- [34] C. Rey, J. Garcia-Rodeja, L. J. Gallego, and J. A. Alonso, *Phys. Rev. B* **55**, 7190 (1997).
- [35] T. Shimada, H. Nakatani, K. Ueno, A. Koma, Y. Kuninobu, M. Sawamura, and E. Nakamura, *J. Appl. Phys.* **90**, 209-212 (2001).
- [36] W. Chen, V. Madhavan, T. Jamneala, and M. F. Crommie, *Phys. Rev. Lett.* **80**, 1469 (1998).
- [37] J. V. Barth, H. Brune, G. Ertl, R. J. Behm, *Phys. Rev. B* **42**, 9307 (1990).
- [38] R. D. Deegan, O. Bakajin, T. F. Dupont, G. Huber, S. R. Nagel, and T. A. Witten, *Nature* **389**, 827-829 (1997).
- [39] J. I. Pascual, J. Gomez-Herrero, D. Sanchez-Portal and H. P. Rust, *J. Chem. Phys.* **117**, 9531 (2002).
- [40] S. H. Yang, C. L. Pettiette, J. Conceicao, O. Cheshnovsky, and R. E. Smalley, *Chem. Phys. Lett.* **139**, 233 (1987).
- [41] L. Esaki, *Phys. Rev.* **109**, 603 (1958).
- [42] S. M. Sze, *Physics of Semiconductor Devices*, Wiley, New York, 1981.
- [43] I.-W. Lyo and Ph. Avouris, *Science* **245**, 1369 (1989).
- [44] M. Di Ventra, Y.-C. Chen, T. N. Todorov, *Phys. Rev. Lett.* **92**, 176803 (2004).
- [45] C. Zeng, H. Wang, B. Wang, J. Yang, and J. G. Hou, *Appl. Phys. Lett.* **22**, 3595 (2000).



## 5. Wet deposition of fullerenes

---

- [46] M. Grobis, A. Wachowiak, R. Yamachika, and M. F. Crommiea, *Appl. Phys. Lett.* **86**, 204102 (2005).
- [47] I. F. Torrente, K. J. Franke and J. I. Pascual, *J. Phys.: Condens. Matter* **20**, 184001 (2008).

## Appendix A

# Nonequilibrium Green's function theory

Here is given the general formalism of an inelastic electron tunneling through a graphene (molecular) junction using the nonequilibrium Greens function (NEGF) theory, which was used in the IETS modeling in chapter 4.3.4. It follows works of Rossen [1] and Galperin *et al.* [2]. The inelastic tunneling problem is considered in the self-consistent Born approximation. The system consisting of two leads and a bridging graphene layer or a molecule was described by the zero-order Hamiltonian in equation 4.3.3 and the interaction Hamiltonian in equation 4.3.4.

The one-particle Greens functions (GFs) are the main objects used in the dynamical description of a coupled many-body quantum system within the NEGF approach. In our system, they are the electronic and phononic GFs defined on the Keldysh contour by criteria

$$G_{ij}(\tau, \tau') = -i\langle \hat{T}_c \hat{c}_i(\tau) \hat{c}_j^\dagger(\tau') \rangle \quad (\text{electrons}), \quad (\text{A-1})$$

$$D_{ij}(\tau, \tau') = -i\langle \hat{T}_c \hat{A}_i(\tau) \hat{A}_j^\dagger(\tau') \rangle \quad (\text{phonons}), \quad (\text{A-2})$$

where  $\hat{T}_c$  is the time ordering operator, which arranges the operators on the Keldysh contour [3]. The Greens function can be physically interpreted as follows:  $iG_{ij}(\tau, \tau')$  is the probability amplitude that electron in a given state  $i$  at time  $\tau$  will be (was) in state  $j$  at time  $\tau'$ , where  $\tau'$  is not necessarily a later time as  $\tau$ . A similar interpretation can be given to  $D_{ij}(\tau, \tau')$ . The Greens functions satisfy following Dyson-type equations [2]

$$G_{ij}(\tau, \tau') = G_{0,ij}(\tau, \tau') + \sum_{k,l} \int_c d\tau_1 \int_c d\tau_2 G_{0,il}(\tau, \tau_1) \sum_{lk}(\tau_1, \tau_2) G_{kj}(\tau_2, \tau'), \quad (\text{A-3})$$

$$D_{ij}(\tau, \tau') = D_{0,ij}(\tau, \tau') + \sum_{k,l} \int_c d\tau_1 \int_c d\tau_2 D_{0,il}(\tau, \tau_1) \prod_{lk}(\tau_1, \tau_2) D_{kj}(\tau_2, \tau'), \quad (\text{A-4})$$

## A. Nonequilibrium Green's function theory

---

where  $G_0$  and  $D_0$  are the electron and phonon Greens functions of the unperturbed system and  $\Sigma$  and  $\Pi$  are the electron and phonon self energies, respectively. The self energies contain all the interactions of the system. These Dyson equations are essentially dressed single particle interactions that can be represented to a desired level of approximation by the GFs themselves, thus providing a closed set of equations that can be solved self-consistently [2]. The Green's functions and self energies can be used to calculate many one-particle characteristics in the studied system such as the current through the system and electron or phonon density of states.

In order to get information about the steady states the Dyson equations are projected from the Keldysh contour onto the real time axis, resulting in equations for the projected GFs and self-energies. There are four possible situations:

- $\tau'$  is on the upper branch of the Keldysh contour and  $\tau$  is on the lower branch of the Keldysh contour. Now  $\tau' < \tau$  independent of their values and the time ordering operator in equation A-1 arranges the Green's function in the so called greater projection

$$[G^>(\tau, \tau')]_{ij} = -i\langle \hat{c}_i(\tau) \hat{c}_j^\dagger(\tau') \rangle. \quad (\text{A-5})$$

- $\tau'$  is on the lower branch of the Keldysh contour and  $\tau$  is on the upper branch of the Keldysh contour. Now  $\tau' > \tau$  independent of their values and the time ordering operator in equation A-1 arranges the Green's function in the lesser projection

$$[G^<(\tau, \tau')]_{ij} = i\langle \hat{c}_j^\dagger(\tau') \hat{c}_i(\tau) \rangle. \quad (\text{A-6})$$

- Both  $\tau'$  and  $\tau$  are on the upper branch of the Keldysh contour. Now time ordering on the Keldysh contour is identical to time ordering in real time space. The time ordering operator in equation A-1 arranges the Green's function in the time ordered projection

$$G^t(\tau, \tau') = \theta(t_1 - t_2)G^>(\tau, \tau') + \theta(t_2 - t_1)G^<(\tau, \tau'). \quad (\text{A-7})$$

- Both  $\tau'$  and  $\tau$  are on the lower branch of the Keldysh contour. Now time ordering on the Keldysh contour is the opposite of time ordering in real time space. The time ordering operator in equation A-1 arranges the Green's function in the anti time ordered projection

$$G^{\bar{t}}(\tau, \tau') = \theta(t_2 - t_1)G^>(\tau, \tau') + \theta(t_1 - t_2)G^<(\tau, \tau'). \quad (\text{A-8})$$

Apart to these four projections, it is convenient and commonly applied to define two different projections of the Green's functions, which are linear combinations previous

---

four equations. They are called the retarded projection

$$\begin{aligned}
G^r(\tau, \tau') &= G^t(\tau, \tau') - G^<(\tau, \tau') & (A-9) \\
&= G^>(\tau, \tau') - G^{\bar{t}}(\tau, \tau') \\
&= \theta(\tau - \tau') (G^>(\tau, \tau') + G^<(\tau, \tau')),
\end{aligned}$$

and the advanced projection

$$\begin{aligned}
G^a(\tau, \tau') &= G^t(\tau, \tau') - G^>(\tau, \tau') & (A-10) \\
&= G^<(\tau, \tau') - G^{\bar{t}}(\tau, \tau') \\
&= \theta(\tau' - \tau) (G^>(\tau, \tau') + G^<(\tau, \tau')).
\end{aligned}$$

The projections for the phonon Green's function  $D(\tau, \tau')$  can be obtained in the same way. In the remainder of the text, only equations for the greater, lesser and retarded projections of Green's functions and self energies are given. The advanced projection of a Green's function or self energy is always the conjugate transpose of the corresponding retarded projection.

The system is treated as a steady-state system, which means that all two-time quantities depend only on the time difference. Accordingly, it is possible to transform the two-variable Green's functions and self energies into one-variable Green's functions and self energies with a Fourier transformation. The Fourier variable associated with the Green's function and self energy for electrons is denoted by  $E$ , and the Fourier variable associated with the Green's function and self energy for phonons is denoted by  $\omega$ . The resulting Green's functions and self energies are again matrices, where each element is a function of either  $E$  or  $\omega$ . The corresponding equations for the Green's functions are the Dyson equations for the retarded Green's functions

$$G^r(E) = \frac{1}{[G_0^r(E)]^{-1} - \Sigma^r(E)}, \quad (A-11)$$

$$D^r(\omega) = \frac{1}{[D_0^r(\omega)]^{-1} - \Pi^r(\omega)}, \quad (A-12)$$

and the Keldysh equations for the lesser and greater Green's functions

$$\begin{aligned}
G^<(E) &= G^r(E)\Sigma^<(E)G^a(E) & (A-13) \\
G^>(E) &= G^r(E)\Sigma^>(E)G^a(E),
\end{aligned}$$

$$\begin{aligned}
D^<(\omega) &= D^r(\omega)\Pi^<(\omega)D^a(\omega) & (A-14) \\
D^>(\omega) &= D^r(\omega)\Pi^>(\omega)D^a(\omega).
\end{aligned}$$

## A. Nonequilibrium Green's function theory

---

By assuming that the interactions in the system are independent of each other, the total self energy term for the electrons and the phonons for all four individual projections are obtained in the forms

$$\Sigma_{ij}(E) = \Sigma_{ij}^L(E) + \Sigma_{ij}^R(E) + \Sigma_{ij}^{ph}(E), \quad (\text{A-15})$$

$$\Pi_{ij}(\omega) = \Pi_{ij}^{ph}(\omega) + \Pi_{ij}^{el}(\omega), \quad (\text{A-16})$$

where the components of the electronic self energy  $\Sigma$  are the self energies associated with the coupling to the left and right leads ( $\Sigma^L$  and  $\Sigma^R$ ) and the self energy associated with the coupling to the primary phonons ( $\Sigma^{ph}$ ). In the wide band limit,  $\Sigma^L$  and  $\Sigma^R$  can be obtained exactly. The real parts of the retarded and advanced self energies are negligible, while the imaginary parts are energy independent constants written as

$$\begin{aligned} \Sigma_K^r &= -\frac{i}{2}\Gamma^K \\ \Sigma_K^< &= i\Gamma^K f_K(E) \\ \Sigma_K^> &= -i\Gamma^K(1 - f_K(E)), \end{aligned} \quad (\text{A-17})$$

where  $K = L$  for the left lead and  $K = R$  for the right lead.  $f_K(E)$  denotes the Fermi-Dirac distribution function, which depends on the lead's chemical potential  $\mu_K$  by an equation

$$f_K(E) = \left( \exp \left[ \frac{E - \mu_K}{k_B T} \right] + 1 \right)^{-1}. \quad (\text{A-18})$$

$\Gamma^K$  is the level-width matrix caused by hybridizations between the left or right lead and the bridge, which is defined by

$$[\Gamma^K(E)]_{ij} = 2\pi \sum_{k \in K} V_{ik} V_{kj} \delta(E - E_k), \quad (\text{A-19})$$

and it is independent of energy in the wide-band limit. For the electron self energy due to coupling to the phonons, only the lowest order (in electron-phonon coupling  $M$ ) self energies are taken into account. The phonon contribution to the electronic self energy is given by

$$\begin{aligned} [\Sigma_{ph}^r(E)]_{ij} &= i \sum_{k_1, k_2} M_i^{k_1} M_j^{k_2} \int \frac{d\omega}{2\pi} \left[ D_{k_1 k_2}^<(\omega) G_{ij}^r(E - \omega) \right. \\ &\quad \left. + D_{k_1 k_2}^r(\omega) G_{ij}^<(E - \omega) + D_{k_1 k_2}^r(\omega) G_{ij}^r(E - \omega) \right] \\ &\quad + \delta_{ij} \sum_{k_1, k_2, i'} M_i^{k_1} M_{i'}^{k_2} n_{i'}^{el} D_{k_1 k_2}^r(\omega = 0) \\ [\Sigma_{ph}^<(E)]_{ij} &= i \sum_{k_1 k_2} M_i^{k_1} M_j^{k_2} \int \frac{d\omega}{2\pi} D_{k_1 k_2}^<(\omega) G_{ij}^<(E - \omega) \\ [\Sigma_{ph}^>(E)]_{ij} &= i \sum_{k_1 k_2} M_i^{k_1} M_j^{k_2} \int \frac{d\omega}{2\pi} D_{k_1 k_2}^>(\omega) G_{ij}^>(E - \omega), \end{aligned} \quad (\text{A-20})$$

---

where  $M$  is the coupling of the primary phonons to the electronic system, which was defined in the interaction Hamiltonian 4.3.3. In the equations in A-20, integration over  $\omega$  from  $(-\infty, \infty)$  is required. Positive frequencies refer to processes where a phonon is first absorbed and subsequently re-emitted, and negative frequencies refer to processes where a phonon is first emitted and then reabsorbed. The term containing  $n_i^{el}$  is the so-called Hartree term in the electron phonon interaction that is omitted in the remainder of the text, because the density of states for phonons with  $\omega = 0$  is considered zero.

The components of the total phonon self energy  $\Pi$  (equation A-16) are the self energy associated with the coupling to the secondary phonons ( $\Pi^{ph}$ ) and the self energy associated with the coupling to the electronic system ( $\Pi^{el}$ ). In the wide band limit,  $\Pi^{ph}$  can be obtained exactly, using the fact that the thermal bath is in thermal equilibrium. Again, the real parts of the retarded and advanced projections are negligible, while the imaginary parts are energy independent constants

$$\begin{aligned}\Pi_{ph}^r(\omega) &= -\frac{i}{2} \text{sgn}(\omega)\gamma(\omega) \\ \Pi_{ph}^<(\omega) &= -i\gamma(\omega)F(\omega) \\ \Pi_{ph}^>(\omega) &= -i\gamma(\omega)F(-\omega),\end{aligned}\tag{A-21}$$

where the function  $F(\omega)$  is

$$F(\omega) = \begin{cases} N(|\omega|) & \text{if } \omega > 0 \\ 1 + N(|\omega|) & \text{if } \omega < 0 \end{cases}\tag{A-22}$$

and  $\gamma$  denotes the level-width matrix caused by hybridizations between the primary phonon states and the secondary phonon states. It is defined as

$$\gamma_{ij}(\omega) = 2\pi \sum_m U_m^i U_m^j \delta(\omega - \omega_m),\tag{A-23}$$

which is independent of  $\omega$  in the wide band limit.  $N(\omega)$  is the Bose-Einstein distribution function

$$N(\omega) = \left( \exp \left[ \frac{\omega}{k_B T} \right] - 1 \right)^{-1}.\tag{A-24}$$

Finally, the phonon self energy due to the coupling to the electronic system ( $\Pi^{el}$ ), where only the lowest order (in electron-phonon coupling  $M$ ) self energy is taken into

## A. Nonequilibrium Green's function theory

---

account, is expressed by

$$\begin{aligned}
[\Pi_{el}^r(\omega)]_{ij} &= -i \sum_{i_1, i_2} M_{i_1}^i M_{i_2}^j \int \frac{dE}{e\pi} \left[ G_{i_1 i_2}^<(E) G_{i_2 i_1}^a(E - \omega) \right. \\
&\quad \left. + G_{i_1 i_2}^r(E) G_{i_2 i_1}^<(E - \omega) \right] \quad (\text{A-25}) \\
[\Pi_{el}^<(\omega)]_{ij} &= -i \sum_{i_1, i_2} M_{i_1}^i M_{i_2}^j \int \frac{dE}{2\pi} G_{i_1 i_2}^<(E) G_{i_2 i_1}^>(E - \omega) \\
[\Pi_{el}^>(\omega)]_{ij} &= -i \sum_{i_1, i_2} M_{i_1}^i M_{i_2}^j \int \frac{dE}{2\pi} G_{i_1 i_2}^>(E) G_{i_2 i_1}^<(E - \omega).
\end{aligned}$$

**Calculation scheme:** The Green's functions  $G(E)$  and  $D(\omega)$  are functions of the self energies  $\Sigma(E)$  and  $\Pi(\omega)$  as shown in equations A-11, A-12, A-13 and A-14, and the self energies  $\Sigma(E)$  and  $\Pi(\omega)$  are functions of the Green's functions  $G(E)$  and  $D(\omega)$  in equations A-15, A-16, A-20 and A-25. These equations provide a self-consistent calculation scheme that takes an infinite number of non crossing diagrams into account to calculate the Green's functions and self energies. This is called the self-consistent Born approximation. It based on the perturbation theory with the electron-phonon coupling  $M$  as the perturbation parameter. The calculation consists of the following steps.

**Step 1 - grids:** The equations involve integration over the electronic energy  $E$  and the frequency variable  $\omega$ . These are done using numerical grids with a fixed minimum, maximum and point density. The range between minimum and maximum is chosen large enough to span the essential energy and frequency ranges, but small enough to keep calculation time under control. The grid step size is chosen smaller than the spectral widths of the functions, but large enough to keep calculation time under control. To reduce calculation times, the graphene bridge between electrodes was assumed to have only one electronic level at  $E = t_{11} = t$  and only one primary phonon mode at  $\omega = \Omega_{11} = \Omega$ . For all calculations the next standard set of parameters were used:  $\gamma_{ph} = 10^{-3}$  eV,  $E_F = 0$  eV, and  $T = 10$  K. The other parameters  $M$ ,  $t$ ,  $\Omega$ ,  $\Gamma_L$ , and  $\Gamma_R$  were specified next to the calculations results in chapter 4.3.4.

**Step 2 - initial values:** Before the iteration calculation starts, an initial value for either the Green's function or the self energy is required. For this purpose, the Green's functions of the electrons and the primary phonons were taken in the zero-order of the electron-phonon interaction. This means that only coupling to the leads was taken into account for the zero-order electron self energy, and only coupling to

---

the thermal bath was taken into account for the zero-order phonon self energy

$$\Sigma_0(E) = \Sigma^L(E) + \Sigma^R(E) \quad (\text{A-26})$$

$$\Pi_0(\omega) = \Pi^{ph}(\omega). \quad (\text{A-27})$$

This leads the zero-order Green's function for electrons

$$G_0^r(E) = \frac{1}{\bar{E} - t + \frac{i}{2}\Gamma(E)} \quad (\text{A-28})$$

$$G_0^<(E) = \frac{if_L(E)\Gamma^L(E) + if_R(E)\Gamma^R(E)}{(\bar{E} - t)^2 + (\frac{1}{2}\Gamma(E))^2}$$

$$G_0^>(E) = \frac{-i(1 - f_L(E))\Gamma^L(E) - i(1 - f_R(E))\Gamma^R(E)}{(\bar{E} - t)^2 + (\frac{1}{2}\Gamma(E))^2},$$

and to the zero-order Green's function for primary phonons

$$D_0^r(\omega) = \frac{1}{\bar{\omega} - \Omega + \frac{i}{2}\gamma(\omega)} - \frac{1}{\bar{\omega} + \Omega + \frac{i}{2}\gamma(\omega)} \quad (\text{A-29})$$

$$D_0^<(\omega) = F(\omega) [D_0^r(\omega) - D_0^a(\omega)] \text{sgn}(\omega)$$

$$D_0^>(\omega) = F(-\omega) [D_0^r(\omega) - D_0^a(\omega)] \text{sgn}(\omega).$$

Here,  $\bar{E}$  in the denominator of equation A-28 stands for  $E \cdot I$ , where  $I$  is the identity matrix with the same dimensions of the electronic interstate coupling matrix  $t$ . Similarly,  $\bar{\omega}$  in the denominator of equation A-29 denotes  $\omega \cdot I$ , where the identity matrix  $I$  has the same dimensions as the matrix  $\Omega$ .

**Step 3 - update of Green's functions and self energies:** The so far obtained Green's functions  $G(E)$  and  $D(\omega)$  are used in equations A-20 and A-25 to calculate the self energies  $\Sigma(E)$  and  $\Pi(\omega)$ . The self energies due to interactions other than electron-phonon interaction are unchanged. These new self energies are used in equations A-11, A-12, A-13 and A-14 to update the Green's functions. These replace the old values for  $G(E)$  and  $D(\omega)$ .

**Step 4 - iteration:** The updating of the Green's functions and self energies in step 3 is repeated until the self energies  $\Sigma^{ph}$  and  $\Pi^{el}$  have converged. Convergence of a matrix  $M(E)$  is achieved when

$$\left| \frac{M_{ij}^{(n)}(E) - M_{ij}^{(n-1)}(E)}{M_{ij}^{(n-1)}(E)} \right| < \delta \quad (\forall i, j, E), \quad (\text{A-30})$$

where  $\delta$  is predefined tolerance and  $M^{(n)}$  is the matrix  $M$  after  $n$  iteration steps. In this work,  $\delta$  was set to  $10^{-4}$  for both electron and phonon self energies.



## A. Nonequilibrium Green's function theory

---

**Step 5 - one-particle characteristics:** When convergence is achieved, several characteristics of the system can be calculated [2]. The total current through the junction can be expressed as

$$I_L = -I_R = \frac{2e}{\hbar} \int \frac{dE}{2\pi} \text{Tr} [\Sigma_L^<(E)G^>(E) - \Sigma_L^>G^<(E)]. \quad (\text{A-31})$$

The density of electronic states on the bridge is given by

$$\rho_j = -\text{Im} \left[ \int \frac{dE}{\pi} G_{jj}^r(E) \right]. \quad (\text{A-32})$$

The Green's functions and self energies are calculated for all values of the applied bias  $V$  within a predefined range. Subsequently,  $dI/dV$  and  $d^2I/dV^2$  curves are calculated numerically from the  $I(V)$  dependence.

## Bibliography

- [1] E. Rossen, Influence of substrate and tip on inelastic electron tunneling spectroscopy, M.Sc. thesis, Eindhoven University of Technology (2007).
- [2] M. Galperin, M. A. Ratner, and A. Nitzan, *J. Chem. Phys.* **121**, 11965 (2004).
- [3] L. Keldysh, *Sov. Phys. JETP* **20**, 1018 (1965).

# Summary

Graphene-based materials exhibit many unique physical properties that are intriguing for both fundamental science and application purposes. This thesis describes three systems of  $sp^2$  bonded carbon: graphite, graphene and fullerene, and studies the electron behavior in these materials and how it is affected by the presence of defects. It is shown here that by inducing specific defects, phenomena such as ferromagnetism and superconductivity can arise in these systems.

Graphite and its structural defects are studied by scanning tunneling microscopy and spectroscopy in chapter 2. This chapter represents the first detailed analysis of the structural and electronic properties of grain boundaries in graphite. Grain boundaries are the most common defects in highly oriented pyrolytic graphite (HOPG) because of its polycrystalline character. They form periodic arrays of point defects that are arranged in planes perpendicular to the graphene planes. On the graphite surface, grain boundaries manifest themselves as one-dimensional chains of point defects with a width around 1 nm and a length up to several micrometers. The periodic structure within a single grain boundary displays only two possible distances between point defects. This periodicity was found to be 0.5-10 nm in different grain boundaries. Atomically resolved STM images showed that grain boundaries are tilt grain boundaries, which are created between two rotated graphite grains. A new proposed structural model of grain boundaries based on periodically repeated point defects could explain all observed periodicities in STM. The electronic structure of grain boundaries has been studied locally with scanning tunneling spectroscopy (STS). Grain boundaries possess enhanced charge densities and localized electron states in comparison to the bare graphite surface. These states extend up to 4 nm from grain boundaries. Two localized electron states have been observed on grain boundaries having small periodicities ( $< 4$  nm), while a single localized state at the Fermi energy has been measured for larger periodicities, indicating a long-range interaction among point defects within a grain boundary.

An unexpected phenomenon in carbon-based materials, ferromagnetism, is studied in chapter 3. Ferromagnetic signals have been observed in HOPG locally by

---

magnetic force microscopy (MFM), and in the bulk magnetization measurements using a superconducting quantum interference device magnetometer (SQUID) at room temperature. In MFM, the ferromagnetic signals have been detected specifically at line defects of the graphite surface. The magnetic moments in these defects pointed out of the graphite surface. SQUID magnetization measurements in HOPG revealed anisotropic ferromagnetic-like hysteresis loops at both 5 K and 300 K. The saturation magnetization reached  $1 \times 10^{-2}$  emu/g along the basal plane of graphite, while it was an order of magnitude smaller in the direction parallel to graphene planes. Magnetic impurities have been excluded as the origin of the magnetic signal after careful analysis, supporting an intrinsic magnetic behavior of carbon-based materials. The observed ferromagnetism has been attributed to originate from unpaired *sp*-electron spins, localized at defects sites of grain boundaries. It was pointed out that the structure of defects within grain boundaries cause sublattice unbalance, which is a sufficient condition for formation of local magnetic moments in graphene lattice according to Lieb's theorem. Because of the unique structure of grain boundaries, defects are formed on the same sublattice and therefore the magnetic coupling between the magnetic moments is always ferromagnetic. The ferromagnetism in graphite sustains unexpectedly high temperatures, where the Curie temperature is well above room temperature. Such a high Curie temperature could be explained on the basis of the 2D anisotropic Heisenberg model using self-consistent spin-wave theories, which gave rise to  $T_C = 764$  K. In the future, a controlled way of producing defects in graphite could lead to production of light and high temperature carbon ferromagnets. Moreover, grain boundaries in graphite can find applications in the field of spintronics as spin-polarized guides.

Chapter 4 is devoted to a single layer of graphite, graphene, grown on SiC(0001). Graphene has shown a number of unexpected physical properties in the last years, which makes it a promising candidate for future electronic devices. Graphene possess a high quality two dimensional electron gas with extremely high mobility at room temperature, where charge carriers can be tuned between electrons and holes by gate. The system of graphene on SiC seems to be the most interesting platform for application purposes and for large scale production. However, the quality of the 2D electron gas in graphene on SiC is much lower than for a free standing graphene or graphene supported on SiO<sub>2</sub> substrates. For this reason, the main focus in this chapter was devoted to the understanding the influence of the SiC interface on the electronic properties of a graphene monolayer. The successful formation of a few-layer graphene (1-3) on SiC(0001) has been performed by a heating procedure in ultra high vacuum. The resulting graphene layers have been studied by scanning tunneling microscopy (STM) and spectroscopy (STS). STM topography and STS measurements have shown that

---

a single graphene layer grown on a SiC(0001) substrate is still affected by the electronic structure of the interface layer of SiC. The graphene monolayer demonstrated transparency at bias voltages  $> 100$  mV in STM. At these voltages, localized states belonging to the underlying interface layer were observed on the first graphene layer. Inelastic electron tunneling spectroscopy (IETS) has revealed an extremely strong inelastic phonon contribution for the out of plane acoustic phonon (70 meV) of graphene, reaching a gigantic 50% intensity of the IETS peaks. This inelastic contribution has been enhanced particularly on the places with localized electron states of the interface layer. Surprisingly, STS spectra on single layer graphene have shown a gap-like feature at the Fermi level, which was pinned between the inelastic phonon contributions at  $\pm 70$  meV. This gap-like feature is probably due to charge modulations from graphene electrons interacting with localized interlayer electron states, indicating that electron correlation effects play an important role for the charge carrier behavior at the Fermi-level. Undoped graphene is a semi-metal, but several ideas have been proposed how graphene can become superconducting by doping. Here is reported that a few layers of epitaxial grown graphene shows a transition to two-dimensional fluctuating superconductivity. The underlying mechanism is based on strong electron-phonon coupling between graphene electrons interacting with localized electron states formed at the SiC(0001) substrate/graphene interface and  $z$ - acoustic phonons of graphene.

Finally, chapter 5 deals with curved graphene systems, fullerenes, for which a new wet deposition technique was successfully developed to produce ultra thin fullerene films. This technique could be especially useful for fullerene derivatives, which cannot sustain the high temperatures needed to evaporate these molecules in ultra high vacuum. It uses a special nebulizer to spray coat fullerenes dissolved in toluene or carbon disulfide onto a sample surface under ambient conditions. Spray coating of  $C_{60}$  has been successfully tested on graphite and gold surfaces. Monolayer thick  $C_{60}$  films have been formed on both surfaces at particular deposition parameters as confirmed by AFM and STM. The structural and electronic properties of spray coated  $C_{60}$  films on Au(111) have shown comparable results to thermally evaporated  $C_{60}$ . The only difference was that solvent residues remained attached to the gold surface and could not be removed. However, the solvent residues have not modified the electronic structure of  $C_{60}$  on Au(111) in the case of  $CS_2$ .



# Samenvatting

Grafeen gebaseerde materialen vertonen verscheidene unieke fysische eigenschappen die interessant zijn voor zowel fundamenteel onderzoek als voor concrete toepassingen. In dit proefschrift worden drie vormen van  $sp^2$  gebonden koolstof beschreven, namelijk grafiet, grafeen en fullerenen. Tevens wordt er gekeken hoe deze materialen worden beïnvloed door defecten. Uit het beschreven onderzoek komt naar voren dat het introduceren van specifieke defecten kan leiden zowel ferromagnetisme als supergeleiding in deze systemen.

Grafiet en de structurele defecten daaraan zijn onderzocht met behulp van een raster tunnel microscoop (RTM), zoals beschreven is in hoofdstuk 2. In dit hoofdstuk word een gedetailleerde analyse van de structurele en elektronische eigenschappen van domeingrenzen in grafiet gegeven. Domeingrenzen zijn het meest voorkomende soort defect in sterk geordend pyrolitisch grafiet (SGPG) vanwege het polykristallijn karakter van SGPG. Deze defecten vormen een periodiek reeks van punten die loodrecht op de grafeenvlakken staan. Aan het grafeenoppervlak manifesteren domeingrenzen zich als eendimensionale ketens van puntdefecten met een breedte van ongeveer 1 nm en lengtes tot enkele micrometers. De periodieke structuur binnen een enkel domein vertoont slechts twee mogelijke afstanden tussen puntdefecten. Voor verschillende domeinen bleek deze periodiciteit te liggen tussen 0.5 en 10 nm. RTM plaatjes met atomaire resolutie tonen aan dat de domeingrenzen geroeteerde domeingrenzen zijn, die gecreëerd zijn tussen twee grafietdomeinen. Een nieuw model, dat de domeingrenzen beschrijft op basis periodiek herhaalde puntdefecten, kan alle met RTM geobserveerde periodiciteiten verklaren. De elektronische structuur van de domeingrenzen is lokaal bestudeerd met behulp van raster tunnel spectroscopie (RTS). Domeingrenzen vertonen verhoogde ladingsdichtheden en meer gelokaliseerde elektronische toestanden in vergelijking met een kaal grafiet oppervlak. Deze toestanden strekken zich tot 4 nm van de domeingrenzen uit. Twee gelokaliseerde elektron toestanden zijn waargenomen op domeinen met kleine periodiciteiten ( $< 4$  nm), terwijl er slechts één gelokaliseerde toestand aan het Fermi niveau gemeten is voor grotere periodiciteiten. Dit geeft aan dat er een langeafstandsinteractie aanwezig is tussen puntdefecten binnen een

---

domeingrens.

Een onverwacht fenomeen dat optreed op koolstof gebaseerde materialen, namelijk ferromagnetisme, wordt beschreven in hoofdstuk 3. Ferromagnetische signalen zijn waargenomen in SGPG met behulp van zowel magnetische kracht microscopie (MKM) als bulk magnetisatiemetingen met behulp van een supergeleidende quantum interferentie device magnetometer (SQUID) bij kamertemperatuur. In MKM zijn de ferromagnetische signalen specifiek waargenomen bij lijn defecten aan het grafietoppervlak. De magnetische momenten in deze defecten staan loodrecht op het grafietoppervlak. SQUID magnetisatiemetingen aan SGPG vertonen anisotropische ferromagnetischachtige hysteresis lussen bij zowel 5 als 300 K. De magnetische verzadiging bereikte  $1 \times 10^{-2}$  emu/g in de richting loodrecht op het grafietoppervlak, terwijl het een orde grootte kleiner was in de richting parallel aan de grafeenvlakken. Na zorgvuldig onderzoek zijn magnetische onzuiverheden uitgesloten als oorzaak van dit magnetische signaal, wat de gedachte ondersteunt dat uit koolstof bestaande materialen intrinsiek magnetisch gedrag vertonen. Het waargenomen ferromagnetisme wordt toegeschreven aan de ongepaarde spin van *sp*-elektronen, die zich op defectlocaties van de domeingrenzen bevinden. Er is al op gewezen dat de structuur van de defecten in de domeingrenzen er voor zorgen dat er een onbalans is in het subrooster. Deze onbalans is volgens de theorie van Lieb een voldoende voorwaarde voor de vorming van een magnetische moment in het grafeenrooster. Door de unieke structuur van de domeingrenzen worden defecten gevormd op het zelfde subrooster en daardoor is de magnetische koppeling tussen de magnetische momenten altijd ferromagnetisch. Het ferromagnetisme in grafeen is waargenomen bij onverwacht hoge temperaturen; de Curie temperatuur ligt duidelijk boven kamertemperatuur. Een dergelijke hoge Curie temperatuur kan verklaard worden met behulp van het 2D anisotropisch Heisenberg model door gebruik te maken van zelfconsistente spin-golf theoriën. Deze methode levert een Curie temperatuur van 768 Kelvin op. In de toekomst kan, het op gecontroleerde wijze aanbrengen van defecten in grafiet, leiden tot lichte en hoge-temperatuur ferromagneten. Daarnaast kunnen domeingrenzen in grafiet toepassing vinden in de spintronica als spingepolariseerde geleiders.

Hoofdstuk 4 behandelt de resultaten van het onderzoek aan een enkele laag grafiet, oftewel grafeen, dat gegroeid is op SiC(0001). De afgelopen jaren is gebleken dat grafeen een aantal onverwachte fysische eigenschappen bezit die het, in potentie, een interessant materiaal voor toekomstige elektronische apparaten maken. Een van de eigenschappen die grafeen bezit is een hoge kwaliteits 2-dimensionaal elektronen gas met een extreem hoge mobiliteit bij kamertemperatuur, waar met behulp van een stuur-elektrode gekozen kan worden tussen elektronen of gaten als ladingsdragers. Grafeen op SiC lijkt het meest interessante systeem voor toepassingsdoeleinden en

---

voor productie op grote schaal. Echter, de kwaliteit van het 2D elektronengas van grafeen op SiC is veel lager dan dat van een losse, op zich staande, laag grafeen of van grafeen dat ondersteund wordt door een SiO<sub>2</sub> substraat. Om deze reden ligt het (hoofd) focus van het onderzoek dat in dit hoofdstuk wordt beschreven op het begrijpen van de invloed van het SiC interface op de elektronische eigenschappen van de grafeenmonolaag. Met behulp van een verhittingsprocedure in ultra hoog vacuüm is een succesvolle vorming van enkele lagen van grafeen (1-3) op SiC(0001) tot stand gebracht. De resulterende grafeenlagen zijn bestudeerd met raster tunnel microscopy (RTM) en spectroscopie (RTS). RTM topografie en RTS metingen hebben aangetoond dat een enkele laag grafeen gegroeid op een SiC(0001) substraat nog steeds beïnvloed wordt door de elektronische structuur van de grenslaag het SiC. In de RTM is de grafeenmonolaag transparant voor bias voltages  $> 100$  mV. Bij dit voltage zijn gelokaliseerde toestanden, behorende bij het onderliggende grenslaag, waargenomen op de bovenste grafeenlaag. Inelastische elektron tunnel spectroscopie (IETS) heeft aangetoond dat grafeen een extreem sterke inelastische fononbijdrage vertoont voor het transversaal akoestisch fonon (70 meV), dat een gigantische 50% intensiteit bereikt. De inelastische bijdrage wordt vooral versterkt op die plaatsen waar de elektronische toestanden van de grenslaag gelokaliseerd zijn. Verrassend genoeg vertonen de RTS spectra van een enkele laag grafeen een gat-vormig fenomeen aan het Fermi niveau dat zich bevindt tussen de fononbijdragen bij  $\pm 70$  meV. Dit gat-vormig fenomeen ontstaat waarschijnlijk door ladingsveranderingen van elektronen van het grafeen, als gevolg van een wisselwerking van deze elektronen met gelokaliseerde elektronische toestanden van de SiC grenslaag. Deze wisselwerking toont aan dat elektroncorrelatieëffecten een belangrijke rol spelen bij het ladingstransportgedrag aan het Fermi niveau. Ongedoopt grafeen is een halfmetaal. Echter, verscheidene theorieën stellen voor dat doping er voor kan zorgen dat grafeen supergeleidend wordt. Uit het onderzoek dat in dit proefschrift beschreven wordt blijkt dat een uit een paar lagen bestaand, epitaxiaal gegroeid, grafeenpreparaat een transitie naar tweedimensionaal fluctuerend supergeleiding vertoont. Het onderliggend mechanisme is gebaseerd op sterke elektron-fonon koppeling tussen grafeenelektronen, die een interactie hebben met de gelokaliseerde elektronische toestanden die ontstaan aan het SiC(0001) substraat-grafeen grensvlak, en de  $z$ -akoestische fononen van grafeen.

Tenslotte behandelt hoofdstuk 5 gekromde grafeensystemen, oftewel fullerenen, voor welke een nieuwe depositietechniek is ontwikkeld waarbij met behulp van een vloeistoftechniek gededoneerd wordt en een ultra dunne film van fullerenen ontstaat. Deze techniek kan misschien erg nuttig zijn voor fullereenderivaten die die de hoge temperaturen, die nodig zijn voor het opdampen in ultra hoog vacuüm, niet kunnen doorstaan. De genoemde techniek maakt gebruik van een vernevelaar om fullerenen,



---

opgelost in toluen of koolstofdissulfide, op een oppervlak te sproeien bij kamertemperatuur en atmosferische druk. Het spray-coaten van  $C_{60}$  films op grafiet- en goudoppervlakken is bestudeerd. Met behulp van atomaire kracht microscopie (AKM) en RTM is bevestigd dat, bij specifieke depositieparameters,  $C_{60}$  films met een dikte van exact een monolaag gevormd worden op beide oppervlakken. De structurele en elektronische eigenschappen van gespraycoate  $C_{60}$  films op Au(111) vertonen vergelijkbare resultaten met die van thermisch opgedampt  $C_{60}$ . Echter, vervuilingen uit het oplosmiddel hechtten zich aan het goudoppervlak en konden niet worden verwijderd, maar zij wijzigden niet elektronstructuur van  $C_{60}$  op Au(111) voor het geval van  $CS_2$ .

# Acknowledgements

Without the help and contribution of many people during the last four years it would have been impossible to obtain the results described in this thesis. On this place I would like to thank all the people, who I have been working with, for their help, support and for creating a very nice working atmosphere in the group of Molecular Materials and Nanosystems.

First of all I would like to thank my advisor, dr. Kees Flipse, for giving me the opportunity to perform this challenging research and guiding me through the PhD study. It has not been easy to understand so many peculiar results covering many fields of physics. However, Kees has always come enthusiastically with diverse new ideas that could explain these findings. All this also would not have been possible if there was not the support and openness from prof. René Janssen, who makes the unity in the M2N group, consisting of two sometimes distant parts: chemistry and physics.

Special credits go to Kevin van de Ruit, who has been my coauthor in the research dealing with graphene on SiC described in chapter 4. His unique dedication gave rise to many wanted and unwanted results. I like to express many thanks to my office and STM lab colleagues Joris Hagelaar and Nick Podaru for their collaborations and the great time we had together. I should not forget to thank Erwin Rossen, who has helped me with the modeling of the IETS spectra using Green's function formalism.

The support from our collaborations were extremely important for my thesis work. I would like to thank to Reinoud Lavrijsen for SQUID measurements and prof. Henk Swagten and prof. Bert Koopmans for their discussions and comments on ferromagnetism in graphite. I am grateful to Peter Mutsaers for the PIXE analysis of the HOPG sample. Many thanks to all members of Calipso, especially to prof. Hidde Brongersma for LEIS measurements. I am particular grateful to prof. Mikhail Katsnelson for his theoretical support and fruitful discussions. Special thanks belong to Thomas Seyller for providing SiC samples and other important information. I also thank Jens Hauschild and prof. Wolfgang Harneit for providing samples of endohedral fullerenes.

---

In particular, I like to thank Gerard Wijers for technical support, without which the STM lab would be in "ruins", and for introducing me to cycling in Eindhoven. I really enjoyed the cycling tours we had together. Of course, I should not forget to thank Rein Rumphorst for his help with electronic devices and wonderful talks in Dutch at the coffee room about the important and unimportant issues of life. Dank je wel Rein. I like to thank also Wijnand Dijkstra for support in electronic and computer devices. Many thanks belong to Oleg Kurnosikov for his expertise in Omicron STM setups.

I highly appreciate the help and support from all the M2N colleagues working with me during my PhD program: Rik van Laarhoven, Ron Willems, Martijn Kemerink, prof. Reinder Coehoorn, Klára Maturová, Marta Fonrodona, Alexandre Nardes, Dimitri Charrier, Yinxin Liang, Cristina Popa, Juan Amir, Tănasă, Jean-Michel Wulveryck, Siebe van Mensfoort, Erik Roeling and Simon Mathijssen.

Finally, I would like to thank my mother, family and girlfriend for their encouragement and always standing by me.

# Curriculum Vitae

- November 9, 1980    Born in Nové Město na Moravě, Czech Republic.
- 1999                Graduated from Gymnasium Pardubice, Czech Republic.
- 1999 - 2004        M. Sc. (cum laude) in applied physics, Brno University of Technology, Czech Republic.
- Traineeship at the group of Molecular Materials and Nanosystems (M2N) of the department of Applied physics, Eindhoven University of Technology, Eindhoven, The Netherlands. Subject: *Scanning probe microscopy studies of fullerenes on graphite*, supervised by dr. ir. C. F. J. Flipse and prof. dr. ir. R. A. J. Janssen.
- Master thesis project at the group of Physical Engineering, faculty of Mechanical Engineering, Brno University of Technology. Subject: *Application of scanning probe microscopies in nanotechnology*, supervised by dr. R. Kalousek, and prof. T. Šíkola.
- 2004 - 2009        PhD project at the group of molecular materials and nanosystems (M2N) of the department of applied physics, Eindhoven university of technology, Eindhoven, The Netherlands. Subject: *The role of defects on electron behavior in graphene materials*, supervised by dr. ir. C. F. J. Flipse and prof. dr. ir. R. A. J. Janssen.

